

Stein Inge Rabben  
Non-invasive methods for estimating  
hemodynamic parameters related to  
left ventricular load

NTNU Trondheim  
Norges teknisk-naturvitenskapelige  
universitet

Doktor ingeniøravhandling 2000:52  
Institutt for teknisk kybernetikk

ITK-rapport 2000:6-W



**Non-invasive methods for estimating  
hemodynamic parameters related to left  
ventricular load**

Stein Inge Rabben

Norwegian University of Science and Technology

March, 2000

Non-invasive methods for estimating hemodynamic parameters related to left ventricular load  
Stein Inge Rabben

NTNU Trondheim  
Norges teknisk-naturvitenskapelige universitet  
Doktor ingeniøravhandling 2000:32  
Institutt for teknisk kybernetikk  
ITK-rapport 2000:6-W

ISBN 82-7984-054-0

## Abstract

This thesis, containing an introduction and five separate papers, is a contribution to non-invasive methods for determining hemodynamic parameters related to left ventricular load. Specifically, the thesis describes methods for deriving myocardial fiber stress, global chamber geometry, arterial diameter, aortic pressure and arterial pulse wave velocity.

In **paper A**, equations for estimating regional fiber stress in rotationally symmetric chambers and equatorial fiber stress in prolate spheroidal chambers are developed. The equations were validated 1) against an idealized prolate spheroidal chamber whose wall thickness was such that the fiber stress was uniform from the equator to apex, and 2) against an equation for determining volume-averaged stress from measurements of the ratio between cavity and wall volumes. The model was also used to estimate a theoretical muscle fiber orientation distribution across the myocardial wall. The estimated fiber orientation was in qualitative agreement with published measurements.

Equations for estimating myocardial stress require measurements of left ventricular geometry. **Paper B** describes a robust and efficient semiautomatic method for obtaining wall boundaries in ultrasound M-mode images. The robustness of the method is ensured by utilizing both grey-scale and tissue Doppler data in a global contour optimization criterion. The global minimum of the criterion is efficiently found by using the computational attractive dynamic programming technique. In M-mode images from 19 human subjects, we compared automatically detected contours with contours manually outlined by four echocardiographers. For all boundaries inspected, the average distance between the automatically detected contours and the manual outlines was smaller than the average distance between the manual outlines.

An estimate of the central aortic pressure, and thereby ventricular pressure during ejection, can be obtained by calibrating peripheral pulse measurements using systolic and diastolic brachial arterial pressures. In **paper C**, a Doppler-based method for tracking vessel walls is presented and evaluated. The tracking algorithm, which is an extension of the conventional auto-correlation method, is based on estimating both the mean Doppler frequency and the RF center frequency. To make a systematic evaluation of the estimator, we performed computer simulations of vessel wall-motion, where parameters such as pulse bandwidth, signal-to-noise ratio, packet size and sample volume were varied. The extended auto-correlation method was compared to the conventional auto-correlation method and two alternative cross-correlation methods. Under the specific simulation conditions considered, the extended auto-correlation method had the lowest bias of all methods, and a variance in the same range as the cross-correlation methods.

The pulse wave velocity is one of the determinants of aortic pressure. **Paper D** presents a novel method for estimating pulse wave velocity. During the reflection free period of the cardiac cycle, the pulse wave velocity equals the ratio between the arterial

flow and the cross-sectional area (area-flow method). To make the area-flow method applicable to non-invasive ultrasound recordings, we also developed a method for estimating arterial flow from pulsed wave Doppler measurements of blood velocity. Data from 21 human subjects (age 23–74) and four dogs showed that the area-flow method and a comparison method based on arterial cross-sectional area and pulse-pressure measurements agreed well on average. When the human subjects were divided into three separate age groups, both methods gave group means that increased with age. As expected, the estimated pulse wave velocity also decreased when the aortic pressure was lowered in two of the dogs. However, on a per-subject basis, discrepancies were observed between the methods, indicating that the methods cannot be used interchangeably.

Because of wave propagation and reflections, the pressure waveforms at the subclavian and carotid arteries are different from the central aortic pressure. A model-study of a method for deriving central aortic pressure waveforms from carotid pressure and flow measurements was recently published. An evaluation of this method is described in **paper E**; the method is used on carotid diameter and velocity measurements from four dogs. The method, which is based on a lossless transmission line approach, did not give reliable reconstructions of the central aortic pressure in the four dogs. To find a possible explanation for the findings, we also evaluated a viscous transmission line model. The viscous transmission line model, which gave better reconstructions, indicated that there was considerable attenuation in the carotid arteries of the four dogs, probably due to the small diameters (2.0–2.5 mm). However, due to their larger carotid diameter, the viscous losses in humans are lower than in dogs. Therefore, the method should be further tested on human data.

# Preface

This thesis is submitted to the Norwegian University of Science and Technology (NTNU) for partial fulfillment of the requirements of the degree of "Doktor Ingeniør". The research project was carried out, during the period 1994-1999, at the Ultrasound Group of the Department of Physiology and Biomedical Engineering (IFBT), Faculty of Medicine, NTNU. My supervisor has been Professor Bjørn Angelsen. During the periods, January 1994 to February 1997 and July 1998 to August 1999, the project was supported by the Program for Medical Technology at NTNU. Formally, I was affiliated to the Department of Engineering Cybernetics, Faculty of Electrical Engineering and Telecommunications, NTNU. From March 1997 to June 1998 I was employed by Vingmed Sound AS. During the fall of 1999, the Faculty of Medicine supported the research project.

## Acknowledgements

This work had not been possible without help from other people. First of all I wish to thank Professor Bjørn Angelsen, Professor Fridtjov Irgens and Professor Hans Torp for their supervision during this work. Their knowledge and ideas have been invaluable to me. Bjørn Angelsen introduced me to non-invasive methods in cardiology. His mathematical and physical intuition, his incredible enthusiasm and his never ending search for theoretical solutions to all sorts of problems are unbelievable. Fridtjov Irgens taught me continuum mechanics and helped me gain insight in the field of biomechanics. Had he not been present in the initial phases of my work, this thesis would never have evolved. Hans Torp supervised me during the last part of the project. His way of supervising students has set an important example for me. I also appreciate his making it possible for me to be a system administrator at IFBT during the last months of the project, thus prolonging my financial support.

My most sincere thanks go to colleagues and friends: Jan Hystad, Vidar Sørhus, Leif Rune Hellevik, Andreas Heimdal, Steinar Bjærum, Sevald Berg, Anders Torp, Johan Kirkhorn, Espen Remme, Tonni Johansen and Gunnar Taraldsen. I thank Jan Hystad for pulling me out of the office. Special thanks also to Vidar Sørhus, my "roommate", who through these years has listened to all my complaints without getting mad. I will remember the special support that both Jan and Vidar gave me through the difficult

period after the deaths of my twins. Thanks also to Leif Rune Hellevik for being the one who read my manuscripts most carefully and gave such constructive comments. Leif Rune also showed that it is indeed possible to finish a doctoral degree in biomechanics at our university.

I also wish to thank Professor Otto Smiseth, National Hospital, who invited me to his lab to record experimental data, Professor Nikos Stergiopoulos, EPFL, who invited me to Lausanne to sort out methodological issues of the last two papers, and Patrick Segers, University of Gent, who learnt me about viscous transmission line models.

Some of the methods that I present in the thesis required programming by Svein Brekke, Erik Østlyngen, Lars Eilertsen, Ragnar Wisløff, and Øystein Veland. Their help is greatly appreciated.

The collaboration with the medical community was very inspiring. Many thanks to Asbjørn Støylen, Stig Slørdahl, Bjørn Olav Haugen, Knut Bjørnstad, Jan Pål Lønnechen and Johannes Soma at the University Hospital in Trondheim, and Stig Urheim, Thor Edvardsen and Helge Skulstad at the National Hospital.

Nancy Eik-Nes revised the text of the thesis. Many thanks.

The thesis would never have evolved without financial support from the Program for Medical Technology at NTNU, GE Vingmed Ultrasound and the Faculty of Medicine at NTNU.

Finally, I wish to thank Anne Ma Nordbø for being the one she is. Her extreme patience is truly remarkable. The period after the deaths of our two small boys was very difficult, but we have pulled each other through it. During seven weeks in 1998, the twins taught me more about myself than did six years of doctoral work.

Trondheim, March 2000

Stein Inge Rabben

# Contents

<b>Introduction</b>	<b>1</b>
1 Left ventricular load . . . . .	1
1.1 Cardiac adaptation to overload . . . . .	2
1.2 Oxygen consumption, external work and efficiency . . . . .	3
1.3 The arterial tree . . . . .	4
2 Aims of the study . . . . .	5
3 Estimation methods . . . . .	6
3.1 Aortic pressure estimation . . . . .	6
3.2 Myocardial stress estimation . . . . .	7
3.3 Pulse wave velocity estimation . . . . .	9
4 Contributions . . . . .	10
5 <i>In vivo</i> examples . . . . .	11
5.1 A healthy subject . . . . .	11
5.2 A patient with post-infarction failure . . . . .	13
6 Concluding remarks and future directions . . . . .	14
References . . . . .	19

**Paper A – Equations for estimating muscle fiber stress in the left ventricular wall**

*Heart and Vessels, Accepted, 1999*

S.I. Rabben, F. Irgens and B. Angelsen

**Paper B – Semiautomatic contour detection in ultrasound M-mode images**

*Ultrasound in Medicine and Biology, 26(2):287–296, 2000*

S.I. Rabben, A.H. Torp, A. Støylen, S. Slørdahl, K. Bjørnstad, B.O. Haugen and B. Angelsen

- Paper C – Ultrasound-based vessel wall tracking: an auto-correlation technique with RF center frequency estimation**  
*Submitted for publication, 2000*  
S.I. Rabben, S. Bjærum, V. Sørhus and H. Torp
- Paper D – An ultrasound-based method for determining pulse wave velocity in the carotid artery**  
*Unpublished*  
S.I. Rabben, N. Stergiopoulos, L.R. Hellevik, O.A. Smiseth, S. Slørdahl, S. Urheim and B. Angelsen
- Paper E – Estimation of the central aortic pressure waveform from diameter and blood velocity measurements in the canine carotid artery**  
*Unpublished*  
S.I. Rabben, N. Stergiopoulos, L.R. Hellevik, P. Segers, O.A. Smiseth, T. Edvardsen, H. Skulstad and B. Angelsen

# Introduction

This thesis contains an introduction and five separate papers. The papers are self-contained and complete with abstracts and references. The introduction is divided into six sections. Section one is a short introduction to the subject of left ventricular load. Section two presents the aims of the research project. The third section puts the non-invasive methods of the papers into a larger context. The fourth section lists the major contributions of the thesis. Section five presents some *in vivo* examples of chamber geometry and myocardial stress estimates. The introduction ends with concluding remarks and directions for future studies.

The papers, posters and abstracts that have been published during this research project are listed in the References [2, 3, 26, 46–51, 55, 71].

## 1 Left ventricular load

The left ventricle adapts the pressure and cardiac output so that adequate amounts of blood are able to reach all organs. The major intrinsic control mechanism of the heart is the Frank-Starling mechanism: an increase in **preload** (diastolic filling) increases the cardiac output and/or ventricular pressure. Preload is often defined as end-diastolic pressure, because the pressure at end-diastole is related to the muscle fiber length just before contraction (lower right corner of the pressure-volume loop of Fig. 1). The major extrinsic control mechanisms of the heart are the nervous and humoral control systems that regulate mainly **heart rate** and **contractility** (the ability of the myocardium to shorten and to develop force). During ejection, the left ventricle pumps blood into the arterial system against an **afterload**. Investigators often define afterload as the ventricular pressure during ejection (upper part of the pressure-volume loop of Fig. 1).

The loading conditions of the myocardial muscle fibers depend on both chamber geometry and ventricular pressure. With the same amount of myocardial stress (force per unit cross-sectional area), a small chamber will generate much higher pressures than a large chamber. This is due to the higher muscle fiber curvature in the small chamber than in the large chamber (Law of Laplace). Therefore, investigators also define preload and afterload in terms of myocardial stress at end-diastole and during

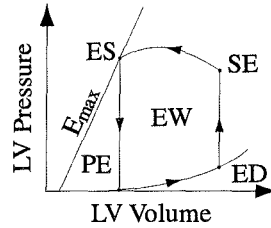


**Figure 1:** Illustration of the pressure and volume in a human left ventricle. ED = end-diastole. SE = start-ejection. ES = end-systole.  $E_{max}$  = contractility index. EW = external work, the area within the pressure-volume loop. PE = potential energy, the area below the  $E_{max}$  curve and left of the pressure-volume loop.

ejection, respectively.

## 1.1 Cardiac adaptation to overload

There are two main categories of left ventricular overload: pressure and volume overloads.

In patients with pressure overload, the left ventricular pressure is higher than normal. The two common causes for pressure overload are hypertension, in which the aortic (and thereby ventricular) pressure is increased due to changes in the vasculature, and aortic stenosis, in which there is a pressure gradient across the aortic valve. Unfortunately, ventricular pressure cannot be measured non-invasively. The doctors therefore use cuff measurements at the brachial artery for diagnosing hypertension. The cutoff value for hypertension is 140/90 mmHg (systolic/diastolic pressures). Note, however, that in some patients there may be significant differences between aortic and brachial pressures. For patients with aortic stenosis, the pressure gradient across the valve can be estimated by ultrasound Doppler techniques. A mean pressure gradient of 50 mmHg is considered significant.

In normal conditions, the cardiac output is 3–3.5 L/min. In patients with aortic regurgitation, blood leaks back into the left ventricle during diastole, whereas in patients with mitral regurgitation, blood leaks back into the left atrium during systole. In both cases, the left ventricle experiences a volume overload since it must deliver a greater-than-normal stroke volume in order to supply the adequate amount of blood to the organs (3–3.5 L/min).

In the long run, the left ventricle adapts to abnormal volume or pressure loads. However, cardiac myocytes lose their ability to duplicate soon after birth; they respond to increased load only by an increase in cell size (hypertrophy) [37]. Ventricular pressure overload is associated with increased wall thickness and almost unchanged

internal diameter (concentric hypertrophy). In contrast, ventricular volume overload is associated with increased wall thickness and increased internal diameter (eccentric hypertrophy).

The appropriateness of the ventricle's anatomic and functional responses to volume or pressure loads has been evaluated by studying myocardial stress estimates [22, 25, 28]. For example, Grossman et al. [22] hypothesized that the increased systolic stress, associated with pressure overload, results in fiber thickening sufficient to return the systolic stress to normal. The increased diastolic stress, associated with volume overload, results in gradual fiber elongation which improves efficiency of the ventricle but does not normalize the diastolic stress. Recently, investigators have found that increased myocardial stress directly induces gene expressions in the cardiac myocytes that again lead to cardiac growth [37, 59]. Although hypertrophy is not a pathological but rather a physiological response of the heart to increased load, heart failure as a final form of hypertrophy is an obvious disease.

For patients with ventricular overload caused by aortic stenosis, or by aortic or mitral regurgitation, it is extremely important that the diseased valve is corrected before the myocardium has been irreversibly damaged ("Golden moment of surgery"). Patients undergoing surgical corrections of a diseased valve experience acute and large changes in chamber load, and the degree of normalization of the left ventricular size and function depends on the type and severity of the valvular disease. For example, patients with chronic aortic insufficiency have higher postoperative morbidity and mortality rates than patients with other valvular diseases. Investigators have therefore estimated myocardial stress in an attempt to predict irreversible cardiac dilatation and failure in valvular diseases [38, 45, 63, 69, 70, 72, 73].

## 1.2 Oxygen consumption, external work and efficiency

The oxygen consumption of the myocardium can be divided into a load-independent part and a load-dependent part [68]. The load-independent part is related to the  $Ca^{++}$  handling for excitation-contraction coupling and to basal metabolism to maintain myocardial viability, whereas the load-dependent part is due to production of adenosine triphosphate (ATP) that is used for generation of mechanical energy by the contractile machinery (sarcomeres).

Investigators have shown that the oxygen consumption is highly related to myocardial stress [33, 36, 65] and to the pressure-volume area (PVA) defined as external work (EW) plus potential energy (PE) (Fig. 1) [67], but not to external work alone [19]. A given amount of external work at high pressures and low stroke volumes requires more oxygen than the same amount of external work at low pressures and high stroke volumes, i.e., the efficiency of the chamber depends on the external load. The greater energy demand of pressure work over volume work is of clinical importance, especially in patients with aortic stenosis, where left ventricular oxygen consumption is increased during systole, but coronary perfusion pressure is normal (or reduced) because of the pressure drop across the diseased valve.

### 1.3 The arterial tree

The functional properties of the arterial system are major determinants of aortic pressure, and thereby ventricular load. During aging, both the aortic mean pressure and pulse pressure increase. The increase in mean pressure is attributable to an increase in peripheral resistance; which is probably due to a decrease in the number of arterioles [24]. The increase in pulse pressure is attributable to two separate mechanisms of arterial stiffening [44]:

- An increase in aortic stiffness causes an increased rise in pressure during early ejection.
- An increase in pulse wave velocity gives an earlier return of the reflected wave responsible for a second rise in pressure during late ejection.

The stiffening of the arteries, such as seen in old adults, therefore increases the pressure at peak ejection and causes the pressure to rise further as the reflected wave returns during systole (right panel of Fig. 2). On the other hand, in young adults, the reflected wave returns both in late systole and early diastole (left panel of Fig. 2). The return of the reflected wave in early diastole is favorable because this boosts coronary perfusion. The difference in shape of the two pressure waveforms shown in Fig. 2 is of course also influenced by the state of the left ventricle in the two cases.

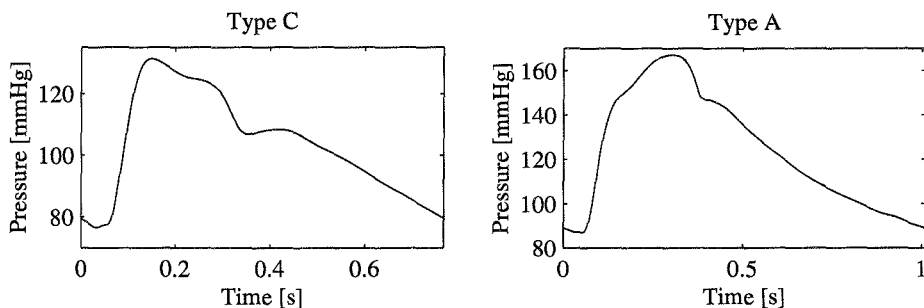


**Figure 2:** Calibrated carotid diameter waveforms from a young adult of age 25 (type C) and an old adult of age 62 (type A). The diameter waveforms were calibrated by systolic and diastolic brachial arterial pressures. The diameters were measured by the wall-tracking technique described in **paper C**.

Regarding afterload, some investigators have pointed out that the stresses in the myocardium depend on a mixture of cardiac and external factors, partly the physiological properties of the myocardial muscle fibers, and partly the physical properties of the arterial tree [41]. For example, the physical properties of the arterial tree ensure that the more rapidly the ventricle tries to eject blood, the higher the ventricular pressure

(or myocardial stress) becomes. Therefore, these investigators claim that afterload is best represented as the functional properties of the arterial system expressed as the frequency spectrum of the aortic input impedance:  $Z(\omega) = P(\omega)/Q(\omega)$ , where  $P$  and  $Q$  are the frequency representations of aortic pressure and flow, and  $\omega$  is the angular frequency.

## 2 Aims of the study

A reliable determination of ventricular load is important for correct treatment of patients with volume or pressure overloaded hearts. Aortic pressure, myocardial stress as well as arterial pulse wave velocity are related to ventricular load, and are therefore of interest.

Aortic pressure has been used as a measure of left ventricular load. We therefore wanted to develop and evaluate methods for estimating aortic pressure. Since arterial pressure and diameter are related, we focus on an ultrasound-based technique for measuring arterial diameter. The aortic pressure can then be estimated by calibrating diameter measurements of, e.g. the carotid artery. However, because of wave propagation and reflections, the aortic and carotid pressure waveforms have different shapes. Recently, a model study of a method for estimating central aortic pressure from measurements of carotid pressure and flow has been published. The method has not been validated experimentally. We therefore wanted to evaluate this method on data from dog experiments.

The left ventricular load has also been defined in terms of myocardial stress, since the loading conditions of the myocardial muscle fibers depend on both ventricular pressure and geometry. Hence, we wanted to develop a mathematical model for estimating myocardial stress. In addition to ventricular pressure, such a model requires measurements of the left ventricular geometry. The recently introduced tissue Doppler modality may make contour detection in ultrasound images more reliable, and we wanted to develop and evaluate a contour-detection algorithm that utilizes both gray-scale and tissue Doppler information.

In old adults, the increase in pulse pressure, and thereby ventricular load, is partly attributable to an increase in arterial pulse wave velocity, since an increase in pulse wave velocity gives an earlier return of the reflected wave. We therefore wanted to derive and evaluate a new method of estimating pulse wave velocity from carotid diameter and blood velocity measurements.

### 3 Estimation methods

#### 3.1 Aortic pressure estimation

Aortic and ventricular pressures are most reliably measured by invasive catheter-tipped micro-manometers. However, aortic pressure may also be estimated by non-invasive techniques. In patients without aortic stenosis, the ascending aortic pressure and the left ventricular pressure are nearly identical throughout ejection.

The central aortic pressure has been estimated by calibrating carotid or subclavian pulse tracings by systolic and diastolic brachial arterial pressures [1, 14]. Examples of calibrated carotid diameter measurements are shown in Fig. 2. In these examples, the carotid diameter was measured by applying the wall-tracking method described in **paper C**. When calibrating diameter waveforms to obtain pressure, the underlying assumption is that there is a linear relation between the pressure and diameter. This may not be the case. An alternative technique for measuring peripheral pulse waveforms is applanation tonometry [34, 35]. However, applanation tonometry is sensitive to the hold-down force and the transducer positioning and orientation and applies best to arteries with a bone underneath, such as the radial artery [18].

The pressures at the subclavian, carotid and radial arteries are different from the central aortic pressure because of wave propagation and reflections (Fig. 3). Investigators have therefore introduced methods to estimate the central aortic pressure from radial pressure through generalized transfer functions [13], or from carotid (or brachial) pressure by individual transfer functions [64]. The latter method has only been evaluated by means of simulations. Thus, in **paper E**, we perform an experimental evaluation of the individual transfer function approach.

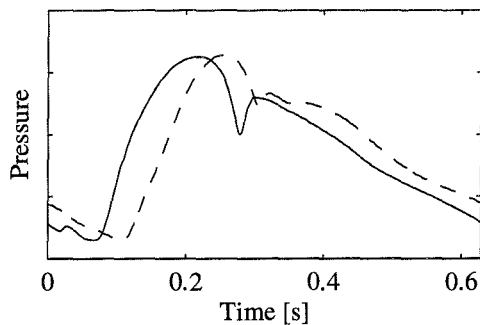


**Figure 3:** Aortic (—) and carotid (- - -) pressure waveforms measured by catheter-tipped micro-manometers in a dog.

### 3.2 Myocardial stress estimation

Direct measurements of wall stress with a force/pressure transducer inserted into the wall are difficult because the transducer damages the tissue at the site of measurement [29]. To estimate myocardial stress, investigators commonly use mathematical models, such as the one described in **paper A**, together with measurements of left ventricular geometry and pressure. To obtain left ventricular geometry and pressure non-invasively, methods such as the ones described in **papers B** and **C** are typically used.

#### Stress equations based on force balance analysis

The first class of models is based on expressing the equilibrium between the myocardial stresses and ventricular pressure (force balance models). The main advantage of this approach is that no constitutive relation between myocardial stress and strain is needed. In **paper A**, a model of this type is developed. The main weaknesses of the force balance approach, are the assumptions of axis-symmetry and constant myocardial stress across the wall. In addition, bending moments in the myocardium are neglected.

Three influential examples of the force balance approach are the equations of Sandler and Dodge [58], Falsetti et al. [20] and Mirsky [42]. These models, which are based on the assumptions that the myocardium is homogeneous, isotropic and ellipsoidal in shape, have been used extensively in clinical research.

At a position inside the myocardium, the total stress  $T$  includes both the pressure field  $p$  developed by more external material fibers (intramyocardial pressure) and the stress  $\sigma$  supported by the material fibers, i.e., the intramyocardial pressure acts against the stress supported by the material fibers:  $T = -p + \sigma$ . Regen [53] has pointed out that the equations of Sandler and Dodge [58], Falsetti et al. [20] and Mirsky [42] estimate the total stress, excluding ambient pressure but including the intramyocardial pressure. What should be estimated is the stress supported by the material fibers, excluding the intramyocardial pressure. In the case of Sandler and Dodge [58] and Falsetti et al. [20], the error occurred because pressure was assumed to act only on the cavity surface, so that all forces in the wall were attributed to myocardial fiber stress.

When assuming a homogeneous, isotropic and ellipsoidal ventricle (Fig. 4), the correct equations for estimating circumferential ( $\sigma_u$ ) and meridional ( $\sigma_v$ ) stresses supported by the material fibers are as follows [52]:

$$\sigma_u = p_{lv} \frac{a_m}{2h_e} \left( 2 - \frac{a_m^2}{b_m^2} \right) \quad (1)$$

$$\sigma_v = p_{lv} \frac{a_m}{2h_e} \quad (2)$$

where  $p_{lv}$  is the left ventricular pressure,  $h_e$  is wall thickness at equator,  $a_m = (a_o - a_i)/(\ln a_o - \ln a_i)$  and  $b_m = (b_o - b_i)/(\ln b_o - \ln b_i)$ . The subscripts  $i$  and  $o$  denote inner and outer walls, respectively.

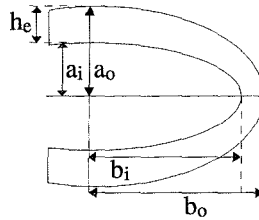


**Figure 4:** Illustration of an ellipsoidal ventricle.  $a_i$  = minor axis (inner wall).  $a_o$  = minor axis (outer wall).  $b_i$  = major axes (inner wall).  $b_o$  = major axis (outer wall).  $h_e$  = equatorial wall thickness.

In the late 70s, the concept of fiber stress was introduced [5, 12, 61]. The myocardium was assumed to be a soft incompressible material embedding muscle fibers that support forces in their longitudinal direction only. Arts et al. [4] showed that the volume-averaged fiber stress of a rotationally symmetric ventricle depends only on the ventricular pressure and the ratio of cavity to wall volumes. Investigators later showed that it is possible to estimate regional stress in rotationally symmetric ventricles by using similar approaches [16, 49, 54].

### Models based on non-linear finite elasticity

Today, the major research activity in cardiac mechanics is directed towards computational methods, the reason being advances in computer hardware and numerical methods, particularly the finite element method. Models based on the finite element method have included the fibrous structure of the myocardium, realistic chamber geometry, physiological stress-strain relations and large deformations [9, 15, 23, 32, 39, 43, 56]. By use of finite element models, the investigators have gained insight in basal physiology. For example, Rijcken et al. [57] found support for the hypothesis that the fiber orientation, during ejection, is optimized for maximum homogeneity of fiber strain.

The finite element approach gives myocardial stress and strain estimates. As opposed to the force balance models, the finite element models can estimate regional stress and strain distributions across the wall of non-symmetric ventricles. In addition to ventricular pressure and geometry, these models require knowledge of the myocardial fibrous structure [40, 66], and passive [17, 30, 62] and active [6, 31] stress-strain relations. However, stress and strain estimates from finite element models must be regarded with caution since the distribution of stress and strain is sensitive to the choice of fibrous structure, and passive and active material laws. The exact values of the parameters of the passive material law are generally unknown, and the passive stress-strain relation may also change during disease. Further, reliable models of the auxotonic (simultaneous change in stress and strain) contraction-relaxation sequences observed in the intact myocardium are also difficult to develop. Active material laws

are typically based on knowledge from isolated muscle (papillary or trabeculae) experiments that have mainly been performed in isometric (constant length) or isotonic (constant force) conditions, or as quick load and length clamps.

### 3.3 Pulse wave velocity estimation

#### Time-delay method

Pulse wave velocity has usually been measured by estimating the delay time between pressure or flow waveforms recorded simultaneously at two different positions along the vessel [10]. The delay time between the two waveforms equals the propagation time ( $\Delta t$ ) and is best estimated by detecting the upstroke (foot) of the waveforms. When the distance ( $\Delta z$ ) between the two recording sites is divided by the propagation time, an estimate of pulse wave velocity is obtained, i.e.,  $c = \Delta z / \Delta t$ . Fig. 3, which shows the aortic pressure near the carotid inlet and the carotid pressure near the carotid bifurcation, illustrates this concept as there is a time delay between the aortic and carotid pressures. The same idea can be applied to ultrasound-based diameter measurements [7, 60]. Usually, the two diameter measurements are recorded by the same probe. Since the width of the probe (in the azimuth direction), and thereby the maximal distance between the two diameter measurements, is in the range 3-5 cm, this approach requires a high pulse repetition frequency so that the delay time between the waveforms can be precisely determined.

#### Wave equation: method 1

Propagation of pressure ( $P$ ) and flow ( $Q$ ) waves in the arterial system is governed by the wave equation [21]:

$$\frac{\partial^2 P}{\partial x^2} - \frac{1}{c^2} \frac{\partial^2 P}{\partial t^2} = 0 \quad (3)$$

where the pulse wave velocity  $c$  is given as:

$$c = \sqrt{\frac{\bar{A}}{\rho} \cdot \frac{1}{C_A}} \quad (4)$$

Here  $\bar{A}$  is mean cross-sectional area,  $\rho$  is blood density, and  $C_A = \partial A / \partial P$  is area compliance. A practical approach for determining the pulse wave velocity by Eq. 4 is to calculate the compliance as  $\Delta A / PP$ , where  $\Delta A$  is the difference between systolic and diastolic areas, and  $PP$  is the pulse pressure. Usually, the brachial pulse pressure is used as a substitute for the local pulse pressure.

### Wave equation: method 2

The function  $D(x, t) = f(t - x/c)$  satisfies Eq. 3 and represents a wave propagating with the velocity  $c$  in the direction of increasing  $x$ . By differentiating  $D(x, t)$  with respect to  $x$  and  $t$ , we see that the pulse wave velocity is also given as:

$$c = \frac{\partial D}{\partial t} \bigg/ \frac{\partial D}{\partial x} \quad (5)$$

Brands et al. [11] have recently presented an ultrasound-based technique that utilizes this property (Eq. 5). By calculating the temporal and spatial diameter gradients, during the reflection free period of the cardiac cycle, they obtain estimates of pulse wave velocity.

### Area-flow method

Pulse wave velocity can also be estimated from area and flow measurements directly by calculating the ratio of flow and area during the reflection free period of the cardiac cycle. **Paper D** describes this method.

## 4 Contributions

The main contributions of this work are summarized as follows:

- A force balance model for estimating muscle fiber stress in the left ventricular myocardium was developed (**paper A**). The model applies to rotationally symmetric left ventricles, and can be used for estimating regional fiber stress from measurements of regional wall thickness and radii of curvature, or equatorial fiber stress from measurements of equatorial wall thickness, and left ventricular diameter and long axis.
- A robust and efficient method for semiautomatic contour detection in ultrasound M-mode images was developed (**paper B**). The robustness of the method is ensured by utilizing both grey-scale and tissue Doppler data in a global contour optimization criterion. The global minimum of the criterion is efficiently found by using the computational attractive dynamic programming technique.
- A method for tracking the motion of vessel walls was evaluated (**paper C**). The tracking algorithm, which is an extension of the conventional auto-correlation method, is based on estimating both the mean Doppler frequency and the RF center frequency inside the observation window. This way the estimator bias and variance are reduced.
- A method (the area-flow method) for estimating pulse wave velocity was developed (**paper D**). To make the area-flow method applicable to non-invasive

ultrasound recordings, we also developed a method for estimating arterial flow from pulsed wave Doppler measurements of blood velocity.

- A lossless transmission line approach for estimating aortic pressure waveforms from measurements of carotid pressure and flow was evaluated on data from four dogs (**paper E**). To find possible explanations for the results of the lossless transmission line technique, we also evaluated a viscous transmission line model.

## 5 *In vivo* examples

This section shows some examples of *in vivo* measurements of left ventricular geometry, and estimates of aortic pressure and myocardial stress. The ultrasound recordings used in the following examples were recorded at the University Hospital in Trondheim by Johannes Soma, MD, PhD, and Stig Slørdahl, MD, PhD.

### 5.1 A healthy subject

Fig. 5 shows the results of an analysis of recordings from a 32-year-old healthy subject. In panel A, tracings of equatorial wall thickness  $W$ , and cavity diameter  $D$  and long axis  $L$  are shown. The geometrical data has been obtained by applying the semiautomatic contour-detection method described in **paper B** in a standard parasternal M-mode and in two synthetic M-modes generated from an apical four chamber cineloop. Three to five cardiac cycles were averaged. The geometrical data shown in panel A illustrate the different phases of the cardiac cycle:

1. Systole: wall thickening, and diameter and long-axis shortening.
2. Early relaxation: quick wall thinning, and diameter and long-axis lengthening.
3. Diastasis: minor changes in wall thickness, diameter and long axis.
4. Atrial contraction: wall thinning, and diameter and long-axis lengthening.

In panel B, strain estimates are shown. The transmural, circumferential and longitudinal strains were calculated as:

$$\varepsilon_w = \frac{W(t)}{W(t_0)} - 1 \quad (6)$$

$$\varepsilon_u = \frac{D(t) + W(t)}{D(t_0) + W(t_0)} - 1 \quad (7)$$

$$\varepsilon_v = \frac{L(t)}{L(t_0)} - 1 \quad (8)$$

where  $t_0$  is the time of the R-peak of the ECG. The peak transmural strain is much higher than the circumferential and longitudinal strains.

The aortic pressure, estimated by calibrating carotid diameter measurements with systolic and diastolic brachial arterial pressures, is shown in panel C. The carotid diameter was measured by the method described in **paper C**. Three to five cardiac cycles were averaged.

Myocardial stress estimates during the ejection are shown in panel D. The stress was calculated by applying Eq. 12 of **paper A**. The peak stress was twice as high as the end-ejection stress.

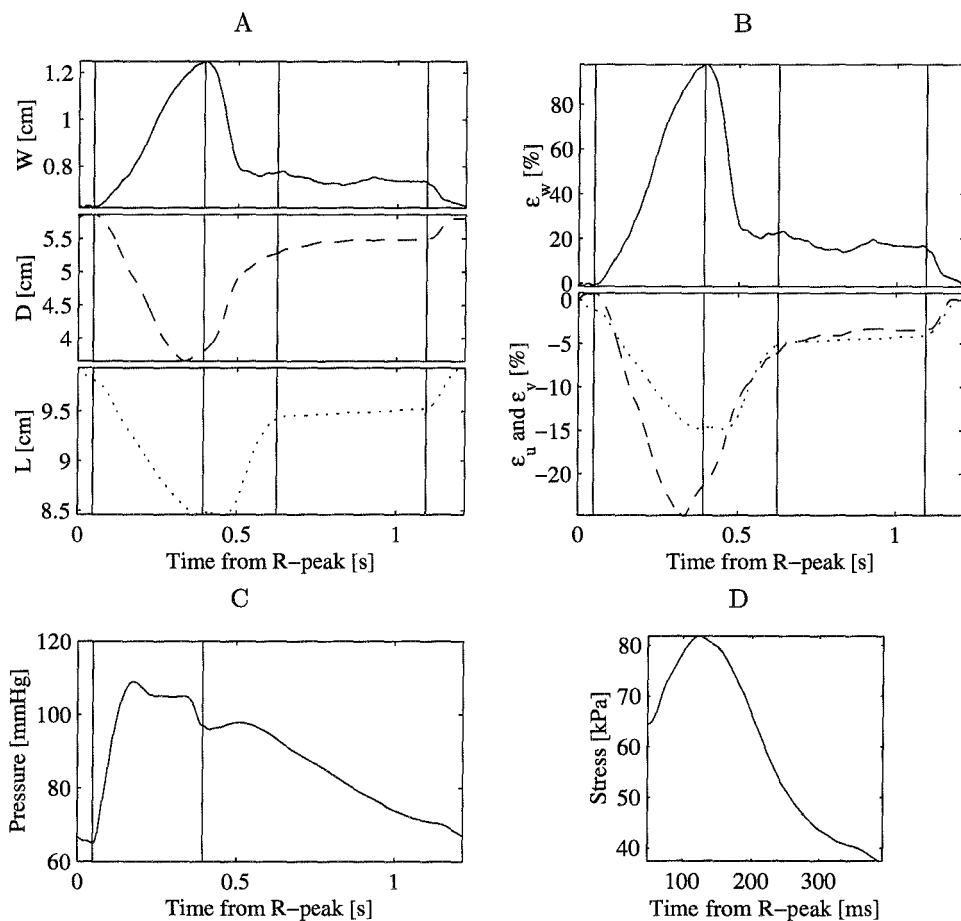


**Figure 5:** Non-invasive measurements from a 32-year-old healthy subject. Panel A: equatorial wall thickness (—), left ventricular diameter (- - -) and long axis (···). Panel B: transmural (—), circumferential (- - -) and longitudinal (···) strains. Panel C: aortic pressure estimates. Panel D: equatorial stress estimates (—) during ejection.

## 5.2 A patient with post-infarction failure

Fig. 6 shows the results of an analysis of recordings from a 71-year-old male with heart failure due to myocardial infarction in parts of the inferior wall. Secondary to the post-infarction dilatation of the left ventricle, the patient had a moderate mitral valve insufficiency.

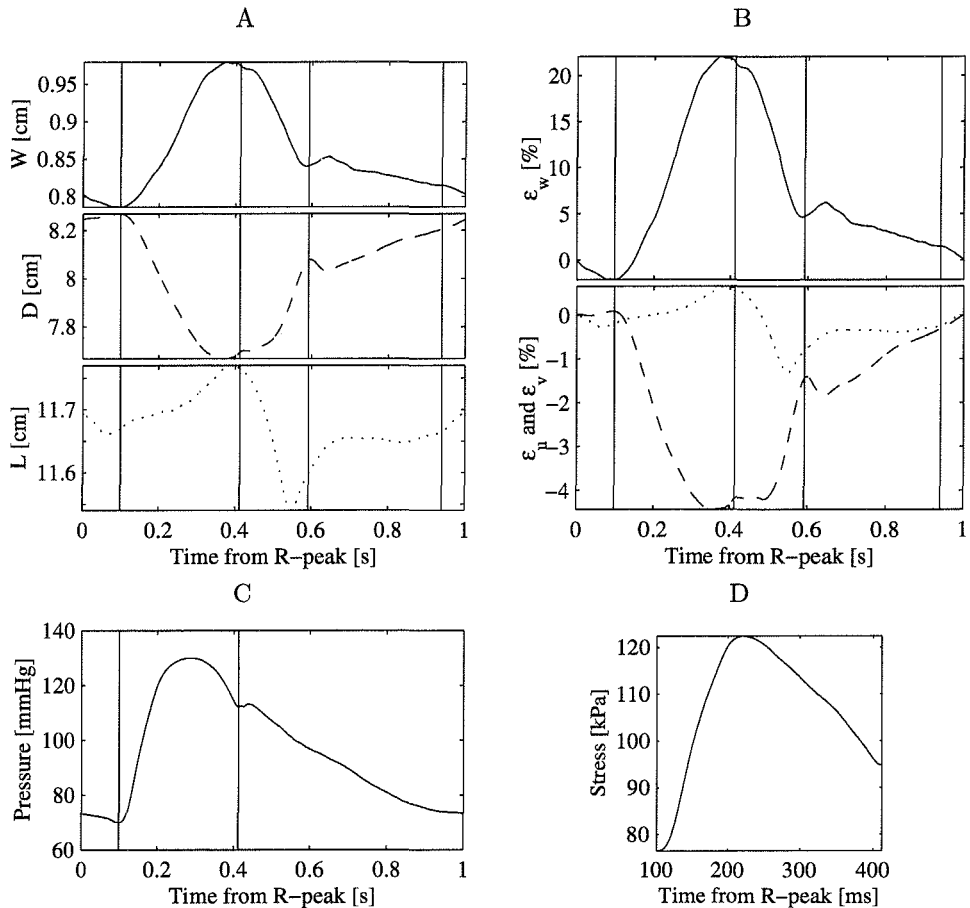


**Figure 6:** Non-invasive measurements from a 71-year-old patient with heart failure due to myocardial infarction. The content of each panel is described in the legend for Fig. 5

The most striking findings were the large diameter, the reduced wall thickening and diameter shortening during contraction and the abnormal long axis contraction pattern (panel A and B). The excursion of the mitral ring was only 2–3 mm (panel

A), which is much lower than a normal excursion of 13–16 mm. Actually, the left ventricular long axis lengthened during ejection and shortened after ejection, which is just opposite of the normal contraction pattern. This indicates that the whole long-axis function of the ventricle was lost. The myocardial stress was also high (panel D), probably due to the ventricular dilatation. Even though the patient had a myocardial infarction in parts of the inferior wall, his left ventricle was rotationally symmetric. The rotational-symmetry assumption of our force balance model was therefore fulfilled.

## 6 Concluding remarks and future directions

The main goal of this work was to develop and evaluate ultrasound-based techniques for determining hemodynamic parameters related to left ventricular load, such as myocardial stress, aortic pressure and pulse wave velocity.

### Myocardial stress estimation

Since the loading conditions of the myocardial muscle fibers depend on both left ventricular pressure and geometry, we developed equations for estimating myocardial stress from measurements of pressure and geometry (**paper A**).

The main advantage of this kind of modeling is that the resulting stress equations do not depend on any assumptions about the relation between stress and strain. However, the modeling approach is based on the simplified view that the myocardium is a soft incompressible material embedding muscle fibers that support stress only in their longitudinal direction. This may only be true in the systolic phase of the cardiac cycle, when the stresses in the muscle fibers are large compared to the stresses in the collagen network. Further, the modeling approach is also based on assuming a rotational symmetric ventricle, and this may not be the case in some of the patients with myocardial infarction. The stress equations should therefore be used mainly on patients with symmetric diseases, such as pressure or volume overloads.

An important property of a stress equation is that it is sensitive to changes in the true myocardial stresses. Unfortunately, we can not validate the stress estimates because myocardial stresses cannot be measured [29]. However, for use in clinical research, it is sufficient that the estimated stress is correlated to the true stress, the estimated stress does not have to equal the true stress.

The clinical usefulness of the stress-estimation method also depends on the inter- and intra-examiner reproducibility. The variation of repeated estimates must be so small that differences in myocardial stress between two patient groups are detectable. The variability of repeated estimates depends on two factors: 1) the variability of the ultrasound recordings, and 2) the variability of the examiner's analysis for determining ventricular pressure and geometry from the ultrasound recordings.

In the case of equatorial stress estimates, we have tried to reduce the variability of

the examiner's analysis by introducing semiautomatic methods for contour detection in M-mode images (**paper B**). However, the variability of the ultrasound recordings may highly affect the repeatability of the estimates. Therefore, in future studies, a full inter- and intra-examiner reproducibility analysis should be performed as described by Bland [8].

The usefulness of a stress-estimation method in clinics is influenced by the time requirements of the method. Because clinicians have limited time, myocardial stress must be estimated with as little effort as possible. When using the semiautomatic methods of **papers B** and **C**, the whole process of estimating equatorial stress can be done in 2–3 minutes.

In the case of regional stress estimates, the method requires measurements of regional wall thickness and principal curvatures. Estimations of regional radii of curvature are based on noise-sensitive second derivatives and may be difficult to estimate from medical image data. Estimation of regional stress from *in vivo* data has therefore not been given priority during this research project. However, medical imaging techniques are constantly improving, and studies for obtaining local wall thickness and principal curvature from 3D magnetic resonance or ultrasound data should be performed in future research.

## Measurements of the global geometry of the left ventricle

To be able to measure the global geometry of the left ventricle (wall thickness, diameter and long axis), we developed a robust and efficient method for semiautomatic contour detection in ultrasound M-mode images (**paper B**). We validated the method in 19 healthy subjects by comparing computer-generated contours with contours manually outlined by four echocardiographers.

The contour-detection method is time-efficient. On a 266 MHz Pentium II, it takes only 2–3 seconds to detect the contour in three to four cardiac cycles. This makes the method very useful in clinical work.

One limitation with the contour-detection method is that the ultrasound beam (M-line) must be approximately perpendicular to the wall being segmented. In 16 of 19 subjects examined, the echocardiographer was able to obtain adequate M-line directions. However, the effect of this limitation has to be studied further.

No intraobserver analysis was performed in the contour-detection study. Since the contour-detection method is semiautomatic, we expect the reproducibility to be higher for the contour-detection method than for manual outlining. Ideally, the contour-detection method requires only one operator-dependent decision: the selection of the initial point. In addition, the method may require algorithmic optimization and manual corrections of the detected contour.

## Arterial diameter measurements

To be able to estimate aortic pressure waveforms and pulse wave velocities, we wanted to measure arterial diameters. In **paper C**, we therefore evaluated a wall-tracking algorithm that is based on estimating both the mean Doppler frequency and the RF center frequency (modified auto-correlation method). In addition to the modified auto-correlation method, we analyzed the conventional auto-correlation method and two cross-correlation methods. Under the specific simulation conditions considered, the modified auto-correlation method had the lowest bias of all methods, and a variance in the same range as the cross-correlation methods. Compared to the cross-correlation methods, the modified auto-correlation method has lower complexity in terms of number of computations and sampling rate requirements, and is therefore the preferred choice of method.

A wall-tracking algorithm based on displacement estimators such as the ones compared in **paper C**, can be categorized as a local segmentation algorithm. In each time-step the tracking of the wall is based on a local criterion, i.e. the displacement estimate. Local segmentation algorithms are usually very fast, but future consequences of the local choices are not evaluated. This makes the local algorithms vulnerable to noise, and in some cases the method might track outside the wall. The contour-detection method presented in **paper B** is an example of a global segmentation algorithm. In future research, we ought to develop wall-tracking algorithms that take into account the global aspect of the problem.

## Aortic pressure estimation

The aortic pressure can be estimated by measuring the diameter waveforms (**paper C**) of the carotid or subclavian arteries and calibrating these with systolic and diastolic brachial arterial pressures (Fig. 2). The correctness of this approach depends on the linearity of the pressure-diameter relation within the operating range. A potentially more correct method is to calibrate applanation tonometer measurements [34, 35]. However, for the carotid and subclavian arteries, we believe that the repeatability of diameter measurements by ultrasound is better than the repeatability of applanation tonometry because applanation tonometry is very sensitive to the hold-down force and the transducer positioning and orientation [18] and because diameter recordings can be guided by two-dimensional ultrasound imaging [7, 27]. To see if this presumption is correct, a study where we compare carotid diameter and tonometer measurements with catheter-tipped micromanometer measurements of the aortic pressure must be performed.

Another advantage of the diameter measurement technique over tonometry is that it can be used to measure the diameter of the thoracic aorta. This is a preferable approach because the aortic and carotid pressure waveforms are different due to wave propagation and reflections (Fig. 3). However, the non-linearity of the pressure-diameter relation is still a potential problem, and has to be studied in humans by comparing the aor-

tic diameter waveforms with invasive pressure waveforms obtained by catheter-tipped micromanometry.

In **paper E**, a novel technique [64] for estimating aortic pressure directly from carotid measurements was evaluated on data from four dogs. Unfortunately, the technique, which is based on a lossless transmission line approach, did not give reliable reconstructions of the aortic pressure in the four dogs examined. This was probably due to the small diameters of the dog carotid arteries (2.0–2.5 mm), causing considerable attenuation. The key question is: Does the technique of Stergiopoulos et al. [64] work on data from human subjects? In humans, the viscous losses are lower than in dogs, due to humans' larger carotid diameters (5–7 mm). It is therefore important to test the technique further on human data.

### Pulse wave velocity estimation

In **paper D**, we derived and evaluated a new method of estimating pulse wave velocity from carotid diameter and blood velocity measurements (area-flow method). To make the area-flow method applicable to non-invasive ultrasound recordings, we also developed a method for estimating arterial flow from pulsed wave Doppler measurements of blood velocity. On a per subject basis, discrepancies were observed between the area-flow method and a comparison method when the methods were applied on data from 21 humans and four dogs. The per subject differences between the methods were difficult to explain. In an *in vitro* pump model as the one used by Brands et al. [11], we could evaluate both the flow estimation technique and the area-flow method. The flow estimates should be validated against electromagnetic or Doppler transit-time flow measurements, whereas the area-flow method should be compared to the alternative methods for estimating pulse wave velocity described in Section 3.3.



# References

1. Aakhus S, Torp H, Haugland T, Hatle L. Non-invasive estimates of aortic root pressures: external subclavian arterial pulse tracing calibrated by oscillometrically determined brachial arterial pressures. *Clin Physiol* 1993;13:573–86.
2. Angelsen BA, Aakhus S, Rabben SI, Torp HG. Model-based estimation of vascular parameters: Evaluation of robustness and suitability of models. *Echocardiography* 1994;11:409–423.
3. Angelsen BA, Rabben SI, Irgens F, Støylen A, Eilertsen L, Soma J. Echocardiographic assessment of fiber stress and strain - determination of transmural rotation of myofiber direction. In: *Invited lecture. 12th Symposium on Echocardiology and 9th meeting of the International Cardiac Doppler Society, 1997, Rotterdam, The Netherlands.* 1997; .
4. Arts T, Bovendeerd PHM, Prinzen FW, Reneman RS. Relation between left ventricular cavity pressure and volume and systolic fiber stress and strain in the wall. *Biophys J* 1991;59:93–102.
5. Arts T, Reneman RS, Veenstra PC. A model of the mechanics of the left ventricle. *Ann Biomed Eng* 1979;7:299–318.
6. Arts T, Veenstra PC, Reneman RS. Epicardial deformation and left ventricular wall mechanics during ejection in the dog. *Am J Physiol* 1982;243:H379–H390.
7. Benthin M, Dahl P, Ruzicka R, Lindstrom K. Calculation of pulse-wave velocity using cross correlation—effects of reflexes in the arterial tree. *Ultrasound Med Biol* 1991;17:461–9.
8. Bland M. *An introduction to medical statistics.* Oxford: Oxford University Press, 1987.
9. Bovendeerd PH, Arts T, Huyghe JM, van Campen DH, Reneman RS. Dependence of local left ventricular wall mechanics on myocardial fiber orientation: a model study. *J Biomech* 1992;25:1129–40.
10. Bramwell JC, Hill AV, McSwiney BA. The velocity of the pulse wave in man in relation to age as measured by hot-wire sphygmograph. *Heart* 1923;10:233–255.

11. Brands PJ, Willigers JM, Ledoux LA, Reneman RS, Hoeks AP. A noninvasive method to estimate pulse wave velocity in arteries locally by means of ultrasound. *Ultrasound Med Biol* 1998;24:1325-35.
12. Chadwick RS. Mechanics of the left ventricle. *Biophys J* 1982;39:279-288.
13. Chen CH, Nevo E, Fetets B, Pak PH, Yin FCP, Maughan WL, Kass DA. Estimation of central aortic pressure waveform by mathematical transformation of radial tonometry pressure. Validation of generalized transfer function. *Circulation* 1997; 95:1827-36.
14. Colan SD, Borow KM, Neumann A. Use of the calibrated carotid pulse tracing for calculation of left ventricular pressure and wall stress throughout ejection. *Am Heart J* 1985;109:1306-10.
15. Costa KD, Hunter PJ, Wayne JS, Waldman LK, Guccione JM, McCulloch AD. A three-dimensional finite element method for large elastic deformations of ventricular myocardium:II-prolate spheroidal coordinates. *J Biomech Eng* 1996;118:464-72.
16. DeAnda A, Komeda M, Moon MR, Green GR, Bolger AF, Nikolic SD, Daughters GT, Miller DC. Estimation of regional left ventricular wall stresses in intact canine hearts. *Am J Physiol* 1998;275:H1879-85.
17. Demer LL, Yin FC. Passive biaxial mechanical properties of isolated canine myocardium. *J Physiol Lond* 1983;339:615-30.
18. Drzewiecki GM, Melbin J, Noordergraaf A. Arterial tonometry: review and analysis. *J Biomech* 1983;16:141-52.
19. Evans CL, Matsuoka Y. The effect of various mechanical conditions on the gaseous metabolism and efficiency of the mammalian heart. *J Physiol* 1915;49:378-405.
20. Falsetti HL, Mates RE, Grant C, Greene DG, Bunnell IL. Left ventricular wall stress calculated from one-plane cineangiography, an approach to force-velocity analysis in man. *Circ Res* 1970;26:71-83.
21. Fung YC. *Biomechanics - Circulation*. New York: Springer-Verlag, 2nd ed., 1997.
22. Grossman W, Jones D, McLaurin LP. Wall stress and patterns of hypertrophy in the human left ventricle. *J Clin Invest* 1975;56:56-64.
23. Guccione JM, Costa KD, McCulloch AD. Finite element stress analysis of left ventricular mechanics in the beating dog heart. *J Biomech* 1995;28:1167-77.
24. Harper RN, Moore MA, Marr MC, Watts LE, Hutchins PM. Arteriolar rarefaction in the conjunctiva of human essential hypertensives. *Microvasc Res* 1978;16:369-72.

25. Hartford M, Wikstrand JC, Wallentin I, Ljungman SM, Berglund GL. Left ventricular wall stress and systolic function in untreated primary hypertension. *Hypertension* 1985;7:97-104.
26. Hellevik LR, Stergiopoulos N, Kiserud T, Rabben SI, Eik-Nes S, Irgens F. A mathematical model of umbilical venous pulsation. *J Biomech* 1999; Accepted.
27. Hoeks AP, Brands PJ, Smeets FA, Reneman RS. Assessment of the distensibility of superficial arteries. *Ultrasound Med Biol* 1990;16:121-8.
28. Hood WPJ, Rackley CE, Rolett EL. Wall stress in the normal and hypertrophied human left ventricle. *Am J Cardiol* 1968;22:550-8.
29. Huisman RM, Elzinga G, Westerhof N, Sipkema P. Measurement of left ventricular wall stress. *Cardiovasc Res* 1980;14:142-53.
30. Humphrey JD, Strumpf RK, Yin FCP. Biaxial mechanical behavior of excised ventricular epicardium. *Am J Physiol* 1990;259:H101-8.
31. Hunter PJ, McCulloch AD, ter Keurs HE. Modelling the mechanical properties of cardiac muscle. *Prog Biophys Mol Biol* 1998;69:289-331.
32. Huyghe JM, Arts T, van Campen DH, Reneman RS. Porous medium finite element model of the beating left ventricle. *Am J Physiol* 1992;262:H1256-67.
33. Johnson LL, Sciacca RR, Ellis K, Weiss MB, Cannon PJ. Reduced left ventricular myocardial blood flow per unit mass in aortic stenosis. *Circulation* 1978;57:582-90.
34. Kelly RP, Hayward C, Ganis J, Daley J, Avolio AP, O'Rourke M. Noninvasive registration of the arterial pressure pulse waveform using high-fidelity applanation tonometry. *J Vasc Med Biol* 1989;1:142-9.
35. Kemmotsu O, Ueda M, Otsuka H, Yamamura T, Winter DC, Eckerle JS. Arterial tonometry for noninvasive, continuous blood pressure monitoring during anesthesia. *Anesthesiology* 1991;75:333-40.
36. Kissling G, Rupp H, Malloy L, Jacob R. Alterations in cardiac oxygen consumption under chronic pressure overload. Significance of the isoenzyme pattern of myosin. *Basic Res Cardiol* 1982;77:255-69.
37. Komuro I, Yazaki Y. Control of cardiac gene expression by mechanical stress. *Annu Rev Physiol* 1993;55:55-75.
38. Kumpuris AG, Quinones MA, Waggoner AD, Kanon DJ, Nelson JG, Miller RR. Importance of preoperative hypertrophy, wall stress and end-systolic dimension as echocardiographic predictors of normalization of left ventricular dilatation after valve replacement in chronic aortic insufficiency. *Am J Cardiol* 1982;49:1091-100.
39. LeGrice IJ, Hunter PJ, Smaill BH. Lamina structure of the heart: a mathematical model. *Am J Physiol* 1997;272:H2466-76.

40. LeGrice IJ, Smaill BH, Chai LZ, Edgar SG, Gavin JB, Hunter PJ. Lamina structure of the heart: ventricular myocyte arrangement and connective tissue architecture in the dog. *Am J Physiol* 1995;269:H571–82.
41. Milnor WR. Arterial impedance as ventricular afterload. *Circ Res* 1975;36:565–70.
42. Mirsky I. Elastic properties of the myocardium: a quantitative approach with physiological and clinical applications. In: Berne RM, Sperelakis N, Geiger S, eds., *Handbook of Physiology, Section 2: The Cardiovascular System*, Baltimore, Maryland: Waverly Press, Inc., vol. 1. The Heart. 1979; 497–531.
43. Nielsen PMF, Grice BH, Smaill BH, Hunter PJ. Mathematical model of geometry and fibrous structure of the heart. *Am J Physiol* 1991;260:1365–1378.
44. O'Rourke MF, Kelly RP, Avolio AP. *The arterial pulse*. Philadelphia: Lea & Febiger, 1992.
45. Percy RF, Miller AB, Conetta DA. Usefulness of left ventricular wall stress at rest and after exercise for outcome prediction in asymptomatic aortic regurgitation. *Am Heart J* 1993;125:151–5.
46. Rabben SI, Bjærum S, Sørhus V, Torp H. Ultrasound-based vessel wall tracking: an auto-correlation technique with RF center frequency estimation. *Ultrasound Med Biol* 2000; Submitted.
47. Rabben SI, Eilertsen L, Støylen A, Soma J, Irgens F, Angelsen B. Non-invasive estimation of left ventricular myocardial fiber stress by using subclavian artery pulse tracings and M-mode echocardiography. In: *Computers in Cardiology, 1997, Lund, Sweden*. 1997; 165–168.
48. Rabben SI, Irgens F, Angelsen B. Approximate formula for myocardial fiber stress. In: *Joint meeting and tutorial course of the 19th congress of the European society for noninvasive cardiovascular dynamics and 13th congress of the cardiovascular system dynamics society, 1998, Gent, Belgium*. 1998; PII–9.
49. Rabben SI, Irgens F, Angelsen B. Equations for estimating muscle fiber stress in the left ventricular wall. *Heart Vessels* 1999; Accepted.
50. Rabben SI, Støylen A, Torp AH, Wisløff R, Angelsen B. Automatic boundary detection in ultrasound M-mode images. In: *Euroecho 2: The second annual and plenary meeting of the working group on echocardiography of the ESC, 1998, Trieste, Italy*. vol. 15, 1998; S65.
51. Rabben SI, Torp AH, Støylen A, Slørdahl S, Bjørnstad K, Haugen BO, Angelsen B. Semiautomatic contour detection in ultrasound M-mode images. *Ultrasound Med Biol* 2000;26:287–296.
52. Regen DM. Myocardial stress equations: fiberstresses of the prolate spheroid. *J Theor Biol* 1984;109:191–215.

53. Regen DM. Calculation of left ventricular wall stress. *Circ Res* 1990;67:245-252.
54. Regen DM, Anversa P, Capasso JM. Segmental calculation of left ventricular wall stresses. *Am J Physiol* 1993;264:H1411-21.
55. Remme E, Sørhus V, Rabben SI, Støylen A, Angelsen B. Comparison of estimated central aortic blood pressure from carotid pulse curves obtained by arterial tonometry and volume distension recordings. In: *Joint meeting and tutorial course of the 19th congress of the European society for noninvasive cardiovascular dynamics and 13th congress of the cardiovascular system dynamics society, 1998, Gent, Belgium*. 1998; PII-10.
56. Rijcken J, Bovendeerd PH, Schoofs AJ, van Campen DH, Arts T. Optimization of cardiac fiber orientation for homogeneous fiber strain at beginning of ejection. *J Biomech* 1997;30:1041-9.
57. Rijcken J, Bovendeerd PH, Schoofs AJ, van Campen DH, Arts T. Optimization of cardiac fiber orientation for homogeneous fiber strain during ejection. *Ann Biomed Eng* 1999;27:289-97.
58. Sandler H, Dodge H. Left ventricular tension and stress in man. *Circ Res* 1963; 13:91-104.
59. Serneri GG, Modesti PA, Boddi M, Cecioni I, Paniccia R, Coppo M, et al. Cardiac growth factors in human hypertrophy. Relations with myocardial contractility and wall stress. *Circ Res* 1999;85:57-67.
60. Sindberg Eriksen P, Gennser G, Lindstrom K, Benthin M, Dahl P. Pulse wave recording—development of a method for investigating foetal circulation in utero. *J Med Eng Technol* 1985;9:18-27.
61. Skalak R. Approximate formulas for myocardial fiber stresses. *J Biomech Eng* 1982;104:162-163.
62. Smaill BH, Hunter PJ. Structure and function of the diastolic heart: material properties of passive myocardium. In: Glass L, Hunter PJ, McCulloch AD, eds., *Theory of Heart*, New York: Springer-Verlag. 1991; 1-29.
63. Smucker ML, Manning SB, Stuckey TD, Tyson DL, Nygaard TW, Kron IL. Pre-operative left ventricular wall stress, ejection fraction, and aortic valve gradient as prognostic indicators in aortic valve stenosis. *Cathet Cardiovasc Diagn* 1989; 17:133-43.
64. Stergiopoulos N, Westerhof B, Westerhof N. Physical basis of pressure transfer from periphery to aorta: a model-based study. *Am J Physiol* 1998;274(4 Pt 2):H1386-92.
65. Strauer BE. Myocardial oxygen consumption in chronic heart disease: role of wall stress, hypertrophy and coronary reserve. *Am J Cardiol* 1979;44:730-40.

66. Streeter DD. Gross morphology and fiber geometry of the heart. In: Berne RM, Sperelakis N, Geiger S, eds., *Handbook of Physiology, Section 2: The Cardiovascular System*, Baltimore, Maryland: Waverly Press, Inc., vol. 1. The Heart. 1979; 61–112.
67. Suga H. Total mechanical energy of a ventricle model and cardiac oxygen consumption. *Am J Physiol* 1979;236:H498–505.
68. Suga H, Takaki M, Matsubara H, Goto Y. Energy costs of PVA and Emax: constancy and variability. In: LeWinter MM, Suga H, Watkins MW, eds., *Cardiac Energetics: from Emax to Pressure-Volume Area*, Dordrecht, The Netherlands: Kluwer Academic Publishers. 1995; 1–15.
69. Taniguchi K, Nakano S, Kawashima Y, Sakai K, Kawamoto T, Sakaki S, Kobayashi J, Morimoto S, Matsuda H. Left ventricular ejection performance, wall stress, and contractile state in aortic regurgitation before and after aortic valve replacement. *Circulation* 1990;82:798–807.
70. Taniguchi K, Nakano S, Matsuda H, Shimazaki Y, Sakai K, Kawamoto T, et al. Timing of operation for aortic regurgitation: relation to postoperative contractile state. *Ann Thorac Surg* 1990;50:779–85.
71. Urheim S, Torp H, Edvardsen T, Olstad B, Rabben SI, Heimdal A, Angelsen B, Smiseth OA. Myocardial strain rate imaging: validation of a new Doppler method to quantify myocardial function. In: *Euroecho 2: The second annual and plenary meeting of the working group on echocardiography of the ESC, 1998, Trieste, Italy*. vol. 15, 1998; S39.
72. Wong CY, Spotnitz HM. Systolic and diastolic properties of the human left ventricle during valve replacement for chronic mitral regurgitation. *Am J Cardiol* 1981;47:40–50.
73. Zile MR, Gaasch WH, Carroll JD, Levine HJ. Chronic mitral regurgitation: predictive value of preoperative echocardiographic indexes of left ventricular function and wall stress. *J Am Coll Cardiol* 1984;3:235–42.

# Paper A



# Equations for estimating muscle fiber stress in the left ventricular wall

Stein Inge Rabben<sup>1</sup>, Fridtjov Irgens<sup>2</sup> and Bjørn Angelsen<sup>1</sup>

<sup>1</sup>Department of Physiology and Biomedical Engineering, NTNU, Trondheim, Norway

<sup>2</sup>MTF/Division of Applied Mechanics, NTNU, Trondheim, Norway

## Abstract

Left ventricular muscle fiber stress is an important parameter in cardiac energetics. We hence developed equations for estimating regional fiber stresses in rotationally symmetric chambers, and equatorial and apical fiber stresses in prolate spheroidal chambers. The myocardium was modeled as a soft incompressible material embedding muscle fibers that support forces only in their longitudinal direction. A thin layer of muscle fibers then contributes with a pressure increment determined by the fiber stress and curvature. The fiber curvature depends on the orientation of the fibers, which varies continuously across the wall. However, by assuming rotational symmetry about the long axis of the ventricle and including a longitudinal force balance, we obtained equations where fiber stress is completely determined by the principal curvatures of the middle wall surface, wall thickness and cavity pressure. The equations were validated against idealized prolate spheroidal chambers, whose wall thicknesses are such that the fiber stress is uniform from the equator to apex. Because the apex is free to rotate, the resultant moment about the long axis of the LV must be zero. By using this constraint together with our fiber stress equations, we were able to estimate a muscle fiber orientation distribution across the wall that was in qualitatively agreement with published measurements.

Accepted for publication in Heart and Vessels

## 1 Introduction

In medical research, left ventricular (LV) wall stress has been used to analyze myocardial oxygen consumption [20], LV systolic function [3] and hypertrophy caused by pressure or volume overloads [6, 8].

Direct measurements of wall stress with a force/pressure transducer inserted into the wall are difficult because the transducer damages the tissue at the site of measurement [11]. The approach has thus been to estimate wall stress by using mathematical models together with measurements of LV pressure and geometry.

Equations for estimating stresses in idealized chambers have been published. With such equations, stresses in spheres and cylinders, stresses at the equator and apex of prolate spheroids, and volume-average stresses in rotationally symmetric chambers can be calculated [1, 15, 16]. Since the left ventricle is not shaped perfectly as a sphere, cylinder or prolate spheroid, and neither equatorial stress nor volume-averaged stress is sufficient for analyzing heterogenic stress patterns, Regen et al. [17] developed a method for estimating regional stress in rotationally symmetric chambers. The method is based on measurements of LV pressure, local wall thickness and local radii of curvature and estimates stresses in the meridional direction and in the direction orthogonal to the meridian.

However, the direction of the myocardial muscle fibers is neither meridional nor orthogonal to the meridian, since the direction of the muscle fibers changes transmurally [22]. There is hence a need for an expression relating stress in the muscle fibers (fiber stress) to LV pressure and local geometry.

For the active myocardium where the muscle fiber stress is much higher than the stresses in the connective tissue, we may assume the myocardium to be a soft incompressible material embedding muscle fibers that support forces only in their longitudinal direction [2]. Under this assumption, Skalak [19] developed a formula for fiber stress that depends on mean radius of fiber curvature. However, the radius of fiber curvature is generally unknown since it is determined by local geometry and fiber direction. Fortunately, in rotationally symmetric chambers, a longitudinal force balance may be included, and fiber stress can be estimated without knowing the transmural fiber direction. Arts et al. [1] thus showed that, in rotational symmetric chambers, volume-averaged fiber stress can be estimated from cavity pressure, cavity volume and wall volume only.

The main purpose of this study was to develop a fiber stress equation that is based on local geometry (i.e. local wall thickness and radii of curvature) instead of global geometry (i.e. cavity and wall volumes), so that regional fiber stresses can be estimated. Further, since local radii of curvature are based on noise sensitive second derivatives and may be difficult to estimate from medical image data, we also wanted to include equations that are based on prolate spheroidal geometry so that fiber stress may be estimated from measurements of LV wall thickness, diameter and long axis.

## 2 Materials and methods

### 2.1 Model

#### 2.1.1 Geometry

We use a set of orthogonal curvilinear coordinates  $(u, v, w)$  to describe a position in the myocardium (Fig. 1). The coordinate lines for  $u$  and  $v$  are chosen to coincide with the lines of the principal curvatures of isobars inside the myocardium, i.e. surfaces of constant intra-myocardial pressure. The  $u$  and  $v$  directions are along the directions of the major and minor principal curvatures, respectively, while the  $w$ -coordinate is in the outward direction of the isobar normals. It is assumed that the muscle fibers lie in a helical manner in a nested set of fiber layers, and that the muscle fiber layers coincide with the isobars. The angle between the main direction of the fibers in a layer and the  $u$ -direction is then denoted by  $\alpha$  (Figs. 1 and 2).

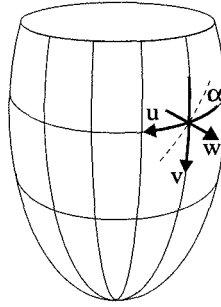


**Figure 1:** Isobaric surface.  $u$ , direction of major principal curvature.  $v$ , direction of minor principal curvature.  $w$ , outward direction of the isobar normal.

#### 2.1.2 Muscle fiber stress in a rotationally symmetric LV

Let us assume the myocardium to be a soft incompressible material embedding muscle fibers that support stress only in their longitudinal direction, and define fiber stress as the stress in the direction of the muscle fibers. Then the fiber stress  $\sigma$  results in the following normal and shear stresses in the  $u$  and  $v$  directions (Fig. 2):

$$\sigma_u = \sigma \cos^2 \alpha, \quad \sigma_v = \sigma \sin^2 \alpha, \quad \tau_{uv} = \frac{\sigma}{2} \sin 2\alpha \quad (1)$$

It follows from Eq. 1 that the sum of the two orthogonal normal stresses  $\sigma_u$  and  $\sigma_v$  equals the fiber stress:

$$\sigma = \sigma_u + \sigma_v \quad (2)$$

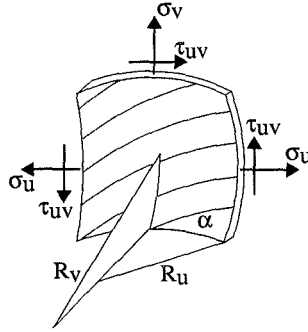


**Figure 2:** A fiber layer.  $\alpha$ , angle between the main muscle fiber direction and the u-coordinate. The fiber stress  $\sigma$  results in normal stresses  $\sigma_u$  and  $\sigma_v$  and shear stress  $\tau_{uv}$ .  $R_u$ , radius of curvature in the u-direction.  $R_v$ , radius of curvature in the v-direction.

A thin layer of unidirectional muscle fibers will contribute with a pressure increment determined by the stress and curvature of the fibers in that layer [19]:

$$-\frac{dp}{dw} = \frac{\sigma}{R} \quad (3)$$

where  $R$  is the radius of curvature of the fiber layer in the direction of the muscle fibers. Defining the principal radii of curvature at location  $(u, v)$  as  $R_u$  and  $R_v$  (Fig. 2), the radius of curvature of the fibers with a direction  $\alpha$  is then obtained by Euler's theorem [13]:

$$\frac{1}{R} = \frac{\cos^2 \alpha}{R_u} + \frac{\sin^2 \alpha}{R_v} \quad (4)$$

By inserting Eq. 4 into Eq. 3 and recognizing the numerators as normal stresses (Eq. 1), we obtain:

$$-\frac{dp}{dw} = \frac{\sigma_u}{R_u} + \frac{\sigma_v}{R_v} \quad (5)$$

which is Laplace's law. Using Eq. 2 we substitute the normal stress  $\sigma_u$ :

$$-\frac{dp}{dw} = \frac{\sigma}{R_u} + \left( \frac{1}{R_v} - \frac{1}{R_u} \right) \sigma_v \quad (6)$$

To substitute  $\sigma_v$  we need to develop a longitudinal force balance. For an LV that is rotationally symmetric around its long axis, the u-coordinate coincides with the circumferential direction, while the v-coordinate coincides with the meridional direction. A longitudinal force balance can then be developed for an arbitrary cross section of

the long axis. The meridional stress  $\sigma_v$  in the myocardial wall must counteract both the blood pressure  $p_{lv}$  in the LV cavity and the intra-myocardial pressure field  $p$ . With reference to Fig. 3 we define  $\psi$  as the angle between the surface normal of a fiber layer and a plane perpendicular to the long axis of the LV,  $r$  as the radius of the circle of intersection between the middle wall of the layer and a plane perpendicular to the LV long axis and  $\Delta w$  as the thickness of the layer. With inner pressure  $p_i$  and outer pressure  $p_o$ , the longitudinal force balance of the fiber layer is described by:

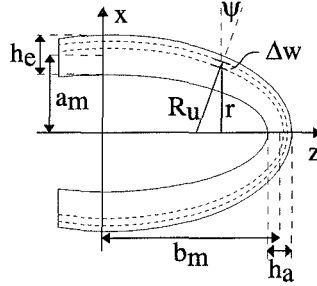


**Figure 3:** A longitudinal cross section of a rotationally symmetric chamber.  $\psi$ , angle between the surface normal of a fiber layer inside the myocardial wall and a plane perpendicular to the LV long axis.  $r$ , radius of the circle of intersection between the middle wall of the layer and a plane perpendicular to the LV long axis.  $\Delta w$ , thickness of the layer. A special case of a rotationally symmetric chamber is the prolate spheroidal chamber, which is described by the semi-axes  $a_m$  and  $b_m$  and the equatorial and apical wall thickness  $h_e$  and  $h_a$ .

$$p_i \pi \left( r - \frac{\Delta w}{2} \cos \psi \right)^2 = p_o \pi \left( r + \frac{\Delta w}{2} \cos \psi \right)^2 + 2\pi r \Delta w \left( \sigma_v - \frac{p_i + p_o}{2} \right) \cos \psi \quad (7)$$

By denoting  $\Delta p = p_o - p_i$  and letting  $\Delta w \rightarrow 0$ , we obtain from Eq. 7 the following differential equation:

$$-\frac{dp}{dw} = \frac{2\sigma_v}{R_u} \quad (8)$$

where we have used the relation  $\cos \psi = \frac{r}{R_u}$ . We can now substitute the meridional fiber stress  $\sigma_v$  in Eq. 6 by using Eq. 8. By solving the resulting expression with respect to  $\frac{dp}{dw}$ , we obtain:

$$-\frac{dp}{dw} = \frac{2\sigma}{R_u(3 - R_u/R_v)} \quad (9)$$

Note that the fiber direction angle  $\alpha$  is now eliminated from the model. At apex, all the meridians meet and  $R_v = R_u$ , and the right side of Eq. 9 becomes  $\frac{\sigma}{R_u}$ . Left ventricular

pressure may be calculated by integrating Eq. 9 along a path from the endocardium to the epicardium. For fixed  $(u, v)$  coordinates, a set of fiber layer normals can be defined, from the endocardium to the epicardium. Since we have assumed that the fiber layers coincide with the isobars, the fiber layer normals will in general not be parallel to each other. The principal radii of curvature of the fiber layers will hence not have common centers of curvature. However, to obtain an approximative expression for fiber stress, we assume that all the fiber layer normals are parallel to the middle wall of the myocardium. We define the middle wall as the reference layer ( $w = 0$ ), and  $R_{mu}$  and  $R_{mv}$  as the principal radii of curvature of the middle wall. We can then substitute  $R_u = R_{mu} + w$  and  $R_v = R_{mv} + w$  into Eq. 9. In general, the fiber stress varies for the different fiber layers, but when we assume homogeneous fiber stress across the wall ( $\sigma = \sigma_f$ ), and integrate the resulting expression from the endocardium ( $w = -h/2$ ) to the epicardium ( $w = h/2$ ), we obtain:

$$\sigma_f = p_{lv} \left[ \frac{2}{3} \ln \left( \frac{R_{mu} + h/2}{R_{mu} - h/2} \right) + \frac{1}{3} \ln \left( \frac{3R_{mv} - R_{mu} + h}{3R_{mv} - R_{mu} - h} \right) \right]^{-1} \quad (10)$$

where  $h$  is the wall thickness. To calculate fiber stress from Eq. 10 we must specify  $p_{lv}$ ,  $h$ ,  $R_{mu}$  and  $R_{mv}$ .

### 2.1.3 Muscle fiber stress in a prolate spheroid

Medical image data are often noisy, and it may be difficult to estimate the principal curvatures of the middle wall of the myocardium directly from the image data. Estimates of principal curvatures can be obtained by adapting a parametric model surface to the image data. A special case of a rotationally symmetric chamber is the prolate spheroidal chamber, which is an ellipsoid of revolution having a polar diameter of greater length than the equatorial diameter (Fig. 3). For a prolate spheroidal chamber, the principal radii of curvature of the middle wall at points with distance  $z$  from the equatorial plane are described by [24]:

$$\begin{aligned} R_{mu}(z) &= \left( 1 - \frac{\epsilon_m^2}{b_m^2} z^2 \right)^{\frac{1}{2}} a_m \\ R_{mv}(z) &= \left( 1 - \frac{\epsilon_m^2}{b_m^2} z^2 \right)^{\frac{3}{2}} \frac{b_m^2}{a_m} \end{aligned} \quad (11)$$

where  $a_m$  and  $b_m$  are the semi-axes of the spheroid (Fig. 3) and  $\epsilon_m$  is the eccentricity of the spheroid, i.e.  $\epsilon_m^2 = 1 - \frac{a_m^2}{b_m^2}$ . Inserting these expressions into Eq. 10, we get the

following formula for fiber stress at the equator ( $z = 0$ ) and apex ( $z = b_m$ ):

$$\sigma_{fe} = p_{lv} \left[ \frac{2}{3} \ln \left( \frac{a_m + \frac{h_e}{2}}{a_m - \frac{h_e}{2}} \right) + \frac{1}{3} \ln \left( \frac{3 \frac{b_m^2}{a_m} - a_m + h_e}{3 \frac{b_m^2}{a_m} - a_m - h_e} \right) \right]^{-1} \quad (12)$$

$$\sigma_{fa} = p_{lv} \left[ \ln \left( \frac{\frac{a_m^2}{b_m} + \frac{h_a}{2}}{\frac{a_m^2}{b_m} - \frac{h_a}{2}} \right) \right]^{-1} \quad (13)$$

where  $h_e$  and  $h_a$  are the wall thickness at the equator and apex (Fig. 3).

## 2.2 Validation

### 2.2.1 Uniform fiber stresses from the equator to apex

Because our regional stress equation (Eq. 10) depends on local measurements of curvature and wall thickness, it will generally not give uniform stresses from the equator to apex. However, Regen [15] found a prolate spheroidal chamber whose wall thickness is such that the average of the stresses in the meridional and the circumferential directions is uniform from the equator to apex. The sum of orthogonal stresses always equals the sum of the principal stresses. Hence, when we apply our regional stress equation on Regen's uniform-stress chamber, our equation must also estimate uniform stresses from the equator to apex. The relation between inner and outer axes of the uniform-stress chamber is given by [15]:

$$b_o^3 - b_i^3 = a_o^2 b_o - a_i^2 b_i \quad (14)$$

where  $a$  and  $b$  are the minor and major axes, while subscripts  $o$  and  $i$  denote outer and inner surfaces. In the same manner as Regen et al. [17], we set the chamber cavity ratio  $a_i/b_i$  to 0.5, equatorial cavity radius  $a_i$  to 2.5 cm, and equatorial wall thickness  $a_o - a_i$  to 1 cm. Eq. 14 then gave an apical wall thickness  $b_o - b_i$  of 0.432 cm. To test whether Eq. 10 complies with the uniform stress constraint (Eq. 14) we defined the middle wall surface as the prolate spheroid given by  $a_m = (a_i + a_o)/2$  and  $b_m = (b_i + b_o)/2$ , and calculated the relative fiber stress for different transverse sections between equator and apex. For each transverse section the radii of curvature were calculated by Eq. 11, while the wall thickness was calculated as the distance between the points where the normal of the middle surface intersects the inner and outer spheroids.

### 2.2.2 Volume-averaged stresses

The second validation aims at answering whether our stress equations agree with the work of Arts et al. [1]. They developed the formula  $\sigma_f = 3p_{lv}/\ln(1 + V_w/V_{lv})$ , where  $V_w$  is the LV wall volume and  $V_{lv}$  is the LV cavity volume. However, our equations depend on local geometry (Eq. 10) or spheroidal dimensions (Eqs. 12 and 13), and not

on LV cavity and wall volumes. Hence, for a chosen cavity volume  $V_{lv}$ , wall volume  $V_w$  and axis ratio  $\rho$ , the dimensions  $a_m$ ,  $b_m$ ,  $h_e$  and  $h_a$  were obtained by numerically solving the following set of equations:

$$\begin{aligned}
 V_{lv} - \frac{2}{3}\pi \left( a_m - \frac{h_e}{2} \right)^2 \left( b_m - \frac{h_a}{2} \right) &= 0 \\
 V_{lv} + V_w - \frac{2}{3}\pi \left( a_m + \frac{h_e}{2} \right)^2 \left( b_m + \frac{h_a}{2} \right) &= 0 \\
 \rho - \frac{a_m}{b_m} &= 0 \\
 V_w - \frac{2}{3}\pi \left[ \left( b_m + \frac{h_a}{2} \right)^3 - \left( b_m - \frac{h_a}{2} \right)^3 \right] &= 0
 \end{aligned} \tag{15}$$

The first two expressions relate the cavity volume ( $V_{lv}$ ) and the volume inside the outer surface ( $V_{lv} + V_w$ ) to the semi-axes and the equatorial and apical wall thickness. The third expression assures a specified chamber ratio, while the last expression is the uniform stress constraint (Eq. 14). Note that we have assumed in these equations (15) that the chamber is a prolate spheroid cut at equator, i.e. the volume is given by  $\frac{2}{3}\pi a^2 b$ .

To imitate an adult human left ventricle we chose the LV wall volume to 100 mL, and the chamber ratio  $a_m/b_m$  to 0.5. For relative cavity volumes  $V_{lv}/V_w$  ranging from 0.01-1 we solved the set of equations (15), the average fiber stress between the equator and apex  $\bar{\sigma}_f$  (Eq. 10), equatorial fiber stress  $\sigma_{fe}$  (Eq. 12), apical fiber stress  $\sigma_{fa}$  (Eq. 13) and volume-averaged fiber stress (Eq. 19 of Arts et al. [1]). The average stress  $\bar{\sigma}_f$  was calculated by averaging fiber stress estimates (Eq. 10) of 7 transverse sections from the equator to apex.

### 2.2.3 Muscle fiber direction

Morphological studies have shown that the fiber direction changes transmurally. In this section we present a method for determining two parameters of models describing the fiber direction angle  $\alpha$ . Comparison of this method to morphological studies may serve as a qualitative evaluation of the modeling.

Eq. 10 is an expression for fiber stress in the myocardium. An alternative expression can be developed by inserting Eq. 4 into Eq. 3, assuming homogeneous fiber stress and integrating the resulting expression from the endocardium to the epicardium. By equating these two alternative fiber stress equations, we get:

$$\int_{-h/2}^{h/2} \left( \frac{\cos^2 \alpha}{R_{mu} + w} + \frac{\sin^2 \alpha}{R_{mv} + w} \right) dw = \frac{2}{3} \ln \left( \frac{R_{mu} + \frac{h}{2}}{R_{mu} - \frac{h}{2}} \right) + \frac{1}{3} \ln \left( \frac{3R_{mv} - R_{mu} + h}{3R_{mv} - R_{mu} - h} \right) \tag{16}$$

which defines the first constraint imposed on a fiber direction model  $\alpha$ . Shear stresses in a cross section of the wall contribute to moments about the axis of revolution. Because the apex is free to rotate, the resultant moment about this axis must be zero. In a rotationally symmetric ventricle, the resultant moment is found by integrating the moment of the shear stress  $\tau_{uv}$  across the wall:

$$T = \int_{-h/2}^{h/2} (\tau_{uv}r) (2\pi r) dw = \sigma_f \pi \cos^2 \psi_m \int_{-h/2}^{h/2} \sin 2\alpha (R_{mu} + w)^2 dw \quad (17)$$

By equating this moment to zero, we get the second constraint imposed on the fiber direction:

$$\int_{-h/2}^{h/2} \sin 2\alpha (R_{mu} + w)^2 dw = 0 \quad (18)$$

Eqs. 16 and 18 serve as two constraints that a model of the fiber direction  $\alpha$  must fulfill. Some studies [9, 18] show an almost linear variation of the fiber direction across the wall:

$$\alpha = -\mu w + \alpha_m \quad (19)$$

where  $\alpha_m$  is the angle offset at the middle wall and  $\mu$  is a scaling factor. In other studies [7, 22] the investigators have measured an S-shaped fiber direction distribution across the wall. An inverted and scaled sine function is thus an alternative model for the muscle fiber direction:

$$\alpha = -\hat{\mu} \arcsin\left(\frac{2w}{h}\right) + \hat{\alpha}_m \quad (20)$$

where  $\hat{\alpha}_m$  is the angle offset at the middle wall and  $\hat{\mu}$  is a scaling factor. By inserting one of these alternative models (Eqs. 19 or 20) into Eqs. 16 and 18 and solving the resulting set of equations numerically, we are able to estimate the fiber angle variation across the wall.

To compare with a morphological study, we used the same end-systolic dimensions at equator as measured by Streeter et al. [23]; we set  $h$  to 1.2 cm,  $R_{mu}$  to 2 cm and  $R_{mv}$  to 9.2 cm.

#### 2.2.4 Assessment of choice of reference layer

When integrating Eq. 9 to obtain Eq. 10 we used the principal curvatures of the middle wall. In general, the inner and outer walls will not have the same centers of curvature as the middle wall. We thus made two alternative expressions to Eq. 10 by using 1) the inner wall and 2) the outer wall as reference layers when integrating Eq. 9. The new expressions were tested against Eq. 10 using the uniform-stress geometry presented above (Eq. 14).

### 3 Results

Table 1 shows the relative fiber stress at seven locations from the equator to apex. The left column of the table corresponds to the equator while the right column corresponds to the apex. The table confirms that the regional stress equation (Eq. 10) gives uniform stresses from the equator to apex when applying it on Regen’s uniform-stress chamber.

$z$	0	1.3500	2.6080	3.6883	4.5173	5.0383	5.2161
$\sigma_f/p_{lv}$	3.9703	3.9705	3.9711	3.9715	3.9706	3.9696	3.9716

**Table 1:** Relative fiber stress at seven locations between the equator and apex.  $z$ , the distance from the equator.

Fig. 4 shows relative fiber stresses  $\sigma/p_{lv}$  plotted against relative cavity volumes  $V_{lv}/V_w$ . The fiber stresses calculated by Eqs. 10, 12 and 13 and the volume-averaged fiber stress from the model of Arts et al. [1] are almost identical for all cavity volumes. The apical fiber stresses (Eq. 13) deviate most from the other stress estimates. However, the difference can only be seen at small cavity volumes (dotted line just above the solid lines). When calculating the relative fiber stresses we have set the axis ratio  $a_m/b_m$  to 0.5. However, other axis ratios gave identical results.

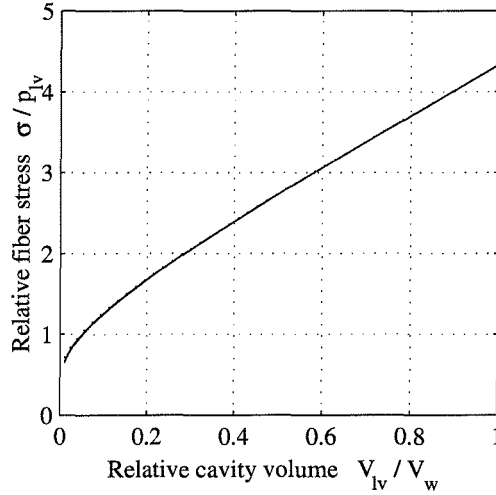
When calculating the parameters in the fiber angle formulas (Eqs. 19 and 20) as described in the method section, we obtained the parameters  $\mu = 97$  degrees and  $\alpha_m = 15.3$  degrees for the linear model and  $\hat{\mu} = 0.89$  and  $\hat{\alpha}_m = 14.8$  degrees for the non-linear model. In Fig. 5 the two models are plotted as a function of the  $w$  coordinate.

Fig. 6 shows the relative fiber stress at different locations from the equator to apex, when the middle (solid line), inner (dashed line) and outer walls (dash-dotted line) are used as reference layers. The fiber stresses are not uniform when the inner and outer walls are used as reference layers.

### 4 Discussion

We have developed equations for estimating regional fiber stress in rotationally symmetric chambers (Eq. 10) and equatorial and apical fiber stress in prolate spheroidal chambers (Eqs. 12 and 13). The equations have been validated against idealized prolate spheroidal chambers [15], whose wall thicknesses are such that the fiber stress is uniform from the equator to apex. In the first validation, the regional stress equation gave uniform stresses from the equator to apex (Table 1). In the second validation, the regional, equatorial and apical stress equations gave estimates identical to the volume-averaged stress of the model established by Arts et al. [1].

We also estimated the fiber orientation distribution across the wall (Fig. 5), using



**Figure 4:** Relative fiber stress  $\sigma/p_{lv}$  versus relative cavity volumes  $V_{lv}/V_w$ . The figure shows average fiber stress between the equator and apex  $\bar{\sigma}_f$  (Eq. 10), equatorial fiber stress  $\sigma_{fe}$  (Eq. 12), apical fiber stress  $\sigma_{fa}$  (Eq. 13) and volume-averaged fiber stress (Eq. 19 of Arts et al. [1]). The four relative stress curves are almost undistinguishable. The normal physiological range of the relative cavity volume is  $V_{lv}/V_w = 0.2 - 0.7$ .

end-systolic dimensional data from Streeter et al. [23]. The total fiber angle variation in their measurements was approximately 140 degrees, while the angle at the middle wall was slightly less than zero. In our calculations, the total fiber angle variation depends on the model chosen and was 116.4 degrees for the linear model and 160.9 degrees for the non-linear model. The angle at the middle wall will always be positive in our calculations, because the shear stresses in the subepicardium will contribute more effectively to the resultant moment than will the shear stresses in the inner part of the wall. A positive fiber angle at the middle wall (5 to 15 degrees) has been reported in some studies [9, 22].

In general, the fiber layers between the endocardium and the epicardium do not have common centers of curvature. Fig. 6 shows the effect of choosing the inner and outer walls as reference layers when Eq. 9 is integrated. The figure shows non-uniform stress when using the expressions based on the principal curvatures of inner or outer walls. It is thus important to choose the middle wall as reference layer when integrating Eq. 9.

The main advantage of modeling based on force balances is that the resulting stress equations do not depend on any assumptions about the relation between stress and strain. However, our approach is based on the simplified view that the myocardium is a soft incompressible material embedding muscle fibers that support stress only in

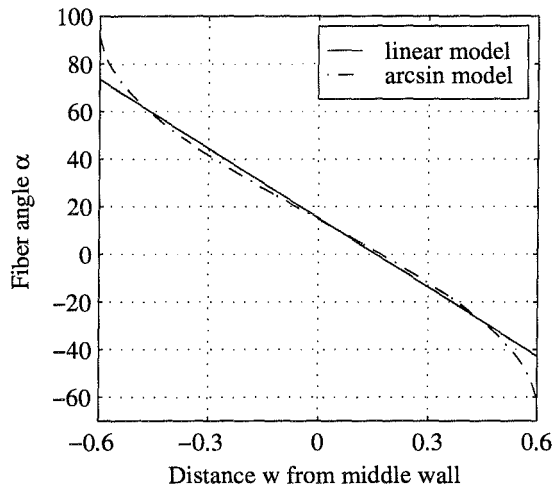


**Figure 5:** Plots of Eqs. 19 and 20 which describe the fiber angle variation across the wall. The parameter values of the equations are listed in the result section.

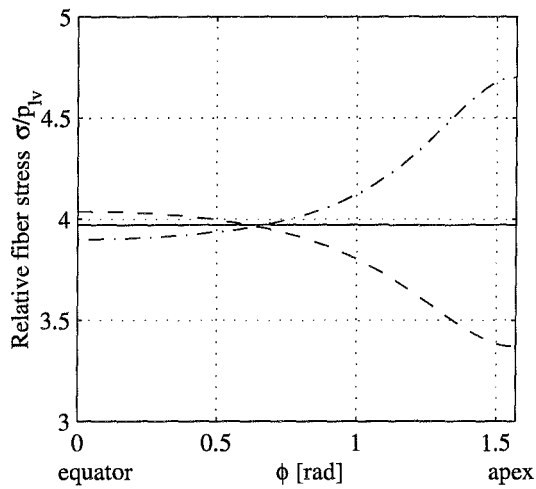


**Figure 6:** The relative fiber stress calculated when the middle (solid line), inner (dashed line) and outer walls (dash-dotted line) are used as reference layers.  $\phi$ , the parameter of the parameterized ellipse:  $x = a \cos \phi$  and  $z = b \sin \phi$ .

their longitudinal direction. This may only be true in the systolic phase of the cardiac cycle, when the stresses in the muscle fibers are large compared to the stresses in the collagen network. A description that includes the effect of the collagen network has been proposed by Ohayon and Chadwick [14], but when using this description one needs to assume a constitutive relation between stress and strain in the collagen network. In general this relation is unknown. Further, a realistic description of a muscle fiber path includes a transverse angle in addition to the helix angle  $\alpha$  [21]. The transverse angle is largest in the apical and the basal parts of the myocardium where the muscle fibers in the subendocardial layers continue in the subepicardium. In these regions, the assumption that the fiber layers coincide with the isobars is violated, and our stress estimates may be less accurate.

As mentioned in the introduction, Regen et al. [17] presented a procedure for estimating regional circumferential and meridional stresses. In their study, they also calculated the average of circumferential and meridional stresses. This was motivated by the fact that the average of circumferential and meridional stresses is independent of the fiber direction distribution across the wall [15]. Our fiber stress estimates equal twice the estimates calculated by Regen et al. [17] since the sum of orthogonal stresses always equals the sum of the principal stresses. Recently, DeAnda et al. [5] developed an explicit expression for average stress by combining Laplace's law with longitudinal force balance. However, their expression corresponds to Eq. 9, and is a thin shell approximation.

## 4.1 Applications

The regional stress equation can be used to assess the pattern of regional stress in normal, pressure overloaded or volume overloaded left ventricles. In the normal ventricle a characteristic pattern may be identified, while in overloaded ventricles the effect of hypertrophy can be studied. Further, the effects of abrupt changes in preload and afterload have been studied extensively in animal models by analyzing pressure-volume loops. Our regional stress equation might give additional information, since combined with strain measurements, regional mechanical work can be estimated.

The regional stress equation requires measurements of local wall thickness and principal curvatures. These parameters can be estimated from 3D MRI or ultrasound data by using the method of Regen et al. [17]. However, the equatorial and apical stress equations require only chamber dimensions; these dimensions may be measured directly in ultrasound 2D cine-loops or M-mode images. In invasive studies, the LV cavity pressure can be measured by using micro-manometer tipped catheters. However, in clinical research the LV cavity pressure must be estimated non-invasively. In patients without aortic stenosis, the aortic root pressure is approximately equal to the LV pressure throughout ejection. Estimates of aortic pressure curves, can then be obtained by calibrating carotid or subclavian applanation-tonometer curves [12], pulse curves [4] or diameter curves [10] with brachial arterial systolic and diastolic pressures.

## 5 Conclusion

We have developed equations for estimating regional fiber stress in rotationally symmetric chambers (Eq. 10) and equatorial and apical fiber stress in prolate spheroidal chambers (Eqs. 12 and 13). The equations have been validated against idealized prolate spheroidal chambers, whose wall thicknesses are such that the fiber stress is uniform from the equator to apex.

## 6 Acknowledgments

This study was supported by Program for Medical Technology at the Norwegian University of Science and Technology. We thank Nancy Lea Eik-Nes for revision of the paper.

## References

1. Arts T, Bovendeerd PHM, Prinzen FW, Reneman RS. Relation between left ventricular cavity pressure and volume and systolic fiber stress and strain in the wall. *Biophys J* 1991;59:93-102.
2. Chadwick RS. Mechanics of the left ventricle. *Biophys J* 1982;39:279-288.
3. Colan SD, Borow KM, Neumann A. Left ventricular end-systolic wall stress-velocity of fiber shortening relation: a load-independent index of myocardial contractility. *J Am Coll Cardiol* 1984;4:715-24.
4. Colan SD, Borow KM, Neumann A. Use of the calibrated carotid pulse tracing for calculation of left ventricular pressure and wall stress throughout ejection. *Am Heart J* 1985;109:1306-10.
5. DeAnda A, Komeda M, Moon MR, Green GR, Bolger AF, Nikolic SD, Daughters GT, Miller DC. Estimation of regional left ventricular wall stresses in intact canine hearts. *Am J Physiol* 1998;275:H1879-85.
6. Gaasch WH, Zile MR, Hoshino PK, Apstein CS, Blaustein AS. Stress-shortening relations and myocardial blood flow in compensated and failing canine hearts with pressure-overload hypertrophy. *Circulation* 1989;79:872-83.
7. Greenbaum RA, Ho SY, Gibson DG, Becker AE, Anderson RH. Left ventricular fibre architecture in man. *Br Heart J* 1981;45:248-63.
8. Grossman W, Jones D, McLaurin LP. Wall stress and patterns of hypertrophy in the human left ventricle. *J Clin Invest* 1975;56:56-64.

9. Hexeberg E, Matre K, Lekven J. Transmural fibre direction in the anterior wall of the feline left ventricle: theoretical considerations with regard to uniformity of contraction. *Acta Physiol Scand* 1991;141:497-505.
10. Hokanson DE, Mozersky DJ, Sumner DS, Strandness DE. A phase-locked echo tracking system for recording arterial diameter changes in vivo. *J Appl Physiol* 1972;32:728-33.
11. Huisman RM, Elzinga G, Westerhof N, Sipkema P. Measurement of left ventricular wall stress. *Cardiovasc Res* 1980;14:142-53.
12. Kelly RP, Hayward C, Ganis J, Daley J, Avolio AP, O'Rourke M. Noninvasive registration of the arterial pressure pulse waveform using high-fidelity applanation tonometry. *J Vasc Med Biol* 1989;1:142-9.
13. Lipschutz M. Theory and Problems of Differential Geometry. Schaum's outline series. New York: McGraw-Hill, Inc., 1969.
14. Ohayon J, Chadwick RS. Effects of collagen microstructure on the mechanics of the left ventricle. *Biophys J* 1988;54:1077-88.
15. Regen DM. Myocardial stress equations: fiberstresses of the prolate spheroid. *J Theor Biol* 1984;109:191-215.
16. Regen DM. Relations between hydrodynamic and mechanical properties of a sphere. *Ann Biomed Eng* 1988;16:573-88.
17. Regen DM, Anversa P, Capasso JM. Segmental calculation of left ventricular wall stresses. *Am J Physiol* 1993;264:H1411-21.
18. Ross MA, Streeter DD. Nonuniform subendocardial fiber orientation in the normal macaque left ventricle. *European Journal of Cardiology* 1975;3:229-47.
19. Skalak R. Approximate formulas for myocardial fiber stresses. *J Biomech Eng* 1982;104:162-163.
20. Strauer BE, Beer K, Heitlinger K, Hoffing B. Left ventricular systolic wall stress as a primary determinant of myocardial oxygen consumption: comparative studies in patients with normal left ventricular function, with pressure and volume overload and with coronary heart disease. *Basic Res Cardiol* 1977;72:306-13.
21. Streeter DD. Gross morphology and fiber geometry of the heart. In: Berne RM, Sperelakis N, Geiger S, eds., *Handbook of Physiology, Section 2: The Cardiovascular System*, Baltimore, Maryland: Waverly Press, Inc., vol. 1. The Heart. 1979; 61-112.
22. Streeter DD, Spotnitz HM, Patel DP, Ross J, Sonnenblick EH. Fiber orientation in the canine left ventricle during diastole and systole. *Circ Res* 1969;24:339-347.

23. Streeter DD, Vaishnav RN, Patel DP, Spotnitz HM, Ross J, Sonnenblick EH. Stress distribution in the canine left ventricle during diastole and systole. *Biophys J* 1970;10:345-63.
24. Timoshenko SP, Woinowsky-Krieger S. *Theory of Plates and Shells*. New York: McGraw-Hill, Inc., 1959.

# Paper B



# Semiautomatic contour detection in ultrasound M-mode images

Stein Inge Rabben<sup>1</sup>, Anders Herman Torp<sup>2</sup>, Asbjørn Støylen<sup>3</sup>,  
Stig Slørdahl<sup>3</sup>, Knut Bjørnstad<sup>3</sup>, Bjørn Olav Haugen<sup>3</sup>  
and Bjørn Angelsen<sup>1</sup>

<sup>1</sup>Department of Physiology and Biomedical Engineering, NTNU, Trondheim, Norway

<sup>2</sup>Department of Computer and Information Science, NTNU, Trondheim, Norway

<sup>3</sup>Department of Medicine, Section of Cardiology, University Hospital Trondheim, Norway

## Abstract

We have developed a method for semiautomatic contour detection in M-mode images. The method combines tissue Doppler and gray-scale data. It was used to detect: 1. the left endocardium of the septum, the endocardium and epicardium of the posterior wall in 16 left ventricular short-axis M-modes, and 2. the mitral ring in 38 anatomical M-modes extracted pair-wise in 19 apical four-chamber cine-loops (healthy subjects). We validated the results by comparing the computer-generated contours with contours manually outlined by four echocardiographers. For all boundaries, the average distance between the computer-generated contours and the manual outlines was smaller than the average distance between the manual outlines. We also calculated left ventricular wall thickness and diameter at end-diastole and end-systole and lateral and septal mitral ring excursions, and found, on average, clinically negligible differences between the computer-generated indices and the same indices based on manual outlines (0.8–1.8 mm). The results were also within published normal values. In conclusion, this initial study showed that it was feasible in a robust and efficient manner to detect continuous wall boundaries in M-mode images so that tracings of left ventricular wall thickness, diameter and long axis could be derived.

## 1 Introduction

Transverse M-mode was the original, and for many years the only, echocardiographic mode for evaluation of cardiac chambers and function [10, 23]. Today, two-dimensional (2D) echocardiography gives additional information, especially in analysis of regional dysfunction. However, in symmetric left ventricles, transverse M-mode still offers a quick and reliable way of assessing ventricular dilation, hypertrophy and contractility [11]. Longitudinal M-mode, on the other hand, is a rather new method, the clinical implication of which is still being investigated. Studies show that the systolic descent of the mitral plane toward the apex is related to global systolic function [1, 15, 20, 25] and prognosis [32], and the diastolic motion of the mitral ring is related to global diastolic function [5, 6]. Furthermore, the relation of transverse and longitudinal systolic shortening changes in various hypertrophic states [3, 31].

Manual drawing of contours in M-mode images is time-consuming and difficult. Hence, echocardiographers usually identify the wall boundaries only at end-systole and end-diastole. Subtraction of one wall boundary from another gives geometrical parameters, such as LV wall thickness, diameter and long axis as a function of time, so that peak and nadir values can easily be determined. The traces may also be differentiated to give rates of change, allowing peak and time-to-peak values to be determined.

Semiautomatic contour detection has the potential of simplifying the work of extracting continuous wall boundaries. Contour detection is often modeled as an energy minimization problem [2, 8, 13, 18]. All admissible candidate contours are associated with individual energy values. The energy function is constructed so that favorable properties decrease energy; i.e., image locations with high gray-scale values and high gradients are assigned low energy values. Most of the development of contour detection in echocardiography has been directed towards 2D images. Only a few attempts of contour detection in M-mode echocardiograms have been reported [19, 30]. Unser et al. [30] described a method based on template matching. The correlation between a reference template and the pixel values in the neighborhood of a candidate point gave a local energy value. The sum of all local energy values along a candidate contour defined a global energy, and the optimal contour was found by dynamic programming as the candidate contour that had the lowest global energy value. Unser et al. [30] reported satisfactory results, but their method was based only on gray-scale information. Recently, a technique that quantifies the velocity of the myocardium, Doppler tissue imaging (DTI), was introduced (Fig. 1) [21, 27]. A combined use of gray-scale and tissue Doppler data may make automatic contour detection in M-mode images more reliable.

The purpose of this study was to develop a semiautomatic contour-detection method that combined M-mode gray-scale and tissue Doppler data, and to make an *in vivo* assessment of this method. Our contour-detection method was based on minimization of a global energy function that included terms that represented image and contour shape properties. To validate the contour-detection method we compared automati-

cally detected contours with contours manually outlined by four echocardiographers in M-modes from 19 healthy subjects. Both LV short-axis M-modes and anatomical M-modes of the mitral ring were studied.

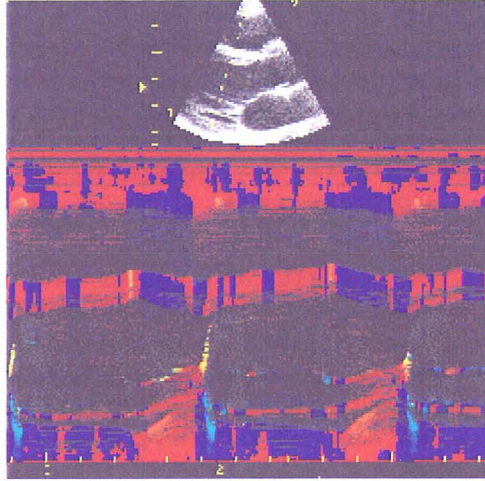


**Figure 1:** Example of a parasternal 2D-guided M-mode with simultaneous gray-scale and tissue Doppler recordings. Red denotes velocities towards the probe; blue denotes velocities away from the probe.

## 2 Method

### 2.1 Software system

We developed a software system for contour detection in ultrasound M-mode images. The system consists of: an application-dependent contour-detection module, a generic library for contour detection based on dynamic programming, and a module for loading of ultrasound image data. The application-dependent module, which provides the user interface, uses the generic library for contour detection together with its own supplementary algorithms to detect contours in the M-mode images. The software system was implemented in C++/MFC (Microsoft Foundation Classes) and runs under Windows95 and WindowsNT (Microsoft Corporation, Washington, USA).

### 2.2 Overview of the semiautomatic contour-detection method

The software system allows the operator to move the cursor to the boundary to be detected in the M-mode image (Fig. 2 upper panels). By integrating the velocity at

the cursor point, the system estimates the position of the point in the next time-step. To obtain an initial contour, this kind of point tracking is done for all time-steps in the M-mode image. Aliasing of Doppler estimates may occur in small regions of some DTI images. To detect aliasing, the system compares the velocity of two neighbor points on a contour. If the difference in the velocities between two neighbor contour points is larger than the Nyquist velocity, twice the Nyquist velocity is added to negative velocities or subtracted from positive velocities. However, the absolute value of the corrected velocities is not allowed to exceed twice the Nyquist velocity. In some of the initial contours, a small drifting is observed. If ECG data are present, this drifting can optionally be adjusted. The system then compares the depth of the initial contour at times corresponding to the R-peaks of the ECG, and adjusts for the drift of the contour if the contour is not cyclic.

When the operator is satisfied with the initial contour, he or she confirms by pushing the mouse button (Fig. 2 middle panels). The system then defines a candidate region (CR) in the M-mode image by selecting all the points in a given range around the initial contour. For each time-step, the CR now defines candidate vertices of the optimal contour. The system automatically runs the optimal contour-detection algorithm with operator-defined settings. The details of the optimal contour-detection algorithm are described in the section below.

If necessary, the operator may manually correct the contour by selecting points inside the CR. After each point selection, the optimal contour-detection algorithm finds a new contour forced through the operator-selected point (Fig. 2 lower panels).

### 2.3 Details of the optimal contour-detection algorithm

A general description of the theory of dynamic programming for optimal contour detection is presented by Amini et al. [2]. This section describes our implementation of this methodology for contour detection in M-mode images.

Fig. 3 illustrates an M-mode image with a candidate contour that consists of a sequence of line segments with  $n$  vertices  $(p_1, p_2, \dots, p_n)$ . For each M-line, a vertex  $p_t$  is selected from  $m$  candidate pixels, i.e.,  $p_t \in \{p_t^1, p_t^2, \dots, p_t^m\}$ . Each candidate contour is associated with an individual energy value, that is calculated according to contour shape (internal energy) and image properties at the locations of the contour vertices (external energy). The total energy function for a candidate contour is hence decomposed as follows:

$$E_{total}(p_n) = \sum_{t=1}^n E_{ext}(p_t) + \sum_{t=2}^n E_{int}(p_{t-1}, p_t) \quad (1)$$

where  $E_{ext}$  represents image properties and  $E_{int}$  represents contour shape. Typically, the image property term  $E_{ext}$  is constructed so that image locations with high gray-scale values and high spatial gradients are assigned low energy values, and the contour shape term  $E_{int}$  assures geometrical smoothness. The optimal contour is found as the

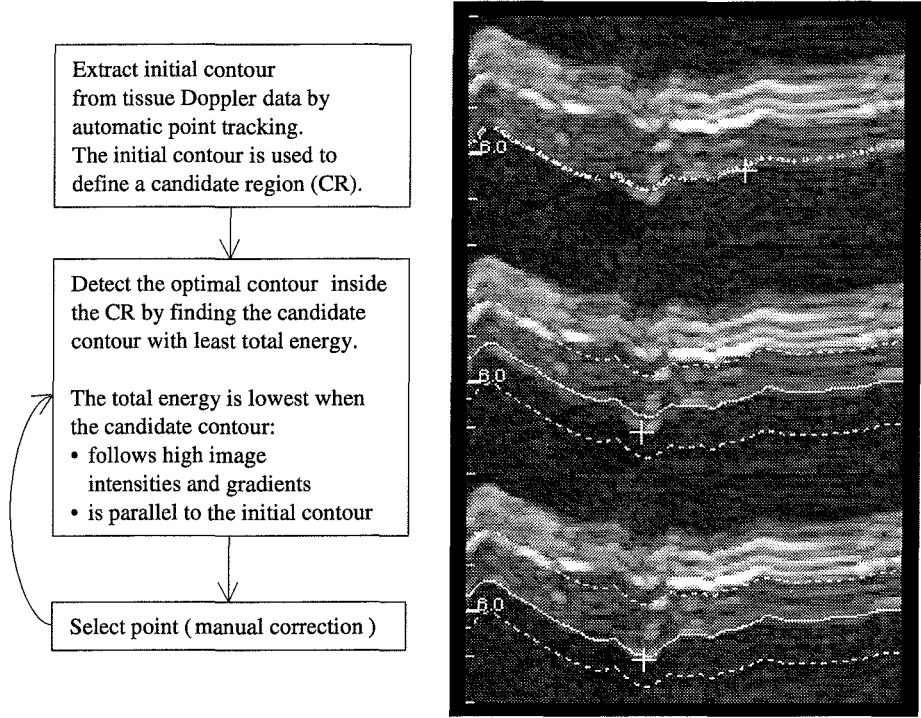


**Figure 2:** Left: the semiautomatic contour-detection method. Upper right: the operator moves the cursor (cross) to a boundary in the image. The cursor is the starting point for extraction of the initial contour (thick dotted line). Middle and lower right: the dotted lines indicate the candidate region, and the solid line is the detected optimal contour. The cross represents a point that the operator selects for manual correction. The optimal detected contour is forced through this point (lower right).

candidate contour with the smallest total energy. For effective global minimization, Eq. 1 can be translated into a dynamic programming algorithm, where the minimal total energy from  $p_1$  to  $p_t$  is found by iterating the following recurrence formula:

$$S_t(p_t) = \begin{cases} E_{ext}(p_t) & , \quad t = 1 \\ \min_{p_{t-1}} [S_{t-1}(p_{t-1}) + E_{ext}(p_t) + E_{int}(p_{t-1}, p_t)] & , \quad 1 < t \leq n \end{cases} \quad (2)$$

At time  $t$ , the optimal value function  $S_t$  contains a value for each candidate pixel  $\{p_t^1, p_t^2, \dots, p_t^m\}$ . Eq. 2 is based on the principle of optimality [4], which may be stated as follows: if the optimal contour goes through a given pixel  $p_t^k$ , then the optimal contour includes, as a part of it, the optimal partial contour to pixel  $p_t^k$ . Accordingly, it is sufficient to restrict the search at time  $t$  to sub-contours that are optimal from



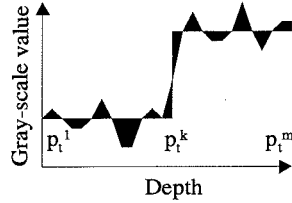


**Figure 4:** An illustration of the energy term  $E_{trans}$  (Eq. 6). The sum of the filled areas corresponds to the value of the energy term. The filled areas are determined by the difference between the horizontal lines and the gray-scale value of the pixels at different depths. The horizontal lines represent the average gray-scale value of the pixels on each side of the candidate pixel  $p_t^k$  and correspond to the first term inside each absolute value functions of  $E_{trans}$ . For another candidate pixel (move the vertical line), the sum of the filled areas, and thereby the energy, will be higher.

seen experimentally that the initial contour is a good *a priori* approximation of the shape of the wall boundary as long as the M-line is approximately perpendicular to the wall boundary.  $E_{int}$  is thus calculated from the initial and candidate contours as follows:

$$E_{int}(p_{t-1}, p_t) = |[D(i_t) - D(i_{t-1})] - [D(p_t) - D(p_{t-1})]| \quad (7)$$

where  $i_t$  is the vertex of the initial contour at time  $t$ , and  $D(\cdot)$  represents the distance from the ultrasound probe to a given contour vertex (depth). The initial contour is extracted, as described above, from tissue Doppler data. Our contour-detection algorithm is hence based on both gray-scale and tissue Doppler data (Eqs. 4–7).

All energy terms listed in Eqs. 4–7 are given individual weights. When recording M-mode images of the heart, we often see that the different walls of the heart have different image characteristics. It is hence important to define individual weights for different wall boundaries. Default weights for each wall boundary were found empirically.

Manual correction of a detected contour is implemented by reducing the number of candidate pixels in the specific M-line to include only the operator-selected pixel.

The complexity of the optimal contour-detection algorithm is  $O(nm^2)$ . However, if we define a maximum allowable boundary velocity and thereby a maximum allowable displacement from  $p_{t-1}$  to  $p_t$ , the  $\min(\cdot)$  operator in Eq. 2 can be reduced to search only a small number of candidate pixels. The number of allowable candidate pixels may then be considered constant and the overall complexity is reduced to  $O(nm)$ .

## 2.4 Acquisition of data

A System FiVe scanner (GE Vingmed Ultrasound, Horten, Norway) with a 2.5 MHz FPA probe was used to record data in 19 healthy subjects (age  $30 \pm 5$  years). All sub-

jects gave informed consent. Standard parasternal 2D-guided M-modes at the equatorial level and apical four-chamber cine-loops were recorded with the subjects in the left lateral recumbent position. Simultaneous gray-scale and Doppler tissue imaging were performed (Fig. 1). If necessary, second harmonic (octave) mode was used to obtain better image quality. To utilize the dynamic range of the color-flow system and to avoid excessive aliasing, the echocardiographer optimized the pulse repetition frequency (PRF). In the short-axis M-modes, the echocardiographer identified aliasing by looking at the velocities (colors) of the endocardium of the posterior wall and, in the four-chamber cine-loops, the echocardiographer identified aliasing by looking at the velocities of the mitral ring.

After the examination, the raw digital ultrasound data with separate gray-scale and DTI values were transferred to a PC for analysis. The DTI samples were represented as auto-correlation function values [17, 28]. Each data set consisted of two to four cardiac cycles. The M-modes had a temporal resolution of 4–6 ms, and the 2D cine-loops had  $101 \pm 24$  frames per second.

## 2.5 Analysis

### 2.5.1 Comparison with manual drawing

Because medical image segmentation lacks gold standards, we compared the automatically detected contours with contours drawn by echocardiographers [7]. Four echocardiographers manually outlined the LV septal endocardium, and the endocardium and epicardium of the posterior wall in one cardiac cycle of each short-axis M-mode. The drawing of boundaries was done as described in the recommendations of the American Society of Echocardiography [23]. Any questions regarding the identifiability of a wall boundary in a poor-quality image, and any mismatch of more than 15 degrees between the M-line and LV short axis, excluded the quantification of that image. We excluded three of the 19 short-axis M-modes on these criteria. In the apical four-chamber cine-loops, we defined two anatomical M-lines, one from the apex to the lateral part of the mitral ring, another from the apex to the septal part of the mitral ring (Fig. 5). The four echocardiographers manually outlined one cardiac cycle of the mitral ring in each of the anatomical M-modes. We then used the semiautomatic method to detect the same boundaries. The manually outlined contours were compared to the automatically detected contours by calculating the mean distance between the computer-generated contours and the manually outlined contours (computer-to-observer distance = COD), and the mean distance between the contours outlined by the observers (interobserver distance = IOD). The distance between two contours was defined as the average difference in depth between pairs of points on the two contours, i.e., we used the following distance measure:

$$d(\mathbf{a}, \mathbf{b}) = \frac{1}{n} \sum_{i=1}^n |D(a_i) - D(b_i)| \quad (8)$$

where  $\mathbf{a}$  and  $\mathbf{b}$  are the contour vertices, and  $D(\cdot)$  represents the distance from the probe to a given vertex (depth).

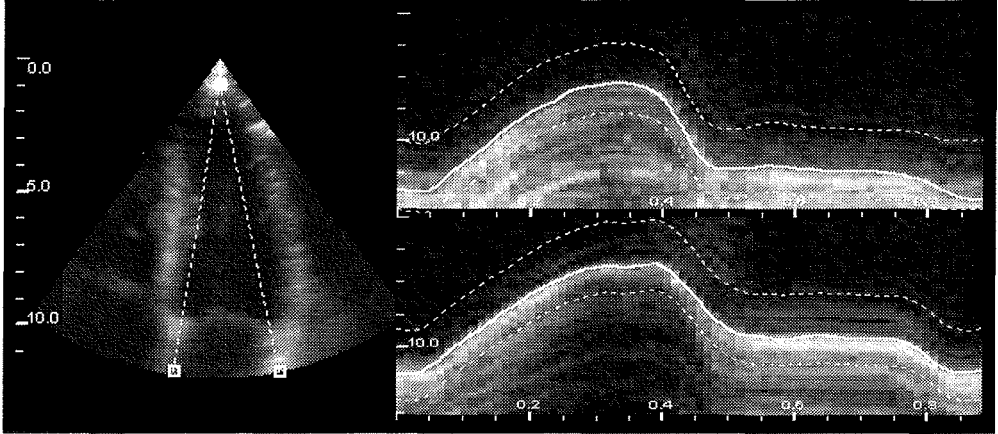


**Figure 5:** Left: an apical four-chamber cine-loop. The dotted lines indicate two anatomical M-lines: one from the apex to the lateral mitral ring, another from the apex to the septal mitral ring. Right upper panel: lateral part of the mitral ring. Right lower panel: septal part of the mitral ring.

Tracings of LV diameter (LVD) were obtained by subtracting the LV septum from the endocardium of the posterior wall, and tracings of the posterior wall thickness (PWT) were obtained by subtracting the endocardium from the epicardium of the posterior wall. The following parameters were calculated:

1. End-diastolic wall thickness (PWTd) and diameter (LVDd), defined as the PWT and LVD at the time corresponding to the R-peak of the ECG.
2. End-systolic wall thickness (PWTs) and diameter (LVDs), defined as the maximum PWT and the minimum LVD, respectively.
3. Fractional shortening (FS), defined as  $FS = 100 * (LVDd - LVDs) / LVDd$ .
4. Lateral and septal mitral ring excursion (LMRE and SMRE), defined as the amplitude of the lateral and septal mitral ring contours, respectively.

The COD and IOD were also calculated for these parameters. Because the operator of the detection method was allowed to force the detected contour through specific points, we also registered the number of manual corrections needed per contour.

### 2.5.2 Signal-averaged tracings

Our semiautomatic method was used to detect the mitral ring in several cardiac cycles of the anatomical M-modes. The mitral ring motion was then differentiated to give velocities. Because differentiation is a noise-sensitive operation, we averaged two to four cardiac cycles before differentiation. The following parameters were computed from the differentiated waveforms: peak velocities of the lateral and septal mitral ring during the systolic, early filling and atrial contraction phases (LMRVs, SMRVs, LMRVe, SMRVe, LMRVa and SMRVa, respectively).

## 3 Results

### 3.1 Comparison with manual drawings

Table 1 shows the computer-to-observer distance (COD) and the interobserver distance (IOD) calculated for the different boundaries. For all boundaries, the COD was smaller than the IOD. This was especially noticeable for the LV septum, the epicardium of the posterior wall, and the lateral and septal mitral ring. For the endocardium of the posterior wall, the COD was only slightly smaller than the IOD.

Boundary	COD (mm)	IOD (mm)
Septum	$0.83 \pm 0.35$	$0.98 \pm 0.39$
Endocardium	$1.07 \pm 0.20$	$1.09 \pm 0.25$
Epicardium	$0.84 \pm 0.14$	$1.00 \pm 0.25$
Septal part of mitral ring	$0.85 \pm 0.14$	$1.02 \pm 0.20$
Lateral part of mitral ring	$0.94 \pm 0.13$	$1.08 \pm 0.23$

**Table 1:** Comparison between the automatically detected contours and the contours manually outlined by the four echocardiographers (mean  $\pm$  standard deviation). COD = computer-to-observer distance. IOD = interobserver distance.

The LV diameters at end-diastole (LVDd) were, on average, 2% smaller when based on computer-generated contours than when based on manually outlined contours, and the LV diameters at end-systole (LVDs) were, on average, 3% larger when based on computer-generated contours than when based on manually outlined contours (Tables 2 and 3). Correspondingly, the fractional shortening (FS) based on the computer-generated contours was, on average, lower than the FS based on the manually outlined contours (Table 3). The underestimation of LVDd and overestimation of LVDs were also reflected in the measurements of posterior wall thickness (PWT). The PWTs based on the computer-generated contours was, on average, 5% smaller than the PWTs based on the manually outlined contours, and the PWTd based on the computer-generated contours was, on average, 10% larger than the PWTd based on the manually outlined

contours (Tables 2 and 3).

Parameter	COD (mm)	IOD (mm)
LVDd	$1.54 \pm 0.54$	$1.32 \pm 0.38$
LVDs	$1.99 \pm 0.26$	$1.78 \pm 0.67$
PWTd	$1.28 \pm 0.40$	$1.21 \pm 0.26$
PWTs	$1.55 \pm 0.48$	$1.52 \pm 0.23$
LMRE	$1.85 \pm 0.35$	$1.10 \pm 0.23$
SMRE	$1.04 \pm 0.10$	$0.73 \pm 0.13$

**Table 2:** Comparison of clinical parameters extracted from computer-generated contours and contours manually outlined by four echocardiographers (mean  $\pm$  standard deviation). LVDd and LVDs = end-diastolic and end-systolic LV diameter. PWTd and PWTs = end-diastolic and end-systolic posterior wall thickness. LMRE and SMRE = lateral and septal mitral ring excursion.

Parameter	C	O1	O2	O3	O4	Mean Obs
LVDd (mm)	$51.6 \pm 4.5$	$51.8 \pm 4.3$	$52.9 \pm 4.3$	$52.5 \pm 4.3$	$53.8 \pm 4.2$	$52.7 \pm 4.2$
LVDs (mm)	$34.9 \pm 3.1$	$32.8 \pm 3.0$	$33.9 \pm 3.1$	$33.3 \pm 2.4$	$35.6 \pm 2.7$	$33.9 \pm 3.0$
PWTd (mm)	$8.8 \pm 1.9$	$8.2 \pm 1.8$	$7.5 \pm 1.3$	$8.2 \pm 1.9$	$8.2 \pm 1.3$	$8.0 \pm 1.6$
PWTs (mm)	$14.3 \pm 2.1$	$14.4 \pm 2.5$	$15.0 \pm 3.3$	$15.0 \pm 2.1$	$16.0 \pm 2.9$	$15.1 \pm 2.7$
FS (%)	$32.2 \pm 4.8$	$36.6 \pm 4.8$	$35.6 \pm 5.6$	$36.4 \pm 4.9$	$33.7 \pm 4.2$	$35.6 \pm 4.9$
LMRE (mm)	$16.2 \pm 2.0$	$18.4 \pm 2.9$	$17.8 \pm 1.9$	$17.7 \pm 2.0$	$17.9 \pm 2.3$	$18.0 \pm 2.2$
SMRE (mm)	$16.0 \pm 1.9$	$16.7 \pm 2.0$	$16.7 \pm 2.2$	$16.5 \pm 2.5$	$16.8 \pm 2.0$	$16.7 \pm 2.1$

**Table 3:** Mean and standard deviation of clinical parameters extracted from computer-generated contours and contours outlined manually by the observers. The last column gives the mean of all the observers. FS = fractional shortening.

For the lateral and septal mitral ring excursions (LMRE and SMRE), the COD was larger than the IOD (Table 2). This difference was also reflected by the fact that the LMRE and SMRE based on the computer-generated contours were, on average, 10% and 4% smaller than the LMRE and SMRE based on the manual outlines (Table 3).

The total number of manual corrections was six for the LV septum and one for the endocardium of the posterior wall. For the other boundaries, we did not do any manual corrections. For the LV septal boundary, we also increased the height of the candidate region from 8 mm to 14 mm in two images.

### 3.2 Signal-averaged tracings

During systole, the peak velocities of the lateral mitral ring were on average higher than the peak velocities of the septal mitral ring. This was also the case for the early filling phase, but, during the atrial contraction phase, the peak velocities of the septal

mitral ring were, on average, highest (Table 4). This pattern is illustrated in Fig. 6, which shows the mitral ring velocities in a healthy subject.

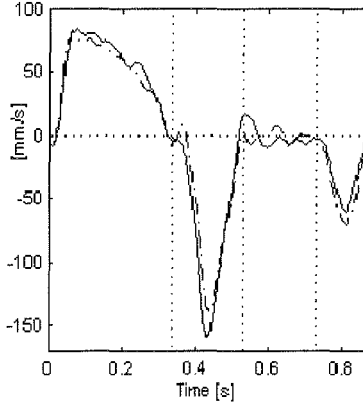


**Figure 6:** Mitral ring velocities in a healthy subject. The solid line denotes the velocities of the lateral mitral ring (LMRV), while the dash-dotted line denotes the velocities of the septal mitral ring (SMRV).

Parameter	mean	$\pm$
LMRVs (mm/s)	80	14
SMRVs (mm/s)	68	10
LMRVe (mm/s)	-123	29
SMRVe (mm/s)	-98	19
LMRVa (mm/s)	-49	16
SMRVa (mm/s)	-62	13

**Table 4:** Mean and standard deviation of parameters extracted from signal-averaged waveforms. LMRV and SMRV = peak lateral and septal mitral ring velocity, respectively; s, e and a = systole, early filling and atrial contraction phases, respectively.

## 4 Discussion

We have developed a robust and efficient method for obtaining wall boundaries in M-mode images. The method, which is based on dynamic programming, efficiently detects the global optimal contour. On a 266 MHz Pentium II, it takes 2–3 seconds to detect the contour in three to four cardiac cycles (candidate region height of 1 cm).

We validated the method by comparing computer-generated contours with contours manually outlined by four echocardiographers. The results are promising (Tables 1 and 2). For all boundaries, the computer-generated contours were, on average, within the range of the manually outlined contours. We also calculated clinical parameters from the computer-generated contours and the manual outlines. On average, we observed clinical negligible differences (Table 3), and the computer-generated parameters were also in accordance with published normal values [9, 11, 26, 31].

Image segmentation consists of two qualitatively different tasks: object recognition and object delineation. Recognition of objects in echocardiograms requires expert knowledge and is done most reliably by echocardiographers. However, a computer might do systematic object delineation more reliably than echocardiographers. Our method combines the strengths of the echocardiographer and the computer. The echocardiographer first recognizes the wall boundary; the computer algorithm then detects an optimal contour according to empirically defined settings (Fig. 2).

Figs. 2 and 7 illustrate different situations when detecting contours in M-mode images. In Fig. 2, we see a good-quality LV septal boundary. The initial contour is reliably extracted and the method performs well. Fig. 7A shows an LV septal boundary with gray-scale dropouts during systole. The contour-detection method tolerates dropouts because it depends on an initial contour that is extracted from Doppler information. Generally, Doppler imaging has better penetration than gray-scale imaging because pulse lengths are longer. The high-pass filter used on Doppler imaging also removes stationary reverberations seen in the gray-scale data. Further, Doppler processing is based on measuring the phase shift of ultrasound pulses that have been reflected by moving scatters, and this phase shift can be detected even in very weak signals. In Fig. 7B, we see mobile structures, such as chordae tendineae, against the endocardium of the posterior wall. In this case, the method performs well because the dynamic programming algorithm assures global optimality and thereby favors continuous speckle lines. In Fig. 7C, the M-line was not perpendicular to the LV septal wall during the recording. The septum has a substantial lateral motion, because the base of the heart moves towards apex during systole and back again during diastole; this affected the calculation of the initial contour (middle panel of Fig. 7C). This lateral wall-motion effect is illustrated in Fig. 8, where the wall has a motion to the right, and there is an oblique angle between the M-line and the wall. The tissue-blood transition (at the M-line) will then have a downward motion, even though the wall's radial velocity is zero. Under such conditions, the initial contour will underestimate the boundary excursion seen in the M-mode image because the initial contour is entirely based on the radial velocity of the wall. This underestimation may, again, affect the final contour because the initial contour is used as an *a priori* approximation of the contour shape (Eq. 7). In the lower panel of Fig. 7C, we have hence made a single manual correction of the contour. Fig. 7D shows a poor-quality image of the endocardium of the posterior wall. In this particular case, abnormal strong echoes from the valve leaflets affect the Doppler estimates and the extracted initial and thereby the final contours are of questionable quality.

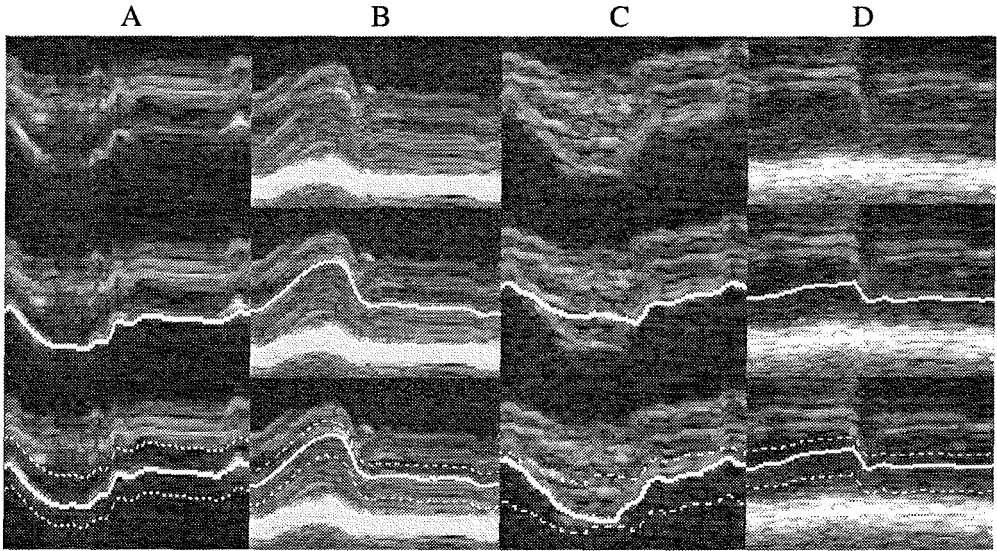


**Figure 7:** Examples of four different wall boundaries. Middle panels: initial contours. Lower panels: final contours. A: an LV septal boundary with dropouts in the gray-scale data. B: mobile structures against the endocardium of the posterior wall. C: an LV septal boundary where the ultrasound beam was oblique to the wall during the recording. The initial contour underestimates the boundary excursion due to lateral wall motion (see text for explanation). However, a single manual correction gave a reasonable final contour (lower panel). D: the endocardium of the posterior wall in a poor-quality image. The strong echoes from the valve leaflets affect the Doppler estimates at the boundary, and the initial and final contours are of questionable quality.

Different wall boundaries in an M-mode echocardiogram have different characteristics, e.g., the LV septal endocardium usually has a clear tissue-blood transition while mobile structures, such as chordae tendineae and valve leaflets, often appear against the endocardium of the posterior wall (Fig. 7B). This makes it necessary to give each wall boundary individual energy weights. In this study, we optimized the weights empirically. The image quality in different subjects varies enormously. In good-quality images, high weight may be given to the gray-scale data, while, in poor-quality images, high weight may be given to the contour shape. It may therefore be a good idea to define two sets of weights per wall boundary, one for good-quality images and another for poor-quality images.

With our method, the echocardiographer has the possibility to make manual corrections. Fig. 2 illustrates that a single manual correction may affect a substantial part of the contour. In the middle image, the echocardiographer selects a point inside the

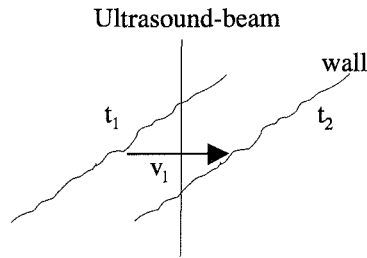


**Figure 8:** An M-line intersects a wall that moves with velocity  $v_1$  to the right. The position of the wall is shown at time  $t_1$  and  $t_2$ . If there is an oblique angle between the M-line and the wall, the tissue-blood transition (at the M-line) will have a downward motion in the interval  $t_1$  to  $t_2$ .

candidate region and the optimal contour-detection algorithm is re-run. In the lower image, the new contour is displayed. It has been lowered in whole systole.

In some of the initial contours, a small drifting was observed. As long as the wall boundary was inside the candidate region, this drifting of the initial contour usually did not influence the detection of the optimal contour. The calculation of the total energy of a candidate contour was partly based on comparing depth increments of the initial contour with depth increments of the candidate contour (Eq. 7). Because the errors in the depth increments of the initial contour were very small and additional energy terms (Eqs. 4–6) were used in the total energy function, drifting was seldom seen in the detected optimal contour.

Our *in vivo* validation showed that, for all the boundaries, the semiautomatic contour-detection method agreed well with the echocardiographers' manual outlines (Table 1). We believe that the COD was smaller than the IOD because of the inherent inaccuracy of manual outlining. The endocardium of the posterior wall was the most difficult contour to extract semiautomatically (Table 1). The probable reason was intermittent appearance of mobile structures, such as papillary muscles, chordae tendineae, trabeculae and valve leaflets, against the endocardium (Fig. 7B).

When comparing clinical parameters based on computer-generated contours with clinical parameters based on manually outlined contours, we observed differences (Table 3). These differences illustrate the fact that the excursions of the computer-generated contours were, on average, smaller than the excursions of the manual outlines. After the analysis, we observed that, in two of the short-axis M-modes, the manual outlines of the endocardium during systole included mobile structures such as chordae tendineae or papillary muscles, while the automatic method excluded these structures. This indicated that, in some situations, the automatic method was more reliable than manual outlining done by the observers. However, the differences could only be partially attributed to erroneous identification of the endocardium in these two images. In most M-modes, the M-line is not perfectly perpendicular to the wall

boundary and the lateral wall-motion effect described above (Fig. 7C) might also play a role.

Our study showed that there were differences in the peak velocities of the different parts of the mitral ring. The fact that the lateral part of the mitral ring has higher velocities than the septal part of the mitral ring during early filling is in accordance with results from other investigators [14, 16]. However, the absolute values were different. This is understandable, because their results were obtained with other techniques and because their controls were from other age groups. The averaging of several cardiac cycles to obtain a representative cycle may affect our results. The times of the peak velocities of the mitral ring will not exactly match from cycle to cycle. The peak velocities in the average cycle will therefore be lower than the peak velocities in the individual cycles.

#### **4.1 Limitations**

We analyzed only data obtained from healthy subjects. The quality of the images was probably higher than in the average patient. Hence, this study should only be seen as evidence for the feasibility of semiautomatic contour detection in M-modes from healthy subjects. We believe that the approach will be useful on data from patients, but further work on such data should be undertaken. One important aspect of a semiautomatic contour-detection method is the intraobserver variation. No intraobserver analysis was performed in this study. Our contour-detection method requires one operator-dependent decision: selection of initial point. In addition, it might require algorithmic optimization and manual corrections of the detected contour. These operator-dependent decisions may influence the intraobserver variation. In this study, we did only seven manual corrections on the 86 boundaries and we only increased the height of the candidate region from 8 mm to 14 mm in two of the LV septal boundaries.

#### **4.2 Clinical applications**

Stress echocardiography has become an emerging tool for diagnosing myocardial viability and/or reversible myocardial ischemia [22, 24]. Stress echo is based on visual analysis of regional wall motion and wall thickening, with comparison of rest and stress images. Our method may provide data concerning exact timing and magnitude of wall thickening, and may thus contribute to more objective and quantitative test analysis. Subtle wall-motion abnormalities and delayed contraction (tardokinesis) may be evidence of evolving myocardial ischemia, and such signs are usually difficult to assess by visual analysis only. Myocardial velocity gradients, which have been used to assess myocardial contractility [12, 29], may also be estimated from wall-thickness measurements performed by our method. Other applications would include measurements of amplitude, velocity and timing of the different portions of the mitral ring which have been used to evaluate ventricular systolic and diastolic function [1, 5, 6, 15, 20, 25]. Our method efficiently measures this information, and is therefore an addition to currently

used methods for assessing the ventricular long axis function.

## 5 Conclusion

This initial study showed that it was feasible to detect in a robust and efficient manner continuous wall boundaries in M-mode images so that tracings of left ventricular wall thickness, diameter and long axis could be derived.

## 6 Acknowledgments

This study was supported financially by Program for Medical Technology at the Norwegian University of Science and Technology, Trondheim, Norway. We thank Erik Østlyngen and Ragnar Wisløff for developing parts of the contour-detection software, and Nancy Lea Eik-Nes for revision of the paper.

## References

1. Alam M, Hoglund C, Thorstrand C. Longitudinal systolic shortening of the left ventricle: an echocardiographic study in subjects with and without preserved global function. *Clin Physiol* 1992;12:443–52.
2. Amini AA, Weymouth TE, Jain RC. Using dynamic programming for solving variational problems in vision. *IEEE Trans PAMI* 1990;12:855–867.
3. Aurigemma GP, Silver KH, Priest MA, Gaasch WH. Geometric changes allow normal ejection fraction despite depressed myocardial shortening in hypertensive left ventricular hypertrophy. *J Am Coll Cardiol* 1995;26:195–202.
4. Bellman R. *Dynamic programming*. Princeton, N.J.: Princeton University Press, 1957.
5. Blomstrand P, Kongstad O, Broqvist M, Dahlstrom U, Wranne B. Assessment of left ventricular diastolic function from mitral annulus motion, a comparison with pulsed Doppler measurements in patients with heart failure. *Clin Physiol* 1996; 16:483–93.
6. Bojo L, Wandt B, Ahlin NG. Reduced left ventricular relaxation velocity after acute myocardial infarction. *Clin Physiol* 1998;18:195–201.
7. Chalana V, Kim Y. A methodology for evaluation of boundary detection algorithms on medical images. *IEEE Trans Med Im* 1997;16:642–652.
8. Cohen LD, Cohen I. Finite-element methods for active contour models and balloons for 2-D and 3-D images. *IEEE Trans PAMI* 1993;15:1131–1147.

9. Devereux RB. Echocardiography: state of the art-1984. *Cardiology* 1984;71:118-35.
10. Devereux RB, Reichek N. Echocardiographic determination of left ventricular mass in man. Anatomic validation of the method. *Circulation* 1977;55:613-8.
11. Feigenbaum H. Echocardiography. Philadelphia: Lea and Febiger, 5th ed., 1994.
12. Fleming AD, Xia X, McDicken WN, Sutherland GR, Fenn L. Myocardial velocity gradients detected by Doppler imaging. *Br J Radiol* 1994;67:679-88.
13. Friedland N, Adam D. Automatic ventricular cavity boundary detection from sequential ultrasound images using simulated annealing. *IEEE Trans Med Im* 1989;8:344-53.
14. Isaza K, Munoz del Romeral L, Lee E, Schiller NB. Quantitation of the motion of the cardiac base in normal subjects by Doppler echocardiography. *J Am Soc Echocardiogr* 1993;6:166-76.
15. Jones CJ, Raposo L, Gibson DG. Functional importance of the long axis dynamics of the human left ventricle. *Br Heart J* 1990;63:215-20.
16. Karwatowski SP, Mohiaddin R, Yang GZ, Firmin DN, Sutton MS, Underwood SR, Longmore DB. Assessment of regional left ventricular long-axis motion with MR velocity mapping in healthy subjects. *J Magn Reson Imaging* 1994;4:151-5.
17. Kasai C, Namekawa K, Koyano A, Omoto R. Real-time two-dimensional blood flow imaging using an autocorrelation technique. *IEEE Trans Sonics Ultrason* 1985;SU-32:458-463.
18. Kass M, Witkin A, Terzopoulos D. Snakes: active contour models. *Int J Comput Vision* 1988;1:321-31.
19. Logan Sinclair RB, Oldershaw PJ, Gibson DB. Computing in echocardiography. *Prog Cardiovasc Dis* 1983;15:465-486.
20. Lundback S. Cardiac pumping and function of the ventricular septum. *Acta Physiol Scand Suppl* 1986;550:1-101.
21. Palka P, Lange A, Fleming AD, Sutherland GR, Fenn LN, McDicken WN. Doppler tissue imaging: myocardial wall motion velocities in normal subjects. *J Am Soc Echocardiogr* 1995;8:659-68.
22. Pierard LA, Landsheere CM, Berthe C, Rigo P, Kulbertus HE. Identification of viable myocardium by echocardiography during dobutamine infusion in patients with myocardial infarction after thrombolytic therapy: comparison with positron emission tomography. *J Am Coll Cardiol* 1990;15:1021-31.

23. Sahn DJ, DeMaria A, Kisslo J, Weyman A. Recommendations regarding quantitation in M-mode echocardiography: results of a survey of echocardiographic measurements. *Circulation* 1978;58:1072-83.
24. Sawada SG, Segar DS, Ryan T, Brown SE, Dohan AM, Williams R, Fineberg NS, Armstrong WF, Feigenbaum H. Echocardiographic detection of coronary artery disease during dobutamine infusion. *Circulation* 1991;83:1605-14.
25. Simonson JS, Schiller NB. Descent of the base of the left ventricle: an echocardiographic index of left ventricular function. *J Am Soc Echocardiogr* 1989;2:25-35.
26. St. John Sutton M, Reichek N, Kastor JA, Giuliani ER. Computerized M-mode echocardiographic analysis of left ventricular dysfunction in cardiac amyloid. *Circulation* 1982;66:790-9.
27. Sutherland GR, Stewart MJ, Groundstroem KW, Moran CM, Fleming AD, Guell-Peris FJ, et al. Color Doppler myocardial imaging: a new technique for the assessment of myocardial function. *J Am Soc Echocardiogr* 1994;7:441-58.
28. Torp H, Kristoffersen K, Angelsen BAJ. Autocorrelation techniques in color flow imaging: Signal model and statistical properties of autocorrelation estimates. *IEEE Trans UFFC* 1994;41:604-12.
29. Uematsu M, Miyatake K, Tanaka N, Matsuda H, Sano A, Yamazaki N, Hiramama M, Yamagishi M. Myocardial velocity gradient as a new indicator of regional left ventricular contraction: detection by a two-dimensional tissue doppler imaging technique. *J Am Coll Cardiol* 1995;26:217-23.
30. Unser M, Pelle G, Brun P, Eden M. Automated extraction of serial myocardial borders from M-mode echocardiograms. *IEEE Trans Med Im* 1989;8:96-103.
31. Wandt B, Bojo L, Hatle L, Wranne B. Left ventricular contraction pattern changes with age in normal adults. *J Am Soc Echocardiogr* 1998;11:857-63.
32. Willenheimer R, Cline C, Erhardt L, Israelsson B. Left ventricular atrioventricular plane displacement: an echocardiographic technique for rapid assessment of prognosis in heart failure. *Heart* 1997;78:230-6.



# Paper C



# Ultrasound-based vessel wall tracking: an auto-correlation technique with RF center frequency estimation

Stein Inge Rabben, Steinar Bjærum, Vidar Sørhus and Hans Torp

Department of Physiology and Biomedical Engineering, NTNU, Trondheim, Norway

## Abstract

The vessel diameter is related to the distending blood pressure, and is used in estimations of vessel stiffness parameters. Therefore, we wanted to develop an ultrasound-based method for tracking vessel walls. The tracking algorithm was based on auto-correlation with RF center frequency estimation. As opposed to the conventional auto-correlation method that only estimates the mean Doppler frequency, this method estimates both the mean Doppler frequency and the RF center frequency. Vessel tracking in ultrasound recordings of the carotid artery in four different subjects showed that the modified auto-correlation method performed better than the conventional auto-correlation method. To make a systematic evaluation of the estimators, we performed computer simulations of vessel wall-motion, where parameters such as pulse bandwidth, signal-to-noise ratio, packet size and sample volume were varied. In addition to the modified and the conventional auto-correlation methods, we analyzed two cross-correlation methods. Under the specific simulation conditions considered here, the modified auto-correlation method had the lowest bias of all methods, and a variance in the same range as the cross-correlation methods. Compared to the cross-correlation methods, the modified auto-correlation method has lower complexity in terms of number of computations and sampling rate requirements, and is therefore the preferred choice of method.

Submitted for publication

## 1 Introduction

Non-invasive estimation of arterial wall properties such as distensibility, compliance and pulse wave velocity has become increasingly important. Distensibility and compliance can be estimated by combining arterial pressure with vessel diameter measurements [10, 12, 21, 24], whereas pulse wave velocity can be measured by estimating the time-delay between diameter waveforms recorded simultaneously at two different positions along the vessel [3, 22] or by processing the temporal and longitudinal gradients of the change in diameter [5]. To study heart-vessel interactions, Parker et al. [20] introduced the wave intensity analysis that reveals the effects of incident and reflected waves on the pressure and velocity waveforms. Wave intensity analysis can be performed non-invasively by combining vessel diameter measurements with Doppler measurements of blood velocity [23]. Further, to estimate aortic pressure waveforms, investigators [1, 6] have calibrated volume-distension (diameter) waveforms recorded at the carotid or the subclavian artery with systolic and diastolic brachial artery pressures. Hence, we wanted to develop an ultrasound-based method for tracking of vessel walls.

Arndt et al. [2] reported use of a device that tracked the ultrasound echoes from the arterial wall by a threshold detector. The main weakness of this technique is that, because of damping, the amplitude of the echoes depends on the distance from the probe to the arterial wall; this distance varies during the cardiac cycle.

Later, Hokanson et al. [14] presented a phase-locking device that tracked a particular zero crossing within the radio-frequency (RF) signals (vessel wall echoes). This technique improved the radial resolution, down to a few microns. The phase-locking technique has later been improved by developing digital tracking hardware [9], linking the tracking system to B-mode imaging [15, 22] and combining the tracking system with pressure recordings [24].

As an alternative to the phase-locking technique, Hoeks and coworkers developed a displacement detection system based on conventional auto-correlation. In this system, the average phase over a fixed [13] or a moving [12] sample window was used to calculate the displacement. More recently, they replaced auto-correlation with RF cross-correlation [7, 11], because tracking based on RF cross-correlation, as opposed to conventional auto-correlation, is independent of the actual center frequency of the RF signal. The RF center frequency is modified by depth-dependent attenuation, especially for wide bandwidth signals (short pulses). RF cross-correlation will hence give more reliable tracking than conventional auto-correlation [11]. However, the conventional auto-correlation technique can be modified to estimate both the mean Doppler frequency and the RF center frequency inside the observation window (modified auto-correlation method) [17, 18, 25]. Compared to cross-correlation methods, the modified auto-correlation method has lower complexity in terms of the number of computations and sampling-rate requirements.

Hence, the purpose of this work has been (1) to develop a method for vessel-wall tracking based on the modified auto-correlation method and (2) to compare the modified auto-correlation method with displacement estimators based on the cross-

correlation method and the conventional auto-correlation method.

The first part of the paper presents a displacement estimator based on the modified auto-correlation method. Then an overview of the tracking system is given. To illustrate the performance of the conventional and modified auto-correlation methods, the tracking system was used on ultrasound recordings of the common carotid artery of four subjects. To make a more systematic comparison of the different displacement estimators, computer simulations that imitated a moving vessel wall were performed. From simulations, the bias and variance of the modified auto-correlation method [17, 18, 25], the conventional auto-correlation method [16] and two alternative cross-correlation methods [7, 19] were estimated.

## 2 Materials and methods

### 2.1 The modified auto-correlation method

An RF signal received after pulse transmission is denoted  $s_i(z)$ , where  $z$  is a certain depth from the transducer and corresponds to the elapsed time after pulse transmission (fast-time);  $i$  is the pulse number (slow-time). The RF signal is quadrature demodulated by applying the following operation:

$$u_i(z) = LPF \left\{ s_i(z) e^{-j2\pi f_m 2z/c} \right\} \quad (1)$$

where  $LPF$  represents a low-pass filter,  $j = \sqrt{-1}$ ,  $f_m$  is the demodulation frequency, and  $c$  is the speed of sound. Note that  $u_i(z)$  is a complex signal with in-phase (real) and quadrature (imaginary) components (IQ data).

In the conventional auto-correlation method, the radial displacement is estimated as [16]:

$$\hat{\Delta r} = \frac{1}{2} \frac{\angle \hat{R}(0,1)}{2\pi} \frac{c}{f_m} \quad (2)$$

where  $\angle$  denotes phase angle, and  $\hat{R}(0,1)$  is the complex-valued auto-correlation estimate of  $u_i(z)$  at a certain depth  $z$ . The conventional auto-correlation method is unbiased, provided that the demodulation frequency  $f_m$  is equal to the center frequency of the received RF signal. However, frequency dependent attenuation causes variations in the RF center frequency.

In the modified auto-correlation method, the RF center frequency is estimated as [17, 18, 25]:

$$\hat{f}_0 = f_m + \frac{\angle \hat{R}(1,0)}{2\pi} f_s \quad (3)$$

where  $f_s$  is the radial sampling frequency, and  $\hat{R}(1,0)$  is the complex-valued auto-correlation estimate of  $u_i(z)$ , in the radial direction. The last term on the right hand

side of Eq. 3 is an estimate of the mean frequency of the quadrature demodulated signal, and corresponds to the deviation between the demodulation frequency  $f_m$  and the RF center frequency. In the modified auto-correlation method, the demodulation frequency used in the conventional auto-correlation method (Eq. 2), is replaced by the estimated RF center frequency (Eq. 3):

$$\hat{\Delta r} = \frac{1}{2} \frac{\angle \hat{R}(0, 1)}{2\pi} \frac{c}{\hat{f}_0} \quad (4)$$

In this study, the sample mean estimator was used for determining  $\hat{R}$ :

$$\hat{R}(m', n') = \frac{1}{M - m'} \frac{1}{N - n'} \sum_{m=0}^{M-m'-1} \sum_{n=0}^{N-n'-1} u_n(m)^* u_{n+n'}(m + m'), \quad m' \geq 0, \quad n' \geq 0 \quad (5)$$

where  $m'$  and  $n'$  are the radial and temporal lags, while  $M \times N$  is the estimation window.

## 2.2 Tracking system

We developed a software application for tracking of vessel walls. A block diagram of the software application is shown in Fig. 1a. The application consists of: a user-interface module, a tracking module, and a module for loading ultrasound image data. The software system was implemented in C++/MFC (Microsoft Foundation Classes) and runs under Windows95 and WindowsNT (Microsoft Corp., USA). After data acquisition, the IQ data is stored by the ultrasound scanner in a data file. The file is loaded by the application and the IQ data is modulated up to RF data (RF reconstructor, Fig. 1a). The RF data is visualized (RF gray-scale renderer, Fig. 1a) as a gray-scale image (Fig. 1b). The user then selects an initial point in the RF gray-scale image (cursor position, Fig. 1a) and the wall is tracked from IQ data according to the displacement estimator (Wall tracker, Fig. 1a). For visual inspection, the wall displacement curve is shown on top of the RF gray-scale image (red line, Fig. 1b). When the user moves the cursor around in the gray-scale image, the RF signal (Fig. 1c) at the current cursor position is plotted (RF signal renderer, Fig. 1a) in a separate window.

## 2.3 Ultrasound recordings

The ultrasound recordings were performed on the left common carotid artery, 3–5 cm proximal to the bifurcation of the internal and external carotid arteries. Guided by two-dimensional (2D) gray-scale imaging, RF data was acquired by a 10 MHz linear array probe on a System FiVe ultrasound scanner (GE Vingmed Ultrasound, Norway). The transmission frequency was 8 MHz, and the length of the electrical drive-pulse was 3 half-periods. The RF data was stored as quadrature demodulated IQ data at

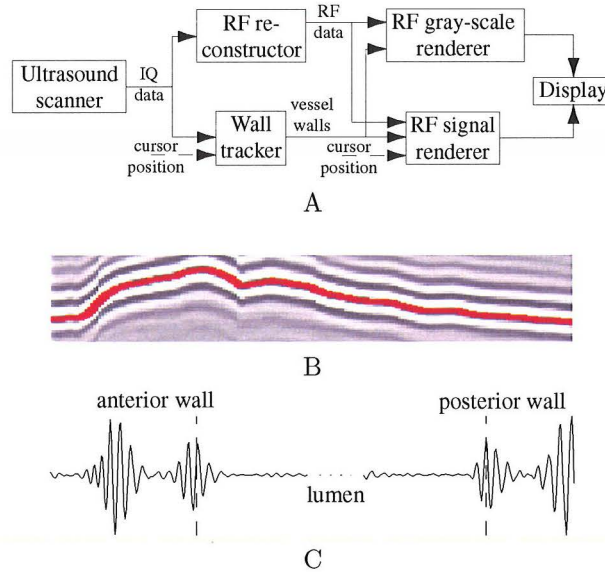


**Figure 1:** Panel A: Block diagram of the wall tracking system. Panel B: RF gray-scale image. Panel C: RF signal. The red line in B is the tracked vessel wall. The vertical dashed lines in C correspond to the tracked vessel walls. Note that a portion of the RF signal has been removed (dotted line).

a sampling frequency of 10 MHz. The pulse repetition frequency (PRF) was 200 Hz. The files also contained other acquisition parameters, such as demodulation frequency  $f_m$ .

## 2.4 Simulations

This section describes computer simulations of vessel-wall motion. These simulations were used for estimating bias and variance of the modified auto-correlation method, the conventional auto-correlation method and two different cross-correlation methods. In the cross-correlation methods, the displacement is estimated by locating the maximum of the cross-correlation function between two successive RF signals [4]. In general, the location of the maximal cross-correlation does not coincide with the sampling grid and the maximum has to be found by interpolating the sampled cross-correlation function. Two different techniques were tested. The first technique [19] (cross-correlation with parabolic interpolation), locates the maximum of the sampled cross-correlation function (coarse estimate), fits a parabola to the cross-correlation function around its maximum, and uses the maximum of the parabola as the final estimate (method described by Loupas et al. [18], p. 681). The second technique [7] (cross-correlation with model-based interpolation), relies on a Gaussian model of the RF cross-correlation

function and uses the sampled cross-correlation function at a limited number of points (method described by Hoeks et al. [11], p. 729).

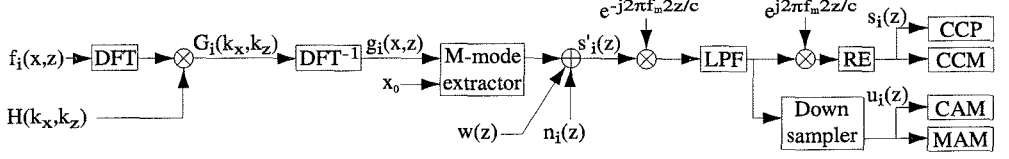


**Figure 2:** Block diagram of the signal simulation. The object  $f_i(x, z)$  is Fourier transformed and multiplied by the point spread function  $H(k_x, k_z)$ . The resulting frequency representation ( $G_i(k_x, k_z)$ ) is inverse Fourier transformed. From each image  $g_i(x, z)$ , the RF signal at the lateral position  $x_0$  is selected and organized in an RF M-mode. Thermal noise  $n_i(z)$  and stationary reverberations  $w(z)$  are added, and the resulting signal  $s'_i(z)$  is quadrature demodulated and low-pass filtered. The filtered data is modulated up to RF data ( $s_i(z)$ ) and used by the cross-correlation methods (CCP and CCM) or down-sampled to 10 MHz ( $u_i(z)$ ) and used by the auto-correlation methods (CAM and MAM). DFT - digital Fourier transform. LPF - low pass filter. RE - real operator.

A block diagram of the simulations is shown in Fig. 2. The ultrasound imaging process was assumed linear and spatially invariant. The latter assumption is appropriate in the transmit focal zone. An ultrasound image  $g_i$  is then given as a convolution between the point spread function  $h$  and a function  $f_i$  representing the acoustical properties of the object. For a linear scan, this is described by:

$$g_i(x, z) = \int h(x_1, y_1, z_1) f_i(x - x_1, -y_1, z - z_1) dx_1 dy_1 dz_1 \quad (6)$$

where  $x$ ,  $y$  and  $z$  are the coordinates in the lateral, elevation and radial directions, respectively, and subscript  $i$  denotes image number. Assume further that  $f(x, y, z) = \tilde{f}(x, z)$  within the beam (i.e. in the region where  $h(x, y, z) \neq 0$ ). For blood vessels, this will be the case when the  $y$ -direction corresponds to the longitudinal direction of the vessel, and the  $x$ - $z$  plane corresponds to the cross section of the vessel. Eq. 6 can then be written as:

$$g_i(x, z) = \int \tilde{f}_i(x - x_1, z - z_1) \int h(x_1, y_1, z_1) dy_1 dx_1 dz_1 \quad (7)$$

For a rectangular aperture, the point spread function is separable in the  $x$ - and  $y$ -directions (i.e.  $h(x, y, z) = h_{xz}(x, z) h_{yz}(y, z)$ ), and

$$\int h(x, y, z) dy = h_{xz}(x, z) \int h_{yz}(y, z) dy = \tilde{h}(x, z) \quad (8)$$

Inserting this into Eq. 7 gives:

$$g_i(x, z) = \int \tilde{h}(x_1, z_1) \tilde{f}_i(x - x_1, z - z_1) dx_1 dz_1 \quad (9)$$

which is a 2D convolution. In the frequency domain, this corresponds to:

$$G_i(k_x, k_z) = F_i(k_x, k_z) \cdot H(k_x, k_z) \quad (10)$$

where  $k$  denotes wave-numbers. In the simulations, the point spread function contained the following terms:

$$H(k_x, k_z) = A(k_x, k_z) \cdot P(k_z) \cdot k_z^2 \cdot \alpha(k_z) \quad (11)$$

where  $A$  is the frequency representation of the two-way aperture,  $P$  is the Fourier transform of the transmitted ultrasound pulse, and  $\alpha$  accounts for frequency dependent attenuation. The third term on the right hand side represents Rayleigh scattering. We assumed  $P$  to be Gaussian shaped with center frequency  $f_0$  and bandwidth  $B$  defined as twice the RMS bandwidth (i.e. -17-dB bandwidth). The aperture function  $A$  was calculated as  $A_{tx} *_{k_x} A_{rx}$ , where  $*_{k_x}$  denotes one-dimensional convolution in the  $k_x$  direction. The transmitter and receiver apertures ( $A_{tx}$  and  $A_{rx}$ ) were given by:

$$A_{tx}(k_x, k_z) = A_{rx}(k_x, k_z) = \begin{cases} \frac{2\pi}{k_z} F_{\#} & , |k_x| \leq \frac{k_z}{2F_{\#}} \\ 0 & , |k_x| > \frac{k_z}{2F_{\#}} \end{cases} \quad (12)$$

where  $F_{\#}$  is the F-number. Rectangular apodization was hence used.

The time-varying object  $f_i(x, z)$  representing the vessel was generated by specifying a time-varying inner radius and wall thickness. In the first object-frame  $f_1$ , the pixels within the wall were given values that fluctuated randomly around a mean value (Gaussian distribution), whereas the pixels representing blood were set to zero. The blood signal component was neglected because scattering caused by blood is much lower than scattering caused by tissue. The first object-frame  $f_1$  was smoothed by spatial filtering. For each of the other object-frames  $f_i$ , we first calculated the positions that each pixel had in the first frame before the vessel wall was deformed. We then did spline interpolation in the first frame at the calculated positions and assigned the interpolated values to the corresponding pixels of the current frame. The pixel size was  $19.25 \mu m$ . In the radial direction, this corresponds to a sampling frequency of 40 MHz. To reduce computation time, only the upper part of the transverse section of the vessel was generated (Fig. 3A). Note that this represents a vessel with blood on each side of the wall. However, this is often the case for a portion of the common carotid artery where the internal jugular vein is positioned anterior to the artery.

Ultrasound RF data was generated by Fourier transforming the objects, applying Eq. 10 and inverse Fourier transforming the resulting frequency domain data. In each image  $g_i(x, z)$ , the RF signal at the middle of the vessel (lateral position  $x_0$ ) was selected (M-mode extractor, Fig. 2). The selected RF signals were organized in an array (RF M-mode). Thermal noise was simulated by adding white Gaussian noise to all sample points in the ultrasound RF M-mode ( $n_i(z)$ ), whereas stationary reverberations were simulated by generating one Gaussian noise vector ( $w(z)$ ) and adding this to all the lines of the RF M-mode. The signal-to-noise ratio (SNR) and the signal-to-reverberation

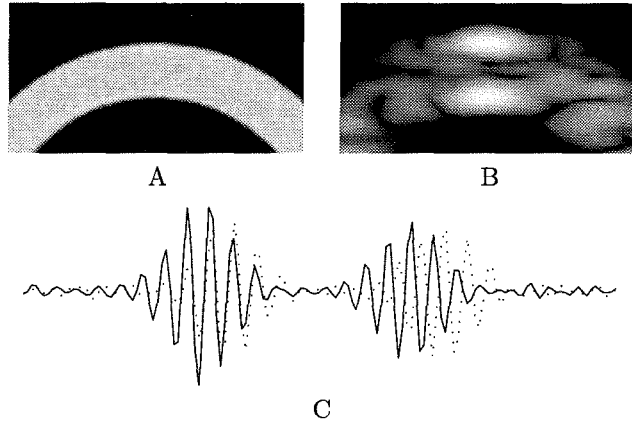


**Figure 3:** Panel A: object  $f_i(x, z)$ . Panel B: simulated ultrasound image  $g_i(x, z)$ . Panel C: a portion of the RF signal (—) at the middle of the the ultrasound image. After the wall has moved, the RF signal has changed (···).

ratio (SRR) were defined as the power of the tissue signal divided by the power of the noise and reverberations, respectively. The total signal  $s'_i(z)$ , including noise and stationary reverberations, was quadrature demodulated (Eq. 1) and low-pass filtered with a bandwidth matched to the pulse bandwidth  $B$  (right part of Fig. 2). The filtered data was (1) modulated up to RF data ( $s_i(z)$ ) and used by the cross-correlation methods (CCP and CCM) or (2) down-sampled to 10 MHz ( $u_i(z)$ ) and used by the auto-correlation methods (CAM and MAM). Table 1 shows the parameter common to all simulations. All the simulations were performed by using Matlab v5.3 (MathWorks Inc., USA). An example of the simulation output is shown in Fig. 3B– 3C.

Parameter	Symbol	Value	Unit
Speed of sound	$c$	1540	m/s
Pulse center frequency	$f_0$	8	MHz
Radial sampling frequency	$f_s$	40	MHz
Frequency dependent attenuation	$\alpha$	2	dB/MHz
F-number (transmit and receive)	$F_{\#}$	4.5	
Demodulation frequency	$f_m$	7.28	MHz

**Table 1:** Parameters common to all simulations.

### Physiological wall-motion simulations

To imitate physiological wall motion, we generated a series of object frames (object movie) where the radius and wall thickness were changed according to measurements from the common carotid artery of a 62 years old subject (right panels, Fig. 4). The object movie contained 97 frames covering one cardiac cycle. Ultrasound RF data was generated from the object movie and the wall was tracked by the different displacement estimators. The parameters settings were as shown in Table 2.

Parameter	Symbol	Value(s)	Unit
Pulse bandwidth	B	0.25, 0.5, 0.75	$f_0$
signal-to-noise ratio	SNR	25	dB
Sample volume	M	5	$\lambda$
Packet size	N	2	lines

**Table 2:** Parameter settings for the physiological wall-motion simulations.  $\lambda$  is the transmitted wavelength, i.e.  $\lambda = c/f_0$ . Reverberation noise was not added to the RF data in these simulations.

### Evaluation of estimator bias and variance

To obtain estimates of estimator bias and variance, we generated an ensemble of 200 object movies, each containing 80 frames. From frame to frame, the vessel radius was increased by  $0.025 \lambda$ , where  $\lambda$  is the transmitted wavelength, i.e.  $\lambda = c/f_0$ . This way up to 8000, 4000 and 2000 displacement samples were generated for packet sizes of 2, 4 and 8 pulses, respectively. Such a high number of estimates ensured reliable statistics.

Parameter	Symbol	Values	Unit
Displacements	$\Delta r$	0.025, 0.05, ..., 0.225	$\lambda$
Pulse bandwidth	B	0.25, 0.5, 0.75	$f_0$
signal-to-noise ratio	SNR	5, 15, 25	dB
signal-to-reverberation ratio	SRR	5, 15, 25	dB
Sample volume	M	1, 2.5, 4	$\lambda$
Packet size	N	2, 4, 8	lines

**Table 3:** Parameter settings for bias and variance estimations.

### 3 Results

#### 3.1 Wall tracking in ultrasound recordings

Fig. 4 shows examples of wall tracking by the modified auto-correlation method (red lines), and wall tracking by the conventional auto-correlation method (yellow lines). The tracking was performed on the anterior and posterior walls of the common carotid artery of subjects aged 31 (left), 41 (middle left), 56 (middle right), and 62 (right). A sample volume of  $1.5 \lambda$ , and a packet size of two were used when tracking the walls. In these examples, the conventional auto-correlation method did not follow the same gray-scale level in the RF images, whereas the modified auto-correlation method gave displacement curves that coincide with white RF-lines.

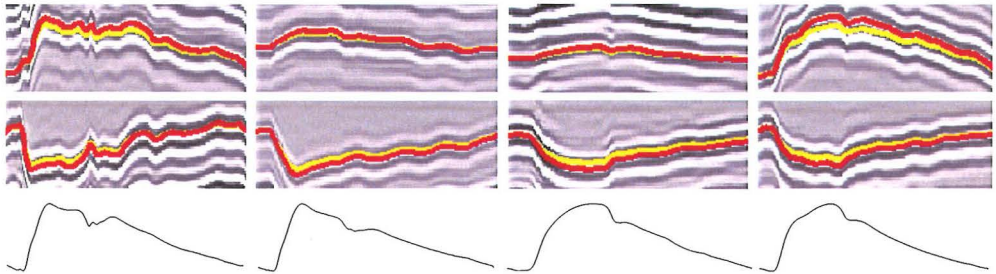


**Figure 4:** Examples of wall tracking by the modified auto-correlation method (red lines) and tracking by the conventional auto-correlation method (yellow lines). The tracking was performed on the anterior and posterior walls of the common carotid artery of subjects aged 31 (left), 41 (middle left), 56 (middle right), and 62 (right). The lower panels show diameter curves obtained by subtracting the tracked anterior wall from the tracked posterior wall. The vertical scaling is not identical for all four cases. Only diameters based on the modified auto-correlation method are shown.

#### 3.2 Physiological wall-motion simulations

Fig. 5 shows examples of wall tracking when using data from physiological wall-motion simulations. In the panels A, B and C, the pulse bandwidth was  $0.25 f_0$ ,  $0.5 f_0$  and  $0.75 f_0$ , respectively. The conventional auto-correlation method overestimated wall excursion in panel A, but underestimated the wall excursion in panel C. However, when comparing the wall position at the start and end of the cardiac cycle we see little global drifting. The cross-correlation method with parabolic interpolation drifted slightly in all three cases. The cross-correlation method with model interpolation tracked nicely in panel A, but drifted slightly in panels B and C. The modified auto-correlation method gave negligible drifting in all panels.

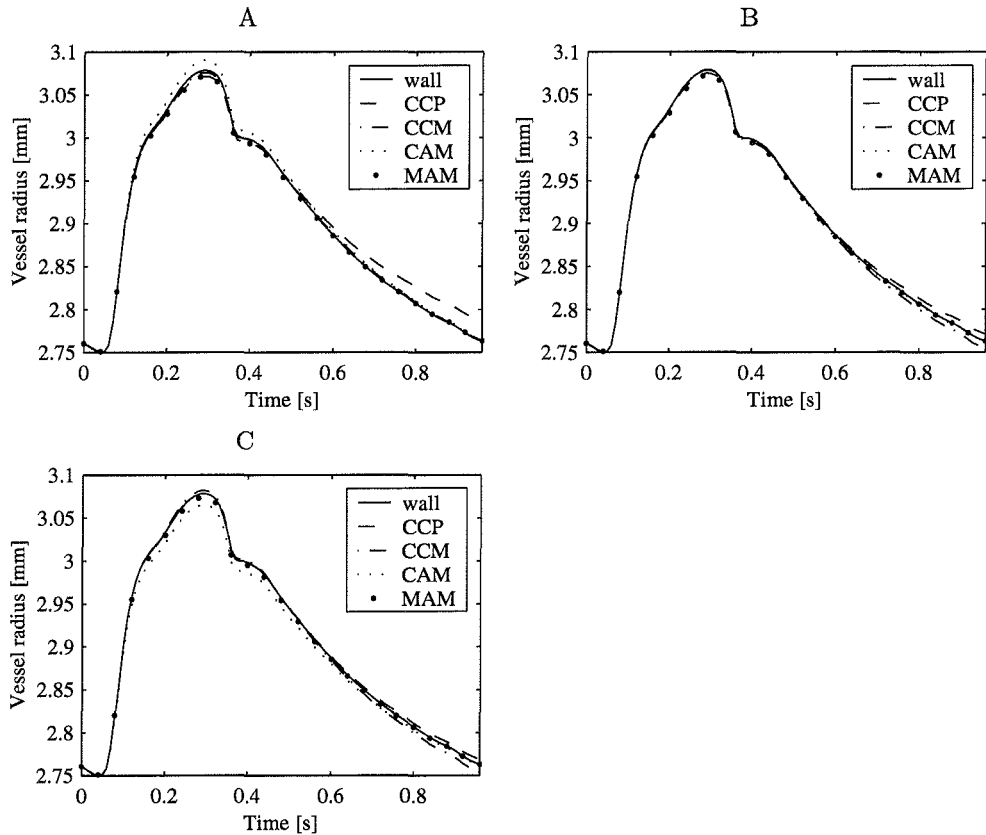


**Figure 5:** Examples of tracking when using data from the physiological wall-motion simulations. The parameter settings are given in Table 2. In the panels A, B and C, the pulse bandwidth was  $0.25 f_0$ ,  $0.5 f_0$  and  $0.75 f_0$ , respectively. (—) true vessel wall. (- - -) cross-correlation with parabolic interpolation (CCP). (- · -) cross-correlation with model interpolation (CCM). (...) conventional auto-correlation (CAM). (...) modified auto-correlation (MAM).

### 3.3 Evaluation of estimator bias and variance

#### Packet size

Fig. 6 shows the bias and standard deviation as a function of displacement for packet sizes equal to 2, 4 and 8 pulses. The fixed parameters for these simulations were: pulse bandwidth of  $0.5 f_0$ , SNR of 15 dB, SRR of 25 dB and sample volume of 2.5 wavelengths. As expected, Fig. 6 shows that the standard deviation of the estimators was inversely related to the packet size. For all packet sizes, the conventional

auto-correlation method had the highest standard deviation, whereas the modified auto-correlation method and the cross-correlator with model interpolation had nearly identical standard deviations. The modified auto-correlation method had the lowest bias of all methods, but the bias of all estimators was not much affected by the packet size.

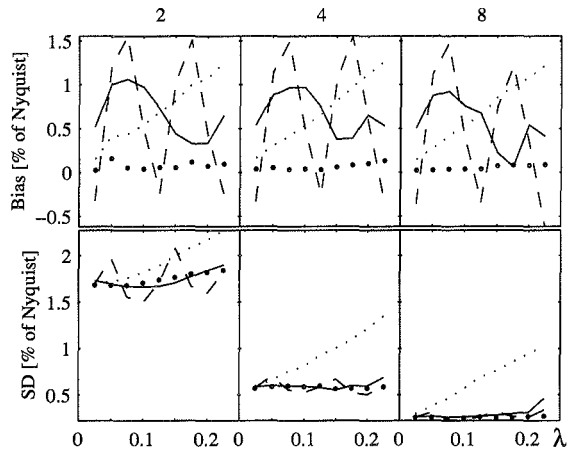


**Figure 6:** Bias and standard deviation as a function of displacement for packet sizes equal to 2, 4 and 8 pulses. (- - -) cross-correlation with parabolic interpolation. (—) cross-correlation with model interpolation. (...) conventional auto-correlation. (-.-) modified auto-correlation.

### Sample volume

Fig. 7 shows the bias and standard deviation as a function of displacement for sample volumes equal to 1, 2.5 and 4 wavelengths. The fixed parameters for these simulations were: pulse bandwidth of  $0.5 f_0$ , SNR of 15 dB, SRR of 25 dB and packet size of 4 pulses. Fig. 7 shows that the performance of the auto-correlation methods did not depend much on the size of the sample volume, whereas the cross-correlation methods became unreliable for the shortest sample volume ( $1 \lambda$ ). For the other sample volumes, the modified auto-correlation method and the cross-correlator with model interpolation had nearly identical standard deviations. This indicates that the cross-correlation methods probably detect false peaks for the shortest sample volume.

### Signal-to-noise ratio

Fig. 8 shows the bias and standard deviation as a function of displacement for signal-to-noise ratios equal to 5, 15 and 25 dB. The fixed parameters for these simulations were:

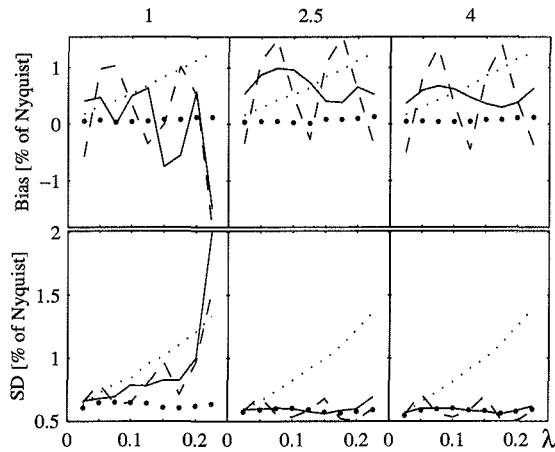


**Figure 7:** Bias and standard deviation as a function of displacement for sample volumes equal to 1, 2.5 and 4 wavelengths. Line styles described in legend for Fig. 6.

pulse bandwidth of  $0.5 f_0$ , SRR of 25 dB, packet size of 4 pulses and sample volume of 2.5 wavelengths. As expected, for all estimators the standard deviation increased with the noise level. The conventional auto-correlation method had the highest standard deviation of all methods, but the deviation between the methods was quite small for a signal-to-noise ratio of 5 dB. This indicates that the benefits of estimating the RF center frequency is marginal under heavy noise conditions. However, the bias, which is the most important factor in vessel tracking, was not much affected by the noise level.

### Signal-to-reverberation ratio

Fig. 9 shows the bias and standard deviation as a function of displacement for signal-to-reverberation ratios equal to 5, 15 and 25 dB. The fixed parameters for these simulations were: pulse bandwidth of  $0.5 f_0$ , SNR of 25 dB, packet size of 4 pulses and sample volume of 2.5 wavelengths. For all methods, both the bias and variance were affected by changing the reverberation level. At a signal-to-reverberation ratio of 5 dB, all methods became unreliable.

### Pulse bandwidth

Fig. 10 shows the bias and standard deviation as a function of displacement for pulse bandwidths equal to 0.25, 0.5 and  $0.75 f_0$ . These pulse bandwidths correspond to pulse lengths of approximately 10.2, 5.1 and 3.4 wavelengths, respectively. The fixed

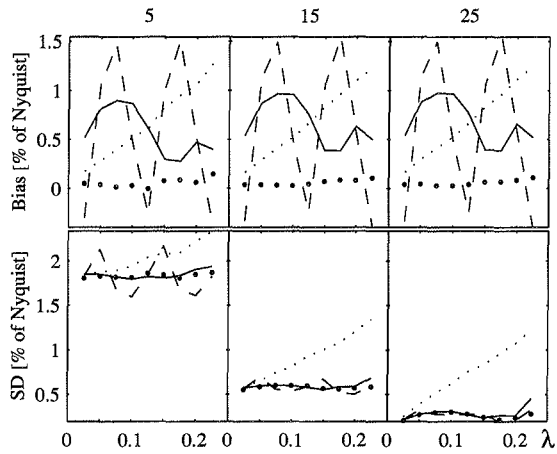


**Figure 8:** Bias and standard deviation as a function of displacement for signal-to-noise ratios equal to 5, 15 and 25. Line styles described in legend for Fig. 6.

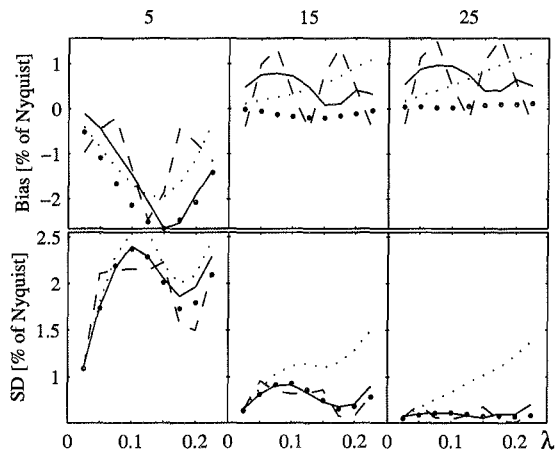


**Figure 9:** Bias and standard deviation as a function of displacement for signal-to-reverberation ratios equal to 5, 15 and 25. Line styles described in legend for Fig. 6.

parameters for these simulations were: SNR of 15 dB, SRR of 25 dB, packet size of 4 pulses and sample volume of 2.5 wavelengths. The bias of the cross-correlation methods increased with decreasing pulse lengths, whereas the bias of the modified

auto-correlation method did not change much. At a pulse bandwidth of  $0.25 f_0$ , the bias was nearly the same for both the modified auto-correlation method and the cross-correlator with model interpolation. This illustrates the fact that De Jong et al. [7] used a narrow bandwidth assumption in the development of the cross-correlator with model interpolation. The bias of the conventional auto-correlation method changed much for the three alternative pulse lengths. The reason is that the same demodulation frequency was used in all three cases. As expected, the standard deviation of the conventional auto-correlation method increased with decreasing pulse lengths. The reason is that the shortest pulse gives the fastest decorrelation.

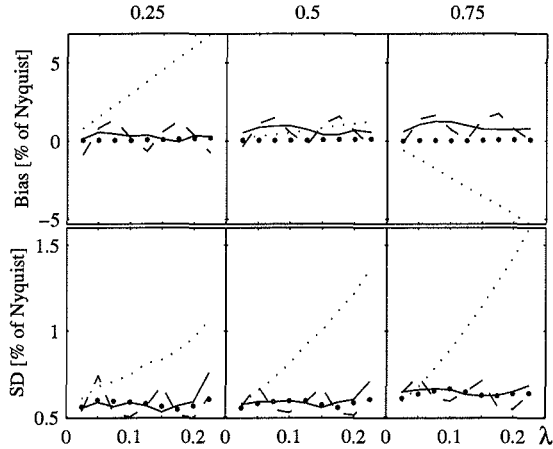


**Figure 10:** Bias and standard deviation as a function of displacement for pulse bandwidths equal to  $0.25$ ,  $0.5$  and  $0.75 f_0$ . Line styles described in legend for Fig. 6.

## 4 Discussion

Tracking algorithms based on (1) the modified auto-correlation method [17, 18, 25] and (2) the conventional auto-correlation method [16] were tested on ultrasound data in four example subjects. The results indicated that the modified auto-correlation method performed better than the conventional auto-correlation method. To make a systematic evaluation of the estimators, we performed computer simulations of a moving vessel wall, where we varied simulation parameters such as pulse bandwidth, signal-to-noise ratio, signal-to-reverberation ratio, packet size and sample volume. In addition to the modified and the conventional auto-correlation methods, we tested two cross-correlation methods [7, 19]. In the simulations, the modified auto-correlation method had the lowest bias of all methods, and a variance in the same range as the

cross-correlation methods.

The standard deviation of the cross-correlation methods was in the same range as the standard deviation of the modified auto-correlation method. This is in accordance with other simulation studies [11, 18]. However, the most important factor in vessel tracking is the bias of the displacement estimator. Under the specific simulation conditions considered in this study, the bias of the cross-correlation methods was not proportional to the displacement magnitudes. The incremental displacements of the vessel wall are normally larger in the expansion phase (early systole) than in the deflation phase (late systole and diastole). When the bias is not proportional to the displacement magnitude, this may lead to global drifting (distance between the true and the estimated wall positions after tracking one cardiac cycle). Lai et al. [17] have shown that the bias of the cross-correlator with parabolic interpolation decreases when the sampling frequency is increased from 4 times  $f_0$  to 8 times  $f_0$ . However, at a sampling frequency of 8 times  $f_0$  they still observed estimation bias. For the cross-correlator with model interpolation, Hoeks et al. [11] recommended a sampling frequency of 4 times  $f_0$ . In our simulations, the sampling frequency was 5 times  $f_0$ , but still the cross-correlator with model interpolation gave estimation bias.

For the conventional auto-correlation method, the bias was higher than for the modified auto-correlation method and some local drifting was observed (Fig. 5). However, the bias was proportional to the displacement magnitudes (Figs. 6 - 10), thus giving little global drifting (Fig. 5). The bias of the conventional auto-correlation method depends on the difference between the chosen demodulation frequency  $f_m$  and the instantaneous RF center frequency. Because the instantaneous RF center frequency is affected by frequency dependent attenuation [8], the local drifting may become substantial and the algorithm may in some cases track out of the wall and into the vessel cavity. In the ultrasound recordings from the four subjects (Fig. 4), the -17-dB bandwidth of the RF signals were in the range 4–5 MHz. In such wide band signals, the center frequency of the received signal will be heavily affected by frequency dependent attenuation.

## 5 Conclusion

This study illustrates that auto-correlation with RF center frequency estimation, as opposed to conventional auto-correlation, tracks the vessel wall properly even though the demodulation frequency deviates from the instantaneous RF center frequency. This is important in wide bandwidth signals where the RF center frequency is severely affected by frequency dependent attenuation. On the basis of computer simulations of vessel wall-motion, we conclude that auto-correlation with RF center frequency estimation performs better than the conventional auto-correlation method and two alternatives of the cross-correlation method. Compared to the cross-correlation methods, the modified auto-correlation method has lower complexity in terms of number of computations and sampling rate requirements, and is therefore the preferred choice of method.

## 6 Acknowledgments

This study was supported by Program for Medical Technology at the Norwegian University of Science and Technology. We thank Erik Østlyngen for developing parts of the software application, Andreas Heimdal for helpful discussions about the computer simulations, and Nancy Lea Eik-Nes for revision of the paper.

## References

1. Aakhus S, Torp H, Haugland T, Hatle L. Non-invasive estimates of aortic root pressures: external subclavian arterial pulse tracing calibrated by oscillometrically determined brachial arterial pressures. *Clin Physiol* 1993;13:573–86.
2. Arndt JO, Klauske J, Mersch F. The diameter of the intact carotid artery in man and its change with pulse pressure. *Pflugers Arch Gesamte Physiol Menschen Tiere* 1968;301:230–40.
3. Benthin M, Dahl P, Ruzicka R, Lindstrom K. Calculation of pulse-wave velocity using cross correlation—effects of reflexes in the arterial tree. *Ultrasound Med Biol* 1991;17:461–9.
4. Bonnefous O, Pesque P. Time-domain formulation of pulse doppler ultrasound and blood velocity estimation by cross correlation. *Ultrason Imag* 1986;8:73–85.
5. Brands PJ, Willigers JM, Ledoux LA, Reneman RS, Hoeks AP. A noninvasive method to estimate pulse wave velocity in arteries locally by means of ultrasound. *Ultrasound Med Biol* 1998;24:1325–35.
6. Colan SD, Borow KM, Neumann A. Use of the calibrated carotid pulse tracing for calculation of left ventricular pressure and wall stress throughout ejection. *Am Heart J* 1985;109:1306–10.
7. De Jong PGM, Arts T, Hoeks APG, Reneman RS. Determination of tissue motion velocity by correlation interpolation of pulsed ultrasonic echo signals. *Ultrason Imaging* 1990;12:84–98.
8. Duck FA. *Physical properties of tissue. A comprehensive reference book.* London: Academic Press, 1990.
9. Groves DH, Powalowski T, White DN. A digital technique for tracking moving interfaces. *Ultrasound Med Biol* 1982;8:185–90.
10. Hansen F, Mangell P, Sonesson B, Lanne T. Diameter and compliance in the human common carotid artery—variations with age and sex. *Ultrasound Med Biol* 1995;21:1–9.

11. Hoeks AP, Arts T, Brands PJ, Reneman RS. Comparison of the performance of the RF cross correlation and doppler autocorrelation technique to estimate the mean velocity of simulated ultrasound signals. *Ultrasound Med Biol* 1993; 19:727-40.
12. Hoeks AP, Brands PJ, Smeets FA, Reneman RS. Assessment of the distensibility of superficial arteries. *Ultrasound Med Biol* 1990;16:121-8.
13. Hoeks AP, Ruissen CJ, Hick P, Reneman RS. Transcutaneous detection of relative changes in artery diameter. *Ultrasound Med Biol* 1985;11:51-9.
14. Hokanson DE, Mozersky DJ, Sumner DS, Strandness DE. A phase-locked echo tracking system for recording arterial diameter changes in vivo. *J Appl Physiol* 1972;32:728-33.
15. Imura T, Yamamoto K, Kanamori K, Mikami T, Yasuda H. Non-invasive ultrasonic measurement of the elastic properties of the human abdominal aorta. *Cardiovasc Res* 1986;20:208-14.
16. Kasai C, Namekawa K, Koyano A, Omoto R. Real-time two-dimensional blood flow imaging using an autocorrelation technique. *IEEE Trans Sonics Ultrason* 1985;SU-32:458-463.
17. Lai X, Torp H, Kristoffersen K. An extended autocorrelation method for estimation of blood velocity. *IEEE Trans UFFC* 1997;44:1332-42.
18. Loupas T, Powers JT, Gill RW. An axial velocity estimator for ultrasound blood flow imaging, based on a full evaluation of the doppler equation by means of a two-dimensional autocorrelation approach. *IEEE Trans UFFC* 1995;42:672-88.
19. Moddemeijer R. On the determination of the position of extrema of sampled correlators. *IEEE Trans Signal Proc* 1991;39:216-219.
20. Parker KH, Jones CJ, Dawson JR, Gibson DG. What stops the flow of blood from the heart? *Heart Vessels* 1988;4:241-5.
21. Reneman RS, van Merode T, Hick P, Muyltjens AM, Hoeks AP. Age-related changes in carotid artery wall properties in men. *Ultrasound Med Biol* 1986; 12:465-71.
22. Sindberg Eriksen P, Gennser G, Lindstrom K, Benthin M, Dahl P. Pulse wave recording-development of a method for investigating foetal circulation in utero. *J Med Eng Technol* 1985;9:18-27.
23. Sugawara M. Wave intensity analysis: a new method for the dynamic study of heart-vessel interactions. In: *European Medical and Biological Engineering Conference, 1999, Vienna, Austria*. vol. I, 1999; 24-27.

24. Tardy Y, Meister JJ, Perret F, Brunner HR, Arditi M. Non-invasive estimate of the mechanical properties of peripheral arteries from ultrasonic and photoplethysmographic measurements. *Clin Phys Physiol Meas* 1991;12:39-54.
25. Torp H, Kristoffersen K. US5560363: Method for calculation of blood velocity and blood velocity spread from multi gated doppler signals. Assignee: Vingmed Sound A/S, Horten, Norway, 1995.



# Paper D



# An ultrasound-based method for determining pulse wave velocity in the carotid artery

Stein Inge Rabben<sup>1</sup>, Nikos Stergiopoulos<sup>2</sup>, Leif Rune Hellevik<sup>3</sup>, Otto A. Smiseth<sup>4</sup>, Stig Slørdahl<sup>5</sup>, Stig Urheim<sup>4</sup> and Bjørn Angelsen<sup>1</sup>

<sup>1</sup>Department of Physiology and Biomedical Engineering, NTNU, Trondheim, Norway

<sup>2</sup>Biomedical Engineering Laboratory, EPFL, Lausanne, Switzerland

<sup>3</sup>MTF/Division of Applied Mechanics, NTNU, Trondheim, Norway

<sup>4</sup>Institute for Surgical Research, National Hospital, Oslo, Norway

<sup>5</sup>Department of Medicine, Section of Cardiology, University Hospital Trondheim, Norway

## Abstract

The vascular properties, which are major determinants of left ventricular load, change in several diseases such as hypertension, diabetes and arteriosclerosis. Hence, there is a need for clinical methods that quantify vascular properties. The pulse wave velocity, which is related to arterial stiffness and determines the timing of the reflected wave, can be estimated from the arterial cross-sectional area and pulse pressure (Bramwell-Hill method). Today, arterial diameter waveforms are measured reliably by ultrasound echo-tracking, whereas the pulse pressure of the brachial artery is used as a substitute for the local pulse pressure. In this paper, a new method for estimating pulse wave velocity is presented (the area-flow method). With this method, the pulse wave velocity is estimated as the ratio between flow and area during the reflection-free period of the cardiac cycle. Hence, the use of brachial pulse pressures is avoided. The area-flow method requires measurements of blood flow, and we also present a method for estimating blood flow from pulsed wave Doppler velocity measurements. The flow estimation method is derived by eliminating the pressure gradient in the Womersley's solution for pulsatile flow in rigid tubes. Data from 21 human subjects (age 23–74) and four dogs showed that the area-flow method and the Bramwell-Hill method agreed well on average. When dividing the humans into three separate age groups, both methods gave group means that increased with age. As expected, the estimated pulse wave velocity also decreased when the aortic pressure was lowered in two of the dogs. However, on a per-subject basis, discrepancies were observed between the methods, indicating that the methods cannot be used interchangeably.

Unpublished

## 1 Introduction

The vascular properties, which are major determinants of left ventricular load, change in several diseases such as hypertension, diabetes and arteriosclerosis. Hence, there is a need for clinical methods that quantify vascular properties. In particular, it would be of value to identify early changes in vascular function that are due to arteriosclerosis. Furthermore, in the treatment of patients with hypertension it is of interest to know the functional status of the arterial vasculature and possibly to identify candidates for specific drug therapy.

Pulse wave velocity has usually been measured by estimating the delay time between the diameter waveforms recorded simultaneously at two different positions along the vessel [1, 14]. However, this technique depends on a reliable identification of the foot of the diameter waveforms, and a sufficiently high pulse repetition frequency so that the time-delay between the waveforms can be precisely determined.

A potentially more robust technique, is to estimate the pulse wave velocity via the Bramwell-Hill expression [3]:

$$c_{BH} = \sqrt{\frac{\bar{A}}{\rho} \cdot \frac{PP}{\Delta A}} \quad (1)$$

where  $\bar{A}$  is the mean cross-sectional area of the vessel,  $\Delta A$  is the difference between systolic and diastolic areas,  $PP$  is pulse pressure, and  $\rho$  is the blood density. Usually, the brachial pulse pressure is used as a substitute for the local pulse pressure. However, differences between the brachial and carotid pressures may exist due to wave propagation and reflections [12].

Recently, Brands et al. [5] presented a novel technique that estimates pulse wave velocity from diameter measurements. For unidirectional waves, the ratio of the temporal and the longitudinal diameter gradients equals the pulse wave velocity. By calculating this ratio during the reflection-free period of the cardiac cycle, they obtained estimates of pulse wave velocity.

The first aim of this study was to present an alternative method for determining pulse wave velocity (the area-flow method). Eq. 1 is based on measurements of area and pressure. However, since pressure, flow and cross-sectional area are related by the wave equation [11, 12], pulse wave velocity can also be estimated from area and flow measurements directly. Hence, the use of brachial pulse pressure is avoided. Further, to make the area-flow method applicable to non-invasive ultrasound recordings, our second aim was to develop a method for estimating arterial blood flow from Doppler velocity measurements. Finally, we wanted to make a comparison between the area-flow method and the Bramwell-Hill method.

## 2 Materials and methods

### 2.1 Data recordings

#### Human data

A total of 23 adults (age 23–74) were included in the comparison study after giving their informed consent. Ultrasound data were recorded as described below, while systolic and diastolic pressures of the right brachial artery were recorded oscillometrically every third minute during the examination (Scholar II / 507E Series, Criticare Systems, Waukesha, USA and Dinamap 1846 SXP, Criticon Inc., Tampa, Finland). The examinations were started after 10 minutes of rest in a sitting position. We excluded 2 of the 23 subjects because of poor image quality.

#### Animal data

Four mongrel dogs with body weight  $26 \pm 5$  kg (mean  $\pm$  SD) were given thiopentone (25 mg/kg b.w.) and morphine 100 mg IV, followed by infusion of morphine (50–100 mg/h) IV and pentobarbital 50 mg IV every hour. The animals were artificially ventilated through a cuffed endotracheal tube using room air with 20–50% oxygen. After a median sternotomy, inflatable vascular constrictors were placed around both caval veins. The experiments that were also performed for other purposes, were approved by the Norwegian Experimental Animal Board. In all dogs, central aortic pressure was measured by a 5F micromanometer-tipped catheter (Model MPC-500, Millar Instruments, Houston, USA) introduced into a femoral artery and positioned in the thoracic aorta near the orifice of the left carotid artery. In addition, in two of the dogs, the left common carotid artery pressure was measured by a 2F micromanometer-tipped catheter (Model SPR-407, Millar Instruments, Houston, USA) introduced in the left external carotid artery. Pressure data were digitized at 200 Hz by an ultrasound scanner and stored for further analysis together with the simultaneously recorded ultrasound data (see below). The pressure transducers were calibrated by use of a mercury manometer prior to each experiment. A fluid-filled catheter in the abdominal aorta was used for absolute pressure reference. Recordings were first taken during baseline. In two of the dogs, we then inflated the caval constrictors and did recordings after the systolic aortic pressure had decreased to approximately 60 mmHg.

#### Ultrasound recordings

A System FiVe ultrasound scanner (GE Vingmed Ultrasound, Horten, Norway) with a 10 MHz linear array probe was used for recording ultrasound data. The recordings were performed on the left common carotid artery, 3–5 cm proximal to the bifurcation of the internal and external carotid arteries. First, we recorded 3–5 (dogs: 5–10) cardiac cycles of ultrasound radio frequency (RF) data for the extraction of vessel diameter. If necessary, we steered the RF M-line perpendicular to the artery. Subsequently, we

recorded 8–10 (dogs: 10–20) cardiac cycles of pulsed wave (PW) Doppler data for extraction of blood velocities. To obtain maximum velocities across the vessel, the sample volume of the PW Doppler was made large enough to cover the central portion of the vessel's cross-section. In all recordings, the steering of the Doppler line was 30 degrees, and the angle correction was 45–60 degrees. In the human subjects, the criterion for proper alignment of the image plane relative to the artery was visible intima layers at both anterior and posterior vessel walls. In the dogs, the intima layer could not be seen, and therefore the image plane giving the largest vessel diameter was used.

## 2.2 Estimation of pulse wave velocity (the area-flow method)

Propagation of pressure (P) and flow (Q) waves in the arterial system is governed by the wave equation [11, 12], with pulse wave velocity:

$$c = \sqrt{\frac{\bar{A}}{\rho} \cdot \frac{1}{C_A}} \quad (2)$$

where  $\bar{A}$  is the mean cross-sectional area of the vessel,  $\rho$  is the blood density, and  $C_A = \frac{dA}{dP}$  is the local area compliance of the vessel. Another quantity relating pressure and flow waves in the arterial system is the characteristic impedance, which, in absence of reflections, is defined as  $Z_c = \frac{dP}{dQ}$ . The characteristic impedance is, hence, related to compliance, area and flow:

$$Z_c = \frac{dP}{dA} \cdot \frac{dA}{dQ} = \frac{1}{C_A} \cdot \frac{dA}{dQ} \quad (3)$$

However, the solution of the wave equation [11, 12] shows that the characteristic impedance is also related to compliance through the following expression:

$$Z_c = \sqrt{\frac{\rho}{\bar{A}} \cdot \frac{1}{C_A}} \quad (4)$$

By multiplying Eqs. 2 and 4, we get:

$$c \cdot Z_c = \frac{1}{C_A} \quad (5)$$

If we insert  $Z_c$  from Eq. 3, we obtain an estimate  $c_{QA}$  of the pulse wave velocity:

$$c_{QA} = \frac{dQ}{dA} \quad (6)$$

The pulse wave velocity can therefore be obtained from recordings of flow and area, provided that the data contain a reflection-free period during the cardiac cycle. We know that in most individuals the early systolic wave is reflection free. This can be checked by separating the pressure wave into its forward and backward components [10, 16].

### Blood flow estimation

Volume flow is difficult to measure by ultrasound because the blood velocity estimates are unreliable near the vessel wall due to the strong tissue signal. However, the maximum blood velocities across the vessel can be measured by PW Doppler. In this section, we present a method for flow estimation based on an extension of Womersley's theory for pulsatile flow in rigid tubes [17]. With this method, volume flow can be estimated from maximum velocities, without knowing the pressure gradient along the vessel.

Let us assume that the blood vessel is a rigid circular tube with radius  $R$ . If the tube is filled with fluid of density  $\rho$  and viscosity  $\mu$ , and  $v(r, t)$  is the longitudinal velocity of the fluid at a distance  $r$  from the center axis of the tube, the equation of motion becomes:

$$\frac{\partial^2 v}{\partial r^2} + \frac{1}{r} \frac{\partial v}{\partial r} - \frac{1}{\nu} \frac{\partial v}{\partial t} = \frac{1}{\mu} \frac{\partial p}{\partial z} \quad (7)$$

where  $\nu = \mu/\rho$  is the kinematic viscosity. Eq. 7 is solvable if we assume that  $\partial v/\partial r$  approaches zero when  $r \rightarrow 0$ , i.e., the velocity profiles are axis-symmetric. In a rigid vessel, there will be no blood motion in the radial direction, and the pressure gradient  $\partial p/\partial z$  will be constant over the cross-section of the vessel. By letting  $r \rightarrow 0$  in Eq. 7, and applying L'Hopital's rule on the second term, we obtain:

$$\frac{1}{\mu} \frac{\partial p}{\partial z} = 2 \left. \frac{\partial^2 v}{\partial r^2} \right|_{r=0} - \left. \frac{1}{\nu} \frac{\partial v}{\partial t} \right|_{r=0} \quad (8)$$

The pressure gradient in Eq. 7 may now be substituted by Eq. 8. If we assume harmonic solutions,  $v(r, t) = V(r, \omega)e^{j\omega t}$ , the following expression describes the blood velocities:

$$V''(r, \omega) + \frac{1}{r} V'(r, \omega) + \lambda^2 V(r, \omega) = 2V''(0, \omega) + \lambda^2 V(0, \omega) \quad (9)$$

where the prime denotes differentiation with respect to radius  $r$ , and  $\lambda^2 = j^3\omega/\nu$ . The homogeneous part of Eq. 9 is a Bessel equation with the solution  $V_h(r, \omega) = c_0 J_0(\lambda r)$ , where  $J_0$  is the Bessel function of first kind order zero. A particular solution of Eq. 9 is given by  $V_p(r, \omega) = \frac{2}{\lambda^2} V''(0, \omega) + V(0, \omega)$ , and a general solution of Eq. 9 is therefore given as:

$$V(r, \omega) = V_h(r, \omega) + V_p(r, \omega) = c_0 (J_0(\lambda r) - 1) + V(0, \omega) \quad (10)$$

Here we have used the fact that  $V''(0, \omega) = -c_0 \lambda^2/2$ , that can be verified by solving the differentiated homogeneous solution  $V_h''(r, \omega)$  for  $r = 0$ . Because we require that the velocities are zero at the vessel boundary,  $V(R, \omega) = 0$ , Eq. 10 becomes:

$$V(r, \omega) = V(0, \omega) \frac{J_0(\alpha j^{3/2} r/R) - J_0(\alpha j^{3/2})}{1 - J_0(\alpha j^{3/2})} \quad (11)$$

where  $\alpha = R\sqrt{\omega/\nu}$  is the Womersley number. From Eq. 11 we may estimate velocity profiles across the vessel by knowing only the velocities at the center axis  $v(0, t)$ , the mean vessel radius  $R$ , and the kinematic viscosity  $\nu$ . Integration of Eq. 11 over the vessel radius yields the volume flow:

$$Q(\omega) = V(0, \omega)\pi R^2 \frac{1 - F_{10}(\alpha)}{1 - 1/J_0(\alpha j^{3/2})} \quad (12)$$

with the Womersley function defined as  $F_{10}(\alpha) = 2J_1(\alpha j^{3/2}) / (\alpha j^{3/2} J_0(\alpha j^{3/2}))$ , where  $J_1$  is the Bessel function of first kind order one. The time-varying volume flow may now be estimated by applying the Fourier transform to the center axis velocities  $v(0, t)$ , by applying Eq. 12 on each harmonic of the center axis velocities, and by applying the inverse Fourier transform to the results of Eq. 12.

In this study, the center axis velocities were assumed identical to the maximum velocities of the PW Doppler spectra. To obtain maximum velocities, the automatic tracing algorithm of the System FiVe ultrasound scanner was used. Since the PW Doppler spectrum has a limited frequency (velocity) resolution and high variance, we needed to average several cardiac cycles to obtain smooth velocity waveforms. After the averaging, the velocity waveform was filtered by (a zero phase-distortion) low-pass Butterworth filter with a 3 dB cutoff frequency of 20 Hz, a transition band of 20 Hz, and a stop band attenuation of at least 50 dB. In the flow calculations, the blood density  $\rho$  was set to 1060 kg/m<sup>3</sup>, and blood viscosity  $\mu$  was set to 0.0035 Pa s.

### Cross-sectional area estimation

The diameter of the vessel was tracked from the RF data according to the method of Rabben et al. [13]. To obtain smooth diameter waveforms, we averaged several cardiac cycles. By assuming axis-symmetric geometry, the cross-sectional area was estimated from the diameter measurements.

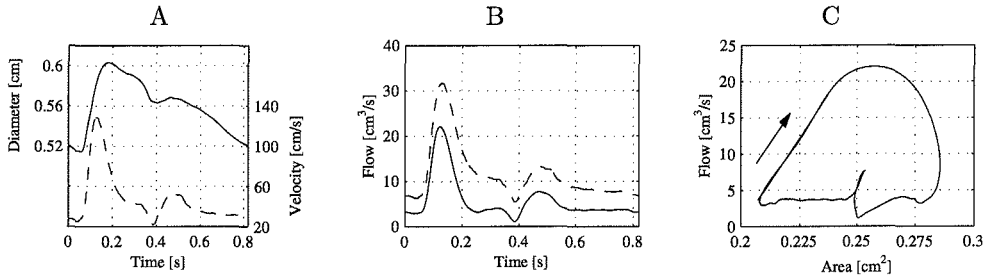
## 2.3 Comparison study

The pulse wave velocities calculated by the area-flow method (Eq. 6) were compared to pulse wave velocities calculated by the Bramwell-Hill expression (Eq. 1). After using Eqs. 1 and 6, we superposed the estimated pulse wave velocity  $c$  on the steady flow velocity [6], i.e.,  $\hat{c} = c + \bar{Q}/(\pi R^2)$ , where  $\bar{Q}$  denotes mean flow.

The agreement between the two methods was assessed by plotting the difference of the two methods against the mean of the two methods, and calculating the limits of agreement as the mean difference  $\pm$  two standard deviations (SD) of the differences [2]. The characteristics of the age groups were presented as mean  $\pm$  SD. Comparison between the age groups were performed with the non-parametric Mann-Whitney test, with a significance level of 0.05.

### 3 Results

Fig. 1 illustrates the area-flow method applied on data from a young human subject. The maximum velocities and vessel diameter were measured by ultrasound techniques (Fig. 1A). From the maximum velocities and the mean cross-sectional area, blood flow was calculated by applying Eq. 12 (Fig. 1B). Note that the flow, calculated by applying Eq. 12 (solid line), is considerably lower than the flow calculated by assuming a flat velocity profile (dashed line). Finally, the pulse wave velocity was found as the slope of the straight portion of the area-flow loop (Fig. 1C).



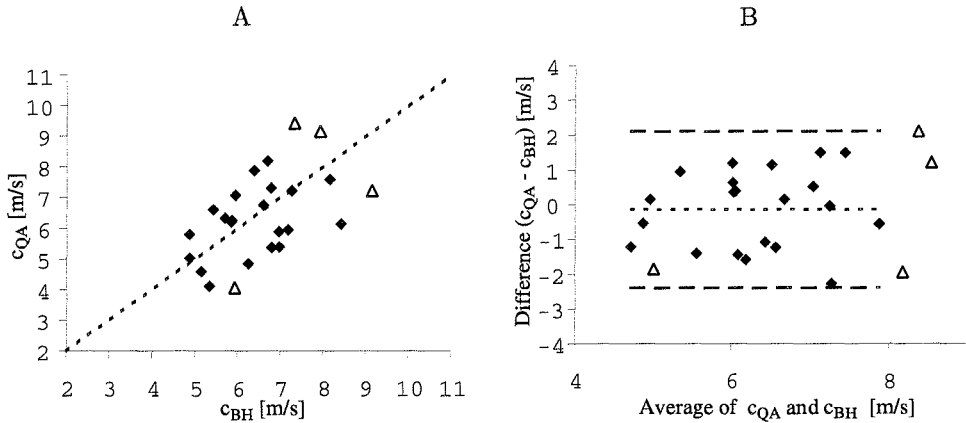
**Figure 1:** Illustration of the area-flow method for estimation of pulse wave velocity. Panel A: Measurements of the vessel diameter (—) and maximum velocities (- - -) from the left common carotid artery of a young human subject. Panel B: Flow calculated from maximum velocities and mean diameter by applying Eq. 12 (—) and by assuming a flat velocity profile (- - -). Panel C: Flow versus cross-sectional area. The slope of the straight portion of the loop corresponds to the reflection-free period of the cardiac cycle and equals the pulse wave velocity.

Table 1 lists pressure parameters and pulse wave velocity estimates at baseline and during vena cava constriction in two of the dog experiments (dog #3 and #4). The vena cava constriction decreased the mean and pulse pressures. Discrepancies were observed between the area-flow method and the Bramwell-Hill method, but for both methods, the pulse wave velocity estimates decreased during vena cava constriction.

Fig. 2A shows pulse wave velocities in 21 human subjects (filled diamonds) and four dogs (open triangles), estimated by the area-flow method plotted against pulse wave velocities estimated by the Bramwell-Hill method. The data points are scattered around the identity line (dotted line). In Fig. 2B, the difference between the two methods is plotted against the average of the two methods. For the human subjects, the mean difference between the two methods was only  $-0.14$  m/s (dotted line), whereas the range of the limits of agreement was  $-2.39$  to  $+2.10$  m/s (dashed line). Note, however, that all except one observation were within the mean difference  $\pm 1.6$  m/s. For the dogs, the mean difference between the two methods was almost identical to the mean difference for the human subjects, i.e.,  $-0.12$  m/s.

Parameter	#3		#4		units
	baseline	vcc	baseline	vcc	
$\bar{P}$	106.6	47.7	136.6	55.0	mmHg
$PP$	22.7	8.6	22.7	11.0	mmHg
$c_{QA}$	4.08	2.17	9.43	4.60	m/s
$c_{BH}$	5.94	3.00	7.33	4.94	m/s

**Table 1:** Hemodynamic parameters before (baseline) and during vena cava constriction (vcc) in dog #3 and #4.  $\bar{P}$  = mean pressure.  $PP$  = pulse pressure.  $c_{QA}$  = pulse wave velocity estimated by Eq. 6.  $c_{BH}$  = pulse wave velocity estimated by Eq. 1.



**Figure 2:** Panel A: Pulse wave velocities estimated by using Eq. 6 plotted against pulse wave velocities estimated by using the Bramwell-Hill method (Eq. 1). The filled diamonds represent the human observations, and the open triangles represent the dog observations. The dotted line is the identity line. Panel B: The difference between the two methods plotted against the average of the two methods. The dotted line is the mean difference of the human observations. The dashed lines represent the mean difference  $\pm$  two times SD of the human observations.

In Table. 2, we have divided the 21 human subjects into three age groups, and listed the mean and standard deviation of the pulse wave velocity estimates in each group. The three age groups were: below 35 years (average 28,  $N=7$ ), between 35 and 55 years (average 45,  $N=6$ ), and above 55 years (average 62,  $N=8$ ). For both methods, the group mean of the pulse wave velocity increased with age. The pulse wave velocity estimates obtained by the Bramwell-Hill method were significantly different when comparing the youngest group with the middle age group ( $p = 0.02$ ), and when comparing the youngest group with the oldest group ( $p = 0.01$ ). For the area-flow method, the pulse

wave velocity estimates tended to be different for the youngest group compared to the oldest group ( $p = 0.13$ ).

Parameter	< 35 years	35–55 years	> 55 years
$c_{QA}$	$5.82 \pm 0.98$	$6.04 \pm 1.32$	$6.69 \pm 0.97$
$c_{BH}$	$5.49 \pm 0.47$	$6.48 \pm 0.73^*$	$7.03 \pm 0.96^*$

**Table 2:** The mean and standard deviation of the pulse wave velocity estimates from three different age groups: below 35 years (< 35 years), between 35 and 55 years (35–55 years), and above 55 years (> 55 years). \* $p < 0.05$  versus the youngest age group.

## 4 Discussion

We derived a new method for estimating pulse wave velocity (area-flow method). To make the area-flow method applicable to non-invasive ultrasound recordings, we also developed a method for estimating arterial blood flow from Doppler velocity measurements. The area-flow method can therefore be based solely on non-invasive measurements of arterial diameter and blood velocity.

The area-flow method, illustrated in Fig. 1, requires flow measurements. The PW Doppler technique measures the maximum of the velocity profiles if the sample volume covers the central portion of the vessel. However, the velocity profiles are neither parabolic nor flat. We therefore developed a method for estimating blood flow from PW Doppler measurements of the maximum velocities across the vessel (Eq. 12). Since the common carotid artery exhibits little tapering, we neglected the convective term of the Navier-Stokes equation. Further, the vessel is also assumed to act as a rigid tube, so that radial velocities and non-linear effects of pressure dependent compliance could be neglected. The Navier-Stokes equation then becomes linear (Eq. 7), and all the harmonics of the center axis velocity waveform have individual velocity profiles (Eq. 11), that can be superposed to obtain the total velocity profile.

Vena cava constriction reduces the arterial blood volume and thereby the arterial pressure. The compliance increases correspondingly because of the non-linear pressure-area relation [7, 9]. The pulse wave velocity, which is related to compliance, should therefore decrease during vena cava constriction. Table 1 indicates that both the area-flow and the Bramwell-Hill methods are sensitive to the expected decrease in pulse wave velocity. The pressure dependence of the pulse wave velocity has been described by [7]:

$$c_H(P) = \left[ \frac{P}{2\rho} \left( \beta + \ln \left( \frac{P}{P_0} \right) \right) \right]^{\frac{1}{2}} \quad (13)$$

where  $\beta$  is a stiffness parameter and  $P_0$  is a reference pressure. With a reference pressure of 100 mmHg and a stiffness parameter of 10, Eq. 13 gives pulse wave velocity estimates of 9.4 m/s and 5.7 m/s at mean pressures of 137 mmHg and 55 mmHg, respectively. This shows that the decrease in pulse wave velocity estimated by the two methods (Table 1) is in the same order of magnitude as the decrease in pulse wave velocity estimated by Eq. 13.

The area-flow method was also compared with the Bramwell-Hill method on data from 21 human subjects (age 23–74). The two methods agreed well on average (mean difference of -0.14 m/s), but discrepancies were observed on a per subject basis (Fig. 2). The range of the limits of agreement (-2.39 to +2.10 m/s) was so wide that the two measurement methods can not be used interchangeably. When the humans were divided into three separate age groups, both methods gave group means that increased with age. This was expected since the arteries stiffen with age. However, only the Bramwell-Hill method gave significant differences between the youngest and the middle age groups ( $p = 0.02$ ) and between the youngest and the oldest age groups ( $p = 0.01$ ). For the area-flow method, the youngest group and the oldest group tended to be different ( $p = 0.13$ ). The number of subjects within each age group were low (6–8 subjects), thus with more observations the differences between the groups might become significant with the area-flow method as well.

There may be many reasons for the observed differences between the area-flow method and the Bramwell-Hill method: Firstly, the pulse pressure used in the Bramwell-Hill method is measured at the brachial artery. Differences between the carotid pulse pressure and the brachial pulse pressure may exist. Usually, the pulse pressure is amplified when the pressure wave propagates from the central aorta to the periphery [12]. Secondly, the blood flow estimation technique used as input to the area-flow method is reliable for laminar flow in sufficiently long straight uniform arteries. In such arteries, the velocity profiles are generally symmetric and inlet effects can be neglected. In some of the human subjects, the common carotid artery was slightly curved, which may have resulted in skewed velocity profiles. Then the assumption that the maximum velocity of the PW spectrum equals the center axis velocity is not valid. The inlet lengths for steady flow can be estimated as  $L = 0.16\bar{v}R^2/\nu$ , where  $\bar{v}$  is the mean velocity over the cardiac cycle [6]. For the human subjects of this study, the inlet-length estimates of the carotid artery were in the range 5–14 cm. Since the inlet length of oscillatory flow is expected to be shorter than for steady flow, and the length from the carotid inlet to the measurement point is larger than 14 cm, we assume that inlet effects can be neglected. The blood flow estimation procedure also involves specification of blood viscosity that might differ from subject to subject. A potential method for circumventing this problem is to estimate blood flow from the time-varying velocity profiles acquired by ultrasound color flow techniques [8]. Thirdly, the angle correction of the velocity measurements will directly influence the slope of the upstroke of the area-flow loop (Fig. 1C), and thereby influence the pulse wave velocity estimate. Fourth, the filtering of the velocity waveforms may affect the slope of the upstroke of the waveform because there is such an abrupt change in velocity at the foot of the waveform. However,

care was taken to avoid ringing effects when designing the filter. Finally, the velocity and diameter data were not recorded simultaneously. However, the ultrasound system used can be modified to record blood velocity and vessel diameters simultaneously. One possibility is to estimate blood velocity and diameter waveforms from the same RF data [4]. Another possibility is to transmit pulses in two different directions, one perpendicular to the vessel to record diameters, and another oblique to the vessel to record velocities [15].

## 5 Conclusion

We derived a new method for estimating pulse wave velocity (area-flow method). To make the area-flow method applicable to non-invasive ultrasound recordings, we also developed a method for estimating arterial blood flow from Doppler velocity measurements. The area-flow method can hence be based solely on ultrasound measurements of arterial diameter and blood velocity. Data from 21 human subjects (age 23–74) and four dogs showed that the area-flow method and a comparison method agreed well on average. When the human subjects were divided into three separate age groups, both methods gave group means that increased with age. As expected, the estimated pulse wave velocity also decreased when the aortic pressure was lowered in two of the dogs. However, on a per-subject basis, discrepancies were observed between the methods, indicating that the methods cannot be used interchangeably. We believe that the major reasons for the discrepancies were: 1) the use of brachial pulse pressure as a substitute for local pulse pressure in the comparison method, 2) inaccurate flow estimates, 3) inaccurate angle corrections of the velocity measurements, and 4) non-simultaneous recordings of velocity and diameter data. However, these problems are related to the measurements used as inputs to the methods and not to the validity of Eqs. 1 and 6 per se.

## 6 Acknowledgments

This study was supported by Program for Medical Technology at the Norwegian University of Science and Technology. We thank Steinar Bjærum for advise regarding the filtering of the velocity waveforms, Gunnar Taraldsen for discussions about the Mann-Whitney test, and Nancy Lea Eik-Nes for revision of the paper.

## References

1. Benthin M, Dahl P, Ruzicka R, Lindstrom K. Calculation of pulse-wave velocity using cross correlation—effects of reflexes in the arterial tree. *Ultrasound Med Biol* 1991;17:461–9.

2. Bland JM, Altman DG. Statistical methods for assessing agreement between two methods of clinical measurement. *Lancet* 1986;1:307-10.
3. Bramwell JC, Hill AV. The velocity of the pulse wave in man. *Proc Roy Soc* 1922; XCIII:298-306.
4. Brands PJ, Hoeks AP, Hofstra L, Reneman RS. A noninvasive method to estimate wall shear rate using ultrasound. *Ultrasound Med Biol* 1995;21:171-85.
5. Brands PJ, Willigers JM, Ledoux LA, Reneman RS, Hoeks AP. A noninvasive method to estimate pulse wave velocity in arteries locally by means of ultrasound. *Ultrasound Med Biol* 1998;24:1325-35.
6. Fung YC. *Biomechanics - Circulation*. New York: Springer-Verlag, 2nd ed., 1997.
7. Hayashi K. Experimental approaches on measuring the mechanical properties and constitutive laws of arterial walls. *J Biomech Eng* 1993;115:481-8.
8. Kasai C, Namekawa K, Koyano A, Omoto R. Real-time two-dimensional blood flow imaging using an autocorrelation technique. *IEEE Trans Sonics Ultrason* 1985;SU-32:458-463.
9. Langewouters GJ, Wesseling KH, Goedhard WJ. The static elastic properties of 45 human thoracic and 20 abdominal aortas in vitro and the parameters of a new model. *J Biomech* 1984;17:425-35.
10. Li JK. Time domain resolution of forward and reflected waves in the aorta. *IEEE Trans Biomed Eng* 1986;33:783-5.
11. Milnor WR. *Hemodynamics*. Baltimore, Maryland, USA: Williams and Wilkins, 2nd ed., 1989.
12. Nichols WW, O'Rourke MF. *McDonald's blood flow in arteries. Theoretical, experimental and clinical principles*. London: Arnold, 4th ed., 1998.
13. Rabben SI, Bjærum S, Sørhus V, Torp H. Ultrasound-based vessel wall tracking: an auto-correlation technique with RF center frequency estimation. *Ultrasound Med Biol* 2000; Submitted.
14. Sindberg Eriksen P, Gennser G, Lindstrom K, Benthin M, Dahl P. Pulse wave recording-development of a method for investigating foetal circulation in utero. *J Med Eng Technol* 1985;9:18-27.
15. Sugawara M. Wave intensity analysis: a new method for the dynamic study of heart-vessel interactions. In: *European Medical and Biological Engineering Conference, 1999, Vienna, Austria*. vol. I, 1999; 24-27.
16. Westerhof N, Sipkema P, van den Bos CG, Elzinga G. Forward and backward waves in the arterial system. *Cardiovasc Res* 1972;6:648-656.

17. Womersley JR. Method for the calculation of velocity, rate of flow and viscous drag in arteries when the pressure gradient is known. *J Physiol* 1955;127:553-63.



# Paper E



# Estimation of the central aortic pressure waveform from diameter and blood velocity measurements in the canine carotid artery

Stein Inge Rabben<sup>1</sup>, Nikos Stergiopoulos<sup>2</sup>, Leif Rune Hellevik<sup>3</sup>,  
Patrick Segers<sup>4</sup>, Otto A. Smiseth<sup>5</sup>, Thor Edvardsen<sup>5</sup>,  
Helge Skulstad<sup>5</sup> and Bjørn Angelsen<sup>1</sup>

<sup>1</sup>Department of Physiology and Biomedical Engineering, NTNU, Trondheim, Norway

<sup>2</sup>Biomedical Engineering Laboratory, EPFL, Lausanne, Switzerland

<sup>3</sup>MTF/Division of Applied Mechanics, NTNU, Trondheim, Norway

<sup>4</sup>Hydraulics Laboratory, IBITECH, University of Gent, Belgium

<sup>5</sup>Institute for Surgical Research, National Hospital, Oslo, Norway

## Abstract

Recently, investigators presented a model study of a novel method for deriving central aortic pressure waveforms from measurements of carotid pressure and flow. The method is based on separating the carotid pressure into its incident and reflected components, shifting these in time according to the propagation time from the central aorta, and adding the shifted incident and reflected waves (lossless transmission line approach). In this study, we evaluate this method on carotid diameter and velocity measurements from four dogs. In the four dogs, the lossless transmission line method did not give reliable reconstructions of the central aortic pressure. To find a possible explanation for the findings, we also evaluated a viscous transmission line model. The viscous transmission line model, which gave better reconstructions, indicated that there was considerable attenuation in the carotid arteries of the four dogs, probably due to the small diameters of the dog carotid arteries (2.0–2.5 mm). However, the viscous losses in humans are lower than in dogs, since human carotid diameters are larger. Therefore, the method should be further tested on human data.

Unpublished

## 1 Introduction

The central aortic pressure determines the systolic load on the left ventricle and influences the coronary perfusion during diastole [15]. Because central aortic pressure waveforms cannot be measured non-invasively, it is common to measure peripheral pulse waveforms and to calibrate these by oscillometrically recorded systolic and diastolic brachial artery pressures.

However, because of wave propagation and reflections, the peripheral pulse waveforms are different from the central aortic pressure waveforms [15]. Investigators have introduced methods to estimate the central aortic pressure waveform from radial pulse waveforms through generalized transfer functions. Generalized transfer functions have been determined from models [9] or from invasive pressure measurements on groups of patients [4, 10]. However, differences between individual and generalized transfer functions may exist, resulting in erroneous prediction of the central aortic pressure.

Stergiopoulos et al. [18] have recently presented a transfer function that permits reconstruction of central aortic pressure waveforms from peripheral pressure and blood velocity measurements. With this method, a determination of central aortic pressure can be done on a per-patient basis, thereby avoiding the use of a generalized transfer function. The vessel between the central aorta and the measurement site is considered as a lossless transmission line (Fig. 1). The central aortic pressure waveform is obtained by separating the measured pressure waveform into incident and reflected components [14, 20], and shifting these in time according to their travel time from and to the central aorta. The method of Stergiopoulos et al. [18] has not yet been validated experimentally, and the aim of the current study was to evaluate this method on measurements from dogs.

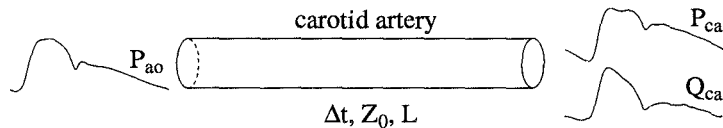


**Figure 1:** The carotid artery is represented as a uniform tube, in which incident and reflected pressure and flow waves propagate.  $P_{ao}$  - the pressure at the carotid inlet.  $P_{ca}$  - the pressure at the measurement site.  $Q_{ca}$  - the flow at the measurement site.  $\Delta t$  - wave propagation time.  $Z_0$  - characteristic impedance.  $L$  - segment length.

The state of the art non-invasive method for measuring peripheral pressure waveforms is applanation tonometry [11, 12]. However, applanation tonometry is sensitive to the hold-down force and the transducer positioning and orientation and applies best to arteries with a bone underneath, such as the radial artery [5]. Pressure is related to cross-sectional area by constitutive laws [6]. If the pressure-area relation is approximately linear in the operating range, pressure can be estimated by calibrating area

measurements. Cross-sectional areas are potentially easier to measure than tonometer pulse waveforms, since diameter recordings can be guided by two-dimensional ultrasound imaging [2, 7, 16].

In four mongrel dogs, we recorded carotid cross-sectional area and blood velocity by ultrasound, and aortic pressure by catheter-tipped micromanometry. To compare with the lossless transmission line approach (LTLM) of Stergiopoulos et al. [18], we also estimated the aortic pressure by calibrating and time-shifting the carotid area measurements (CTSM), and by using a viscous transmission line approach (VTLM) [1, 8, 19].

## 2 Materials and methods

### 2.1 Dog experiments

Four mongrel dogs with body weight  $26 \pm 5$  kg (mean  $\pm$  sd) were given thiopentone (25 mg/kg b.w.) and morphine 100 mg IV, followed by infusion of morphine (50–100 mg/h) IV and pentobarbital 50 mg IV every hour. The animals were artificially ventilated through a cuffed endotracheal tube using room air with 20–50% oxygen. The Norwegian Experimental Animal Board approved the dog experiments that were also performed for other purposes.

#### Pressure recordings

In all dogs, central aortic pressure was measured by a 5F micromanometer-tipped catheter (Model MPC-500, Millar Instruments, Houston, USA) introduced into a femoral artery and positioned in the thoracic aorta near the orifice of the left carotid artery. In addition, in two of the dogs, the left common carotid artery pressure was measured by a 2F micromanometer-tipped catheter (Model SPR-407, Millar Instruments, Houston, USA) introduced in the left external carotid artery. Pressure data were digitized at 200 Hz by an ultrasound scanner and stored for further analysis together with the simultaneously recorded ultrasound data (see below). The pressure transducers were calibrated by use of a mercury manometer prior to each experiment. A fluid filled catheter in central aorta was used for absolute pressure reference. Recordings were first made during stable hemodynamic conditions.

#### Ultrasound recordings

A System FiVe ultrasound scanner (GE Vingmed Ultrasound, Horten, Norway) with a 10 MHz linear array probe was used for recording ultrasound data. The recordings were performed on the left common carotid artery, 3–5 cm proximal to the bifurcation of the internal and external carotid arteries. First we recorded 8–10 cardiac cycles of ultrasound radio frequency (RF) data for extraction of vessel diameter. If necessary,

we steered the RF M-line perpendicular to the artery. After this, we recorded 10–20 cardiac cycles of pulsed wave (PW) Doppler data for the extraction of maximum blood velocities. To obtain maximum velocities, the sample volume of the PW Doppler was made large enough to cover the central portion of the vessel’s cross-section. In all recordings, the steering of the Doppler line was 30 degrees, and the angle correction was 45–60 degrees.

### Blood flow estimation

Blood flow was estimated from the maximum velocities of the PW Doppler spectrums by using an extension of Womersley’s theory of flow in rigid tubes [21]. The estimation method is described in Rabben et al. [17].

### Cross-sectional area estimation

The inner diameter of the vessel was tracked from the RF data according to the method of Rabben et al. [16]. By assuming rotational symmetry around the vessel-axis, the cross-sectional area was estimated from the diameter measurements.

## 2.2 Estimation of aortic pressure by calibrating and time-shifting the carotid area waveforms (CTSM)

The vessel’s cross-sectional area depends on the distending pressure. Various constitutive laws have been suggested to represent the pressure-area relation [6]. Usually, the viscoelasticity of the wall is neglected, and a non-linear constitutive relation is assumed:

$$P = P(A) \tag{1}$$

where  $P$  is the distending pressure, and  $A$  is the cross-sectional area. If the pressure-area relation is approximately linear in the operating range, Eq. 1 can be linearized around a mean pressure by introducing the area compliance ( $C_A = \partial A / \partial P$ ), and the pressure waveform can be estimated simply by calibrating the area waveform. Usually, the mean and diastolic pressures are used for calibration, because the mean pressure drop along large arteries is negligible.

A simple method for estimating the aortic pressure is then to calibrate and time-shift the carotid area waveform. The propagation time  $\Delta t$  from the aorta to the measurement site, was estimated by aligning the upstroke of the calibrated area waveform to the upstroke of the aortic pressure waveform.

### 2.3 Estimation of the aortic pressure by a lossless transmission line model (LTLM)

#### Principle

This method, which is due to Stergiopoulos et al. [18], is based on separating the carotid pressure waveform into its incident (forward) and reflected (backward) components, and then shifting these waveforms in time according to their propagation times from and to the central aorta. The incident waveform is delayed with respect to the central aortic pressure waveform and needs to be shifted backward in time, whereas the reflected waveform runs towards the central aorta and needs to be shifted forward in time.

#### Theory

When we assume no frictional losses, the carotid artery can be represented as a lossless transmission line, and the central aortic pressure can be estimated as:

$$\hat{P}_{ao} = \frac{1 + \Gamma e^{-j2\omega\Delta t}}{(1 + \Gamma) e^{-j\omega\Delta t}} P = P_f e^{j\omega\Delta t} + P_b e^{-j\omega\Delta t} \quad (2)$$

where  $\Gamma = \frac{P_b}{P_f}$  is the reflection coefficient at the measurement site,  $j = \sqrt{-1}$ ,  $\omega$  is the angular frequency,  $\Delta t$  is the wave propagation time from the aorta to the measurement site,  $P$  is the pressure at the measurement site, and subscripts  $f$  and  $b$  denote forward and backward waves, respectively. To obtain the forward and backward waves of Eq. 2, we use the wave-separation technique of Westerhof et al. [20]:

$$P_f = \frac{1}{2} [P + Z_0 Q] \quad , \quad P_b = \frac{1}{2} [P - Z_0 Q] \quad (3)$$

where  $Z_0$  is the characteristic impedance and  $Q$  the flow at the measurement site. The characteristic impedance, which is the relation between unidirectional pressure and flow waves, can be estimated during early systole as  $Z_0 = \frac{\Delta P}{\Delta Q}$  [14], since the early systolic wave is normally free of reflections.

#### Estimation procedure

The carotid pressure is estimated by calibrating the carotid area-distension waveform to mean and diastolic pressures of the aortic pressure waveform. From the carotid pressure and flow waves, the characteristic impedance is estimated during early systole as  $Z_0 = \frac{\Delta P}{\Delta Q}$  (Fig. 2B). The carotid pressure waveform is then separated into its forward and backward waves according to Eqs. 3 (Fig. 2C). Finally, the aortic pressure is reconstructed by using Eq. 2 (Fig. 2D). The propagation time  $\Delta t$  of Eq. 2 is estimated by aligning the upstroke of the carotid pressure waveform to the upstroke of the aortic pressure waveform.

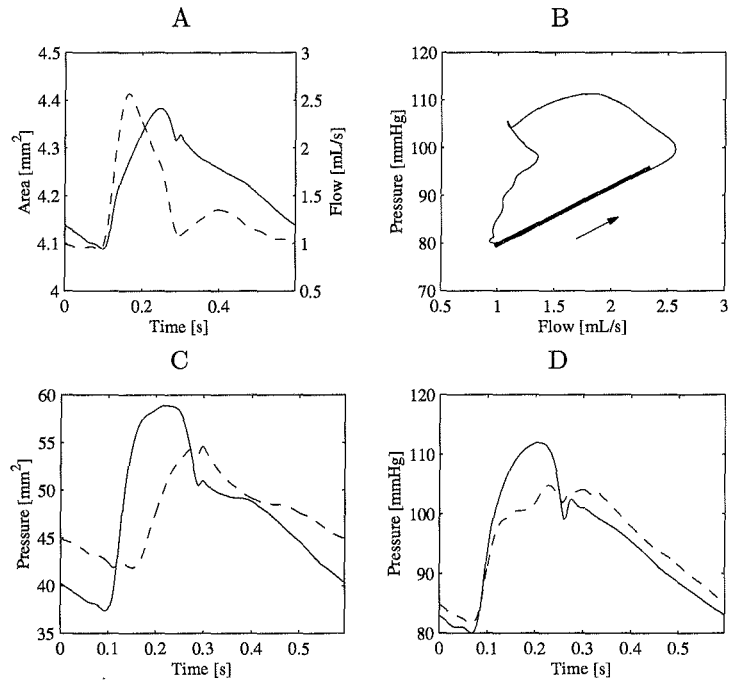


**Figure 2:** Illustration of the lossless transmission line method (LTLM). Panel A: measurements of cross-sectional area (—) and blood flow (---) of the common carotid artery of dog#1. Panel B: carotid pressure versus flow. The slope during early systole is the characteristic impedance,  $Z_0 = \frac{\Delta P}{\Delta Q}$ . Panel C: the incident (—) and reflected (---) carotid pressure. Panel D: the measured (—) and reconstructed (---) aortic pressure.

## 2.4 Estimation of the aortic pressure waveform by a viscous transmission line model (VTLM)

### Principle

The viscous transmission line approach is also based on separating the carotid pressure waveform into its incident and reflected components. However, because of attenuation, the incident and reflected waves cannot simply be time-shifted. Instead, the incident waveform is backward-propagated to the aorta, through time-shifting and increasing the amplitudes of each harmonic according to the propagation coefficient and segment length, whereas the reflected wave is forward-propagated to the aorta, through time-shifting and decreasing the amplitudes of each harmonic according to the propagation coefficient and segment length. The approach used here is analogous to those of Taylor [19], Avolio [1], and Karamanoglu and Feneley [8].

## Theory

To include frictional losses due to viscosity of the blood and viscoelasticity of the vessel wall, the carotid artery must be represented by a transmission line with viscous damping. The central aortic pressure is then estimated as:

$$\hat{P}_{ao} = \frac{1 + \Gamma e^{-2\gamma L}}{(1 + \Gamma) e^{-\gamma L}} P = P_f e^{\gamma L} + P_b e^{-\gamma L} \quad (4)$$

where  $\gamma$  is the propagation coefficient and  $L$  is the length from the aorta to the measurement site. An estimate of the propagation coefficient is given as [22]:

$$\gamma = \frac{j\omega}{c} \frac{1}{\sqrt{1 - F_{10}}} \quad (5)$$

where  $F_{10}$  is the Womersley function, and  $c$  is the wave propagation velocity:

$$c = c_0 e^{j\theta/2} \quad (6)$$

In Eq. 6,  $c_0$  is the inviscid Moens-Korteweg wave propagation velocity, and  $\theta$  represents the phase lead of pressure in relation to wall displacement. Taylor [19] suggested the following expression for the variation of  $\theta$  with frequency:

$$\theta = \theta_0 (1 - e^{-2\omega}) \quad (7)$$

where  $\theta_0$  is the phase angle at high frequencies.

To obtain the forward and backward waves of Eq. 4, we use the same wave-separation technique as for the lossless transmission line (Eq. 3). However, for the viscous transmission line model, a frequency dependent characteristic impedance  $Z_0$  must be used [22]:

$$Z_0 = \frac{\rho c}{A} \frac{1}{\sqrt{1 - F_{10}}} \quad (8)$$

## Estimation procedure

The estimation procedure is illustrated by Fig. 3. Using the viscous transmission line model (Eqs. 4– 8), we iteratively estimate the wave propagation velocity  $c_0$  and the segment length  $L$  by fitting (in a root-mean-square sense) the model output  $\hat{P}_{ao}$  to the measured aortic pressure waveform  $P_{ao}$ . During the estimation, the other parameters of the viscous transmission line model are fixed (Table 1). For the lossless transmission line model, we obtain an estimate of the carotid pressure by calibrating the carotid area-distension waveform to the mean and diastolic pressures of the aortic waveform. However, with the viscous transmission line approach, the mean and diastolic carotid and aortic pressures will be different due to attenuation. Therefore, the calibration of the area-distension waveform is done during the estimation scheme by adjusting the mean ( $\bar{P}_{ca}$ ) and diastolic ( $P_{ca,d}$ ) pressures at each iteration. Fig. 4D shows the final result of the aortic pressure estimation. The incident and reflected pressures at the measurement site (Fig. 4B) and at the carotid inlet (Fig. 4C) are also plotted.

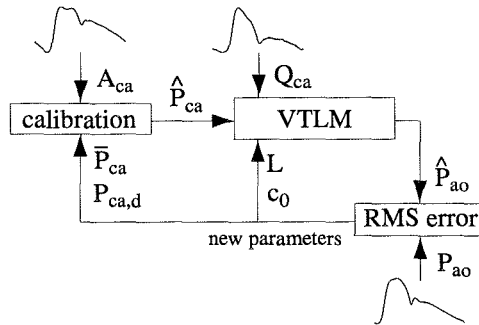


**Figure 3:** Block diagram of the viscous transmission line method (VTLM). The aortic pressure is estimated from carotid pressure ( $\hat{P}_{ca}$ ) and flow ( $Q_{ca}$ ) by use of Eqs. 4– 8. The minimal root-mean-square (RMS) error between estimated ( $\hat{P}_{ao}$ ) and measured ( $P_{ao}$ ) aortic pressure is found iteratively by adjusting the parameters  $L$ ,  $c_0$ ,  $\bar{P}_{ca}$  and  $P_{ca,d}$  according to a non-linear optimization algorithm. The carotid pressure  $\hat{P}_{ca}$  is estimated at each step by calibrating the carotid area-distension waveform ( $A_{ca}$ ).

Parameter	Symbol	Value	Unit
Blood density	$\rho$	1060	kg/m <sup>3</sup>
Blood viscosity	$\mu$	0.0035	Pa s
Viscoelasticity phase angle	$\theta_0$	7.2	deg

**Table 1:** Fixed model parameters for the viscous transmission line approach. The blood viscosity is used for determining the Womersley function  $F_{10}$ , and for estimating flow from maximum velocities. The value of the viscoelasticity phase angle is taken from the work of Bergel [3].

## 2.5 Analysis

The measured and the estimated aortic pressures were compared in terms of systolic and diastolic pressures and in terms of shape. The shape of the waveforms was assessed according to their root-mean-square errors:

$$RMS = \sqrt{\frac{1}{N} \sum (P_{ao} - \hat{P}_{ao})^2} \quad (9)$$

where  $P_{ao}$  and  $\hat{P}_{ao}$  are measured and reconstructed aortic pressures, respectively, and  $N$  is the number of data points.

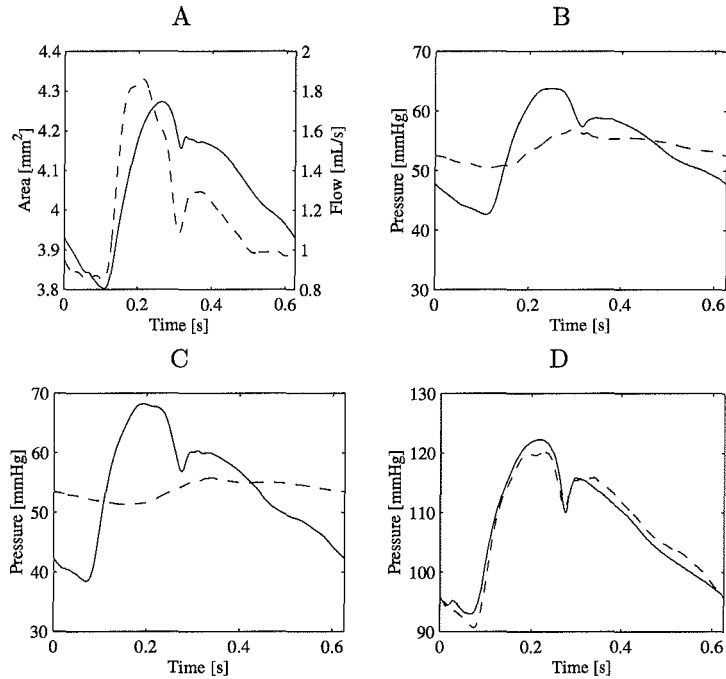


**Figure 4:** Example outputs of the viscous transmission line approach. Panel A: measurements of cross-sectional area (—) and blood flow (---) of the common carotid artery of dog#3. Panel B: the incident (—) and reflected (---) carotid pressure. Panel C: the incident (—) and reflected (---) carotid pressure after backward-propagation (incident wave) and forward-propagation (reflected wave). Panel D: the measured (—) and reconstructed (---) aortic pressure waveforms.

### 3 Results

#### 3.1 Measured versus estimated pressure waveforms

Fig. 5 shows the measured and estimated aortic pressures in the four dogs. For the calibrated and time-shifted carotid area waveform ( $\cdots$ ), the upstroke of the reconstructed pressure is not as steep as the upstroke of the measured pressure. Correspondingly, the reconstructed pressures have a later peak than the measured pressures. The differences between the peak and notch (insicura) pressures are also smaller for the reconstructed than for the measured pressure waveforms. For the lossless transmission line approach (---), there are large discrepancies between the reconstructed and measured aortic pressure. The estimated peak pressures are much lower than the measured peak pressures, and the estimated systolic pressures are too low compared to the estimated

diastolic pressures. For the viscous transmission line approach (- · -), the discrepancies between reconstructed and measured aortic pressure are smaller.

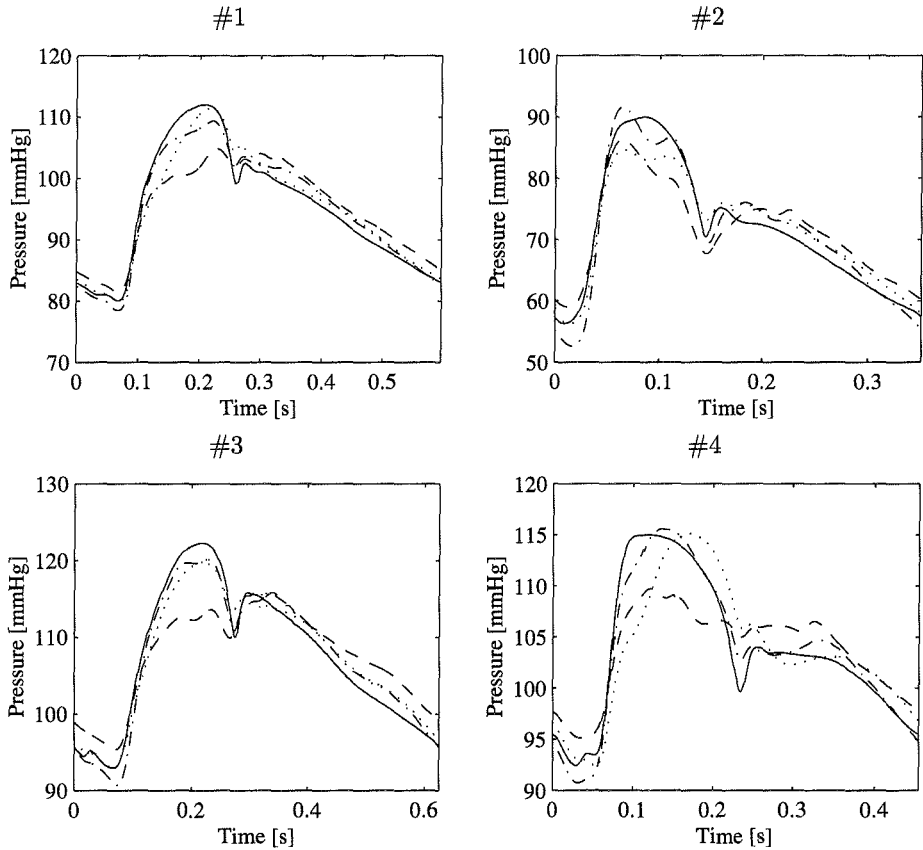


**Figure 5:** Measured (—) and estimated aortic pressures in the four dogs. The aortic pressure was estimated by 1) calibrating and time-shifting the carotid cross-sectional area (···), 2) the lossless transmission line model (- - -), and 3) the viscous transmission line model (- · -).

Table 2 shows diastolic, systolic, and RMS errors between the measured and the estimated pressure waveforms. The lossless transmission line had the largest errors, whereas the viscous transmission line had the smallest errors.

Table 3 lists the estimated parameters of the reconstruction methods. The propagation times  $\Delta t$  estimated by aligning the upstroke of the area-distension waveform to the upstroke of the measured aortic pressure were comparable to the propagation times of the viscous transmission line ( $L/c_0$ ). In the dogs, the distance between the carotid

Method	Error	#1	#2	#3	#4
Calibrated cross-sectional area	RMS	2.3	2.8	1.9	3.5
	$e_{P_s}$	-0.6	-5.4	-2.5	0.1
	$e_{P_d}$	0	0	0	0
Lossless transmission line	RMS	4.4	4.1	4.3	3.6
	$e_{P_s}$	-7.18	-3.7	-6.4	-5.3
	$e_{P_d}$	1.5	2.7	2.4	2.7
Viscous transmission line	RMS	1.8	2.4	1.7	1.4
	$e_{P_s}$	-2.6	1.5	-2.1	0.5
	$e_{P_d}$	-1.6	-3.7	-2.3	-1.7

**Table 2:** Root-mean-square (RMS), systolic ( $e_{P_s}$ ) and diastolic ( $e_{P_d}$ ) errors (in mmHg) between measured and estimated pressure waveforms.

inlet and the measurement site was approximately 20 cm, measured by ruler. Table 3 shows that the viscous transmission line gave comparable estimates of the segment lengths  $L$ .

Parameter		#1	#2	#3	#4	Unit
Propagation time (CTSM/LTLM)	$\Delta t$	30	35	44	38	ms
Characteristic impedance	$Z_0$	12.1	20.1	15.1	8.9	$\frac{\text{mmHg}}{\text{mL/s}}$
Inviscid wave velocity	$c_0$	5.2	6.0	5.8	4.0	m/s
Segment length	$L$	13.6	18.3	20.1	14.6	cm
Propagation time (VTLM)	$L/c_0$	26	30	36	37	ms

**Table 3:** Estimated parameters. The estimated propagation time  $\Delta t$  was used both in CTSM and LTLM. The characteristic impedance  $Z_0$  was estimated by LTLM, whereas the inviscid wave velocity  $c_0$  and the segment length  $L$  were estimated in VTLM. The propagation time of VTLM ( $L/c_0$ ) is listed for comparison with the propagation time  $\Delta t$  used in CTSM and LTLM.

## 4 Discussion

The lossless transmission line approach did not give reliable reconstructions of the central aortic pressure in dogs. A possible reason may be seen in Fig. 4. At the measurement site (Fig. 4B), the ratio between the amplitudes of the reflected and the incident waves is 0.31, whereas at the carotid inlet (Fig. 4C), the ratio between the amplitudes of the reflected and the incident waves is 0.15. Hence, the propagating waves are severely attenuated and the assumption of lossless propagation is probably not valid.

The attenuation of the waves in the canine carotid artery is probably due to the small diameter of the vessel. In the four datasets, the mean diameters were 2.3, 2.2, 2.3, and 2.4 mm. Correspondingly, the Womersley numbers ( $\alpha = R\sqrt{\omega\frac{\rho}{\mu}}$ ), for the first harmonic, were 2.1, 2.5, 2.0, and 2.5. With such low Womersley numbers, the frictional forces are more important than the inertial forces, hence giving significant losses. In the dogs, the distance from the inlet of the carotid artery to the measurement site was 20–23 cm. Together with small vessel diameters, this gives significant attenuation. Stergiopoulos et al. [18] noted that the lossless transmission line approach will not work properly on measurements from arteries with small diameters. Our study is an experimental confirmation of this.

To test the hypothesis that the reflected wave is severely attenuated, we modified the lossless transmission line approach by only time-shifting and calibrating the incident wave, thus effectively neglecting the reflected component. The results are shown in Fig. 6. This simple modification gave good results, with RMS errors in the same range as for the viscous transmission line. In humans, however, the carotid diameter is 6–7 mm. Consequently, the frictional losses will be smaller than in the canine carotid artery, and the reflected waves will be less attenuated when arriving at the central aorta. Hence, the method of calibrating and time-shifting the forward wave will probably not work in humans.

In this study, we have calibrated the carotid area-distension waveforms to obtain estimates of carotid pressure waveforms. The underlying assumption is that the vessel's cross-sectional area is linearly dependent on the distending pressure. Various studies have shown that this is not the case [6, 13]. One might claim that our procedure for estimating the carotid pressure waveform is part of the reason for the poor performance of the lossless transmission line. Therefore, in two of the dogs (# 3 and #4), we measured carotid pressure and diameter simultaneously (Fig 7). In both cases, the pressure-diameter relations were practically linear, which indicates that the calibration procedure is applicable.

The viscous transmission line method gave good reconstructions of the central aortic pressure waveforms, but the current method cannot be used non-invasively. The estimated aortic pressure is determined by an iteration scheme in which the measured aortic pressure waveform is needed. However, the viscous transmission line approach illustrates the effect of attenuation in the canine carotid arteries, and gives a possible explanation for the poor performance of the lossless transmission line approach.

It must also be noted that the estimation of characteristic impedance  $Z_0$  affects the reconstruction of the aortic pressure. In this study, the characteristic impedance was estimated as the slope of the ratio between pressure and flow during the early rise in systole. Potential problems with the flow estimation technique were briefly addressed in Rabben et al. [17]. Inaccurate estimation of flow affects the estimation of characteristic impedance, and thereby the reconstruction. However, Stergiopoulos et al. [18] have shown that a very accurate determination of characteristic impedance is not essential for the reconstruction of aortic pressure.

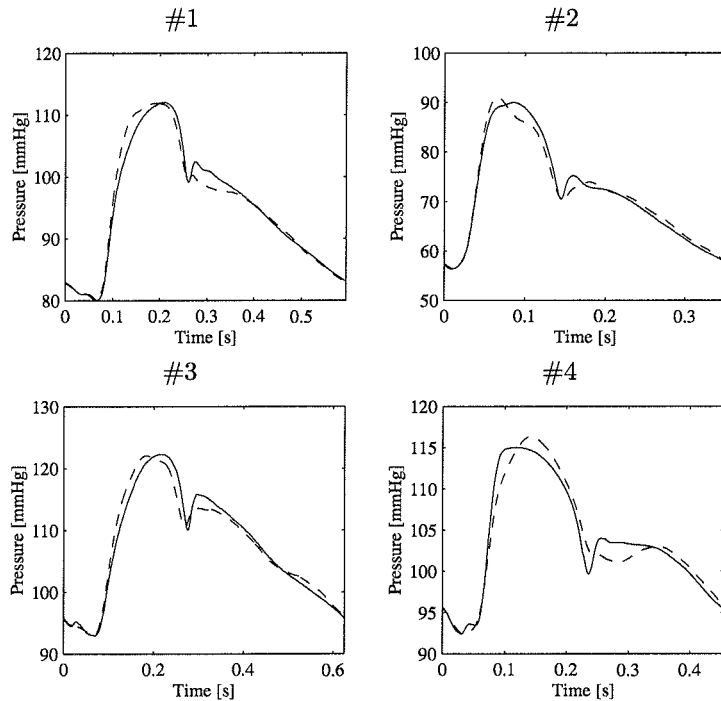


**Figure 6:** Measured and estimated aortic pressures in the four dogs. (—) measured aortic pressure. (- - -) aortic pressure estimated time-shifting and calibrating the forward wave of the lossless transmission line approach.

**In conclusion,** the lossless transmission line method did not reliably reconstruct the canine aortic pressure waveform, the probable explanation being that the small vessel diameter causes considerable attenuation. In humans, however, the viscous losses are lower than in dogs, due to larger human carotid diameters. Therefore, the method should be further tested on human data.

## 5 Acknowledgments

This study was supported by the Program for Medical Technology at the Norwegian University of Science and Technology. We thank Nancy Lea Eik-Nes for revision of the paper.

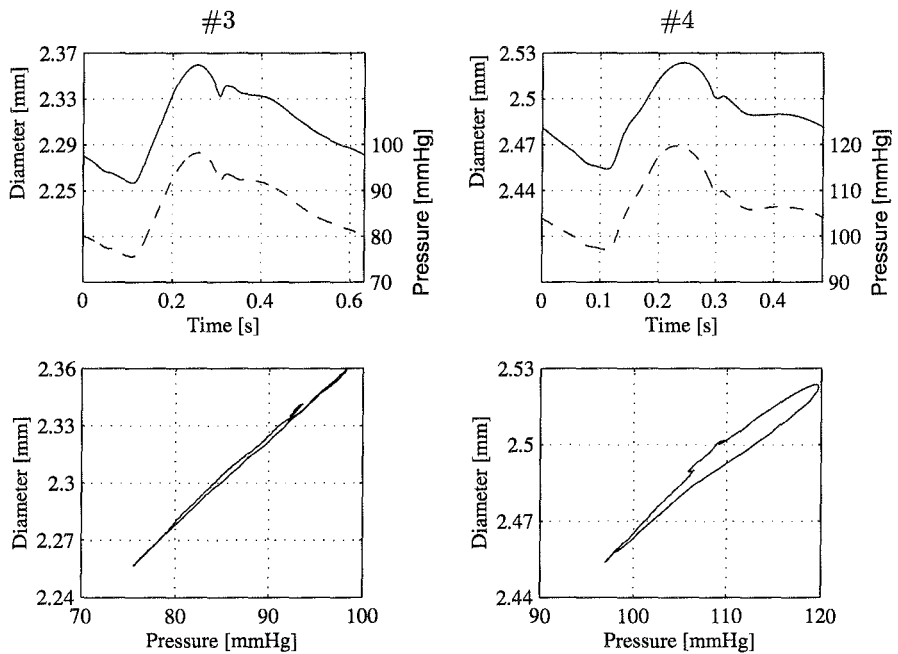


**Figure 7:** Left common carotid diameter (—) and blood pressure (---) in dog #3 and #4. In the lower panels, diameter has been plotted against pressure. In dog #4, the diameter-pressure plot shows viscoelastic effects (hysteresis).

## References

1. Avolio AP. Multi-branched model of the human arterial system. *Med Biol Eng Comput* 1980;18:709–18.
2. Benthin M, Dahl P, Ruzicka R, Lindstrom K. Calculation of pulse-wave velocity using cross correlation—effects of reflexes in the arterial tree. *Ultrasound Med Biol* 1991;17:461–9.
3. Bergel DH. The dynamic elastic properties of the arterial wall. *J Physiol* 1961; 156:458–469.
4. Chen CH, Nevo E, Fetis B, Pak PH, Yin FCP, Maughan WL, Kass DA. Estimation of central aortic pressure waveform by mathematical transformation of radial tonometry pressure. Validation of generalized transfer function. *Circulation* 1997; 95:1827–36.
5. Drzewiecki GM, Melbin J, Noordergraaf A. Arterial tonometry: review and analysis. *J Biomech* 1983;16:141–52.

6. Hayashi K. Experimental approaches on measuring the mechanical properties and constitutive laws of arterial walls. *J Biomech Eng* 1993;115:481–8.
7. Hoeks AP, Brands PJ, Smeets FA, Reneman RS. Assessment of the distensibility of superficial arteries. *Ultrasound Med Biol* 1990;16:121–8.
8. Karamanoglu M, Feneley MP. Derivation of the ascending aortic-carotid pressure transfer function with an arterial model. *Am J Physiol* 1996;271:H2399–404.
9. Karamanoglu M, Gallagher DE, Avolio AP, O'Rourke MF. Pressure wave propagation in a multibranched model of the human upper limb. *Am J Physiol* 1995;269:H1363–9.
10. Karamanoglu M, O'Rourke MF, Avolio AP, Kelly RP. An analysis of the relationship between central aortic and peripheral upper limb pressure waves in man. *Eur Heart J* 1993;14:160–7.
11. Kelly RP, Hayward C, Ganis J, Daley J, Avolio AP, O'Rourke M. Noninvasive registration of the arterial pressure pulse waveform using high-fidelity applanation tonometry. *J Vasc Med Biol* 1989;1:142–9.
12. Kemmotsu O, Ueda M, Otsuka H, Yamamura T, Winter DC, Eckerle JS. Arterial tonometry for noninvasive, continuous blood pressure monitoring during anesthesia. *Anesthesiology* 1991;75:333–40.
13. Langewouters GJ, Wesseling KH, Goedhard WJ. The static elastic properties of 45 human thoracic and 20 abdominal aortas in vitro and the parameters of a new model. *J Biomech* 1984;17:425–35.
14. Li JK. Time domain resolution of forward and reflected waves in the aorta. *IEEE Trans Biomed Eng* 1986;33:783–5.
15. O'Rourke MF, Kelly RP, Avolio AP. *The arterial pulse*. Philadelphia: Lea & Febiger, 1992.
16. Rabben SI, Bjærum S, Sørhus V, Torp H. Ultrasound-based vessel wall tracking: an auto-correlation technique with RF center frequency estimation. *Ultrasound Med Biol* 2000; Submitted.
17. Rabben SI, Stergiopoulos N, Hellevik LR, Smiseth O, Slørdahl S, Urheim S, Angelsen B. An ultrasound-based method for determining pulse wave velocity in the carotid artery 2000; Unpublished work.
18. Stergiopoulos N, Westerhof B, Westerhof N. Physical basis of pressure transfer from periphery to aorta: a model-based study. *Am J Physiol* 1998;274(4 Pt 2):H1386–92.
19. Taylor MG. The input impedance of an assembly of randomly branching elastic tubes. *Biophys J* 1966;6:29–51.

20. Westerhof N, Sipkema P, van den Bos CG, Elzinga G. Forward and backward waves in the arterial system. *Cardiovasc Res* 1972;6:648-656.
21. Womersley JR. Method for the calculation of velocity, rate of flow and viscous drag in arteries when the pressure gradient is known. *J Physiol* 1955;127:553-63.
22. Womersley JR. An elastic tube theory of pulse transmission and oscillatory flow in mammalian arteries. Tech. Rep. WADC TR 56-614, Wright Air Development Center. Aeronautical Research Laboratory, 1957.